DISSERTATION | DOCTORAL THESIS

Titel | Title

Development of magnon-based offset-free magnetic field sensors

verfasst von | submitted by

Ing. Markus Gattringer BSc MSc

angestrebter akademischer Grad | in partial fulfilment of the requirements for the degree of

Doktor der Naturwissenschaften (Dr.rer.nat.)

Wien | Vienna, 2024

Studienkennzahl lt. Studienblatt | Degree programme code as it appears on the student record sheet:	UA 796 605 411
Dissertationsgebiet lt. Studienblatt | Field of study as it appears on the student record sheet:	Physik
Betreut von | Supervisor:	Univ.-Prof. Dipl.-Ing. Dr.techn. Dieter Süss Privatdoz.

Storm'd at with shot and shell,
While horse and hero fell,
They that had fought so well
Came thro' the jaws of Death,
Back from the mouth of Hell,
All that was left of them,
Left of six hundred.

Abstract

The abilitiy to rapidly, accurately, and remotely determine vital information has become one of the cornerstones of progress in engineering. Sensors that can detect and measure magnetic fields — magnetometers — play a large part in applications to determine mechanical parameters (*i. e.* position or motion) and support the storage and processing of digital data.

There exist a range of different methods to measure magnetic fields, with the two most common ones in engineering applications being based on the Hall-effect and the magnetoresistive effect. One of the biggest challenges is the development of an offset-free magnetometer that provides zero signal at zero field, regardless of the manufacturing accuracy. There exist techniques to minimize this offset but for magnetoresistive magnetometers considerable offset remains.

A method to measure magnetic fields that has only been examined superficially in the past, especially regarding the ability to nullify the offset, is measurement based on spin waves — magnons. The behavior of those magnons is sensitive to any external magnetic field. The amplitude of the wave is used as its indicative quantity; the employed detection method then relies on spin pumping and the inverse spin-Hall effect to generate a voltage signal.

Using spin pumping means that the detection does not rely on an electric current afflicting the necessary multilayer heterostructure, therefore avoiding Joule heating and increasing the lifetime of the device. The downside is decreased sensitivity. Spin pumping has hitherto never been employed in a practical design.

To employ spin pumping in a micromagnetic setup, a computation model had to be developed. This was published in a peer-reviewed journal and integrated in the used micromagnetic solver suite. The model solves the spin drift-diffusion equation, complete with coupling terms, in both directions, to the magnetization dynamics.

A design based on a standing spin-wave was examined numerically. The results have also been published in a peer-reviewed journal. It is indeed free from offset, within the limits of micromagnetic simulations.

As the manufacturing requirements for this design are rather high, and the resulting sensitivity is very low, owing to the limited amplitude possible for a spin wave, a second design has also been examined numerically. This relies on ferromagnetic resonance, *i. e.* a magnon without momentum. This design remedies, at least to some extend, the major shortcoming of the first.

It can be assessed that a design based on magnetic precession and/or spin pumping can not compete with Hall-effect devices, both regarding sensitivity and offset. However, compared to magnetoresistive devices, the obtained results, especially for the second design, look promising. Future work, *i. e.* fabrication of a prototype and testing, is necessary to obtain real-world data.

Zusammenfassung

Die Fähigkeit wichtige Informationen rasch, genau und aus der Ferne festzustellen ist ein Grundstein des Fortschrittes in der Technik geworden. Sensoren die Magnetfelder detektieren und messen können — Magnetometer — spielen eine wichtige Rolle in Anwendungen in denen mechanische Parameter (*i. e.* Position oder Bewegung) ermittelt werden und unterstützen die Speicherung und Verarbeitung digitaler Daten.

Es existieren verschiedene Methoden Magnetfelder zu messen, als weitestverbreitete in technischen Anwendungen basierend auf dem Hall-Effekt und dem magnetoresistiven Effekt. Eine der größten Herausforderungen ist die Entwicklung eines Offset-freien Magnetometers welches in Abwesenheit eines Feldes kein Signal ausgibt, ohne Einfluss der Fertigungsgenauigkeit. Es existieren Techniken um diesen Offset zu minimieren, aber für magnetoresistive Magnetometer verbleibt eine beträchtliche Abweichung.

Eine Methode Magnetfelder zu messen die in der Vergangenheit nur oberflächlich behandelt wurde, vor allem in Hinsicht der Möglichkeit den Offset auszulöschen, ist Messung auf der Basis von Spin-Wellen — Magnonen. Das Verhalten dieser Magnonen ist empfindlich auf externe Felder. Die Amplitude der Welle dient als Indikator; die verwendete Detektionsmethode basiert auf spin pumping und dem inversen Spin-Hall-Effekt um ein Spannungssignal zu erzeugen.

Die Verwendung von spin pumping bedeutet dass die Detektion nicht auf einem elektrischen Strom durch die Materialschichten basiert und damit Aufheizung verhindert wird; dies erhöht auch die Lebensdauer der Struktur. Der Nachteil ist aber verminderte Empfindlichkeit. Spin pumping wurde bis jetzt in keinem praktikablen Entwurf verwendet.

Um spin pumping in einem mikromagnetischen Umfeld behandeln zu können, wurde ein Rechenmodel erstellt. Dieses wurde auch in einem Fachmagazin veröffentlicht und in der verwendeten mikromagnetischen Plattform integriert. Das Modell löst die Spin-Drift-Diffusionsgleichung komplett mit den Kopplungstermen, in beiden Richtungen, zur Magnetisierungsdynamik.

Ein Entwurf basierend auf einer stehenden Spin-Welle wurde numerisch untersucht. Die Ergebnisse wurden auch in einem Fachmagazin veröffentlicht. Es ist in der Tat frei von Offset, innerhalb der Grenzen mikromagnetischer Simulationen.

Die Anforderungen an den Fertigungsprozess dieses Entwurfes sind recht hoch, und die Empfindlichkeit, resultierend aus der begrenzten Amplitude einer Spin-Welle, recht niedrig. Ein zweiter Entwurf wurde deshalb ebenfalls numerisch untersucht. Dieser basiert auf ferromagnetischer Resonanz, *i. e.* ein Magnon ohne Impuls. Dieser Entwurf behebt im Wesentlichen die Beschränkungen des Ersten.

Es kann festgestellt werden dass ein Entwurf basierend auf magnetischer Präzession und/oder spin pumping nicht gegen Hall-Effekt-Magnetometer bestehen kann, sowohl hinsichtlich Empfindlichkeit als auch Offset. Verglichen mit magnetoresistiven Magnetometern sind die erzielten Ergebnisse, vor allem des zweiten Entwurfes, jedoch vielversprechend. Zukünftige Bearbeitung, *i. e.* Herstellung eines Prototypen und dessen Test, ist notwendig um reelle Aussagen treffen zu können.

Contents

Chapter 1: Introduction

Star Trek, the TV show created by Gene Roddenberry in 1966, proved to have a cultural — lasting — impact much larger than anything from that period. Aside from any memes about frequent deaths of crew members with a uniform of a certain color, much of the technology depicted would motivate future physicists and engineers to create it. Be it superluminal travel [1, 2], matter teleportation [3, 4] (at least on quantum scale) or personal communicators (the nowadays ubiquitous cell phones), the fiction has become reality. But aside from technologies that exist only in theory or laboratories, or cell phones that had a questionable impact on society, it was one technology of *Star Trek* that would become the cornerstone of progress.

Figure 1.1: A *Mk VII Tricorder* from *Star Trek — Voyager*. Via `https://www.ex-astris-scientia.org`.

The ability to rapidly, accurately, and remotely determine vital information. **Sensors**. The *tricorder*, a handbag-, later fist-sized device that can detect basically anything (figure 1.1). Shipboard sensors that can detect the presence of a Klingon battle cruiser half a lightyear away. Or sensors that can measure the radiation flux in the matter/anti-matter reaction assembly.

And while some of the capabilities have not been recreated in the real world, modern solid state manufacturing has made it possible to indeed create sensing devices with stunning capabilities. Devices that enabled the advances in solid state manufacturing in the first place.

Also devices that enabled the current information age, in that they support the storage and processing of information [5]. Even sensing devices that in the past relied on mechanical concepts, simply because they determine mechanical parameters (*i. e.* position or motion), have been replaced with solid-state devices for reasons of price, accuracy and reliability [6, chps. 5 & 7]. Sensors that can **detect and measure magnetic fields** — **magnetometers** — play a large part in both applications. This is hardly a surprise: magnetic fields, be it in the form of *Oersted fields* (subsection 2.2.2) or *itinerant magnetism* (subsection 2.2.3 and 2.2.5), are the only easily modifiable interaction in physics and can be tailored to sensing needs.

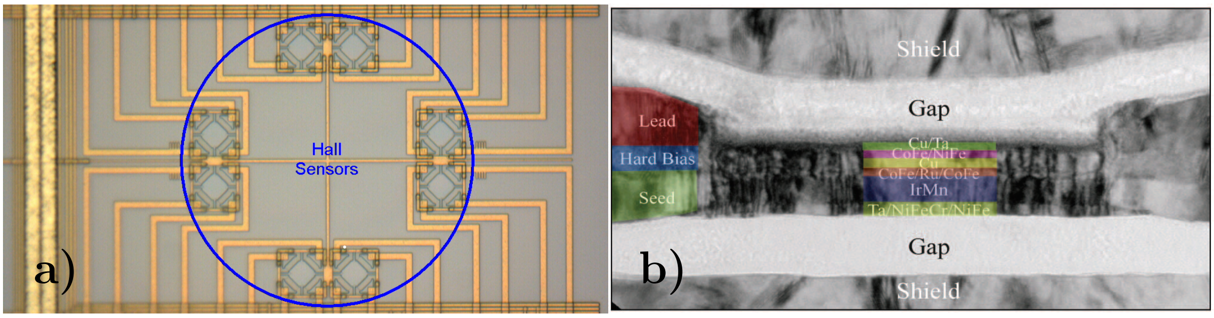

Figure 1.2: a): An AK8975 Hall-effect magnetometer as used in some iPhone generations. Via *MEMS Journal*. **b)**: TEM image of a GMR read head. The purple, yellow, and orange layers constitute the actual GMR structure. Reprinted from McFadyen *et al.* [8].

1.1 Magnetometers

A list of different types of magnetometers can be found in [7]. They all have in common that a **signal** S, commonly a **voltage** U, is produced as a **function of a measured magnetic flux density** $\vec{B}$, where the vector nature of that field generally introduces direction-dependency to the device.

Induction and fluxgate magnetometers are based on *Faraday's law* [9, pp. 208–211]. They offer very high sensitivity and are used both for scientific and commercial applications, but are of macroscopic size.

SQUIDs (superconducting quantum-interference devices) [10], based on the *Josephson effect* (after B. D. Josephson [11]), offer superior sensitivity, but are limited to laboratory use.

Magneto-optical magnetometers are heavily employed in physics, including magnonics, but have little application outside. Their strength lies in their scanning ability as they are based on the *Faraday effect* (after M. Faraday [12]) or *Kerr effect* (after J. Kerr [13]).

Hall-effect magnetometers [14], based on the *Hall effect* [15], are the most widely used magnetometers, if just because the overwhelming majority of them is used to determine mechanical parameters. They are heavily used in automation, automotive and aviation. Their large production numbers and overall high production value means that they have been brought almost to perfection, regarding manufacturing and signal processing. The Hall-effect magnetometer array employed in some iPhones is shown in figure 1.2 **a)**.

Magnetoresistive magnetometers are based on magnetoresistive effects. These are either *anisotropic magnetoresistance* (**AMR**) [16, 17], *giant magnetoresistance* (**GMR**) [18, 19], or *tunnel-magnetoresistance* (**TMR**) [20, 21]. Such devices are of sub-nanometer size and have high sensitivity. Originally employed in read heads of hard disks, they have also successful forayed into the domains dominated by Hall-effect magnetometers [22]. A transmission electron microscope (TEM) image of such a read head is shown in figure 1.2 **b)**.

Resonance magnetometers are specialized setups. They are best known from medical applications — nuclear magnetic resonance is, after all, nothing else then a magnetometer with powerful signal processing. Nanoscale resonance-type magnetometers have been proposed before [23], but they still employ GMR to generate a signal. There is no large scale application of this type.

Other types of magnetometers include nitrogen vacancy (NV) detectors [24] and magnetometers that are based on magnons [25, 26]. Also, magnetic force microscopy (MFM) [27] can be counted into that class.

Just by their sheer production volume, Hall-effect and magnetoresistive magnetometers are the benchmark regarding parameters and properties.

1.2 Basic properties of magnetometers

Finding a physical interaction that can be used as a gauge for a quantity is one thing. Engineering this interaction into a device that can indeed gauge this quantity, reliably and reproducible, is a completely different matter. Sensors in general have characteristic properties that define how the their signal behaves during actual operations. This is also true for magnetometers. What follows is a non-exhaustive list of such properties [28].

Linear range defines the range of the measured quantity that produces a signal that is approximately a linear function of the quantity, *i. e.* $U = \widehat{a}\,\vec{B}$. Complex physical interactions tend to not be linear, and hence this behavior is only achievable for small measured values around a working point. A quantifier for the linearity of magnetometers has been introduced [29]. Ideally, this value would be as high as possible.

Hysteresis and perming describe the change of magnetometer parameters due to high fields. *Magnetic hysteresis* [30, pp. 26–28] is the irreversible behavior of magnetic systems due to nonlinear effects. If the fields that the magnetometer is exerted to are outside its linear range, its response can change. Degaussing or reperming mechanisms are necessary to combat this.

Sensitivity gives the slope of the signal. Since any magnetometer has to be powered, here also the consumed power has to be considered. This is commonly given as $\left(\mathrm{d}U/\mathrm{d}B_1 = a_{11}\right)/I$ in $\mathrm{V}/(\mathrm{T\,A})$, where I is the current supplied to the device. B_1 is the vector component of $\vec{B}$ that the magnetometer is supposed to measure; most magnetometers are 1-dimensional sensors. It is obvious that a high value is desired.

Transversal sensitivity is the slope of the signal, $\left(\mathrm{d}U/\mathrm{d}B_2 = a_{12}\right)/I$ or $\left(\mathrm{d}U/\mathrm{B}_3 = a_{13}\right)/I$. Now the vector components are those that the magnetometer is not supposed to measure. This should be zero.

Offset and Offset drift describe the affine deviation from the linear behavior. Instead the signal is given by $U = \widehat{a}\,\vec{B} + O\left[t, T, \vec{B}\right]$, where a non-zero offset O produces a signal even when no measured quantity exists. Offset drift is the deviation of the offset from — constant — nominal behavior; the offset can be dependent on magnetometer age (so basically t), temperature T and even measured field itself.

Noise describes all kinds of noise in the system, be it directly from the physical principles, temperature effects, or signal processing [31]. It is generally quantified utilizing the *Fourier time spectral density* $\bar{S}[f]$ [32, Spectral Power Density] of the signal.

Detectivity is the ratio noise to sensitivity [33],

$$D[f] = \frac{\bar{S}[f]}{a_{11}}. \tag{1.1}$$

As such it provides a figure-of-merit for the signal-to-noise-ratio.

One of the biggest challenges is the **development of an offset-free** magnetometer that provides zero signal at zero field, regardless of the manufacturing accuracy. For a magnetoresistive magnetometer, the resistance is measured, which is of course non-zero. For Hall-effect magnetometers, the generated Hall voltage is in principle free from offset, but fabrication errors and material defects introduce a measured output voltage.

To eliminate the offset, different methods are employed. For magnetoresistive magnetometers, an array of four detectors is connected in a *Wheatstone-bridge setup* to nullify the measured resistance in field-less case [34, 35]. For Hall-effect magnetometers, a *spinning-current* setup is used, whereby different contacts of the Hall cross have voltage applied to them successively; the offset can then be nullified by comparing the different resulting signals [36]. In both cases, offset elimination results from comparison of different signals. The elimination can therefore only be complete if all those subsignals behave perfectly identical. In practice, a finite **offset remains**, due to fluctuating material parameters, fabrication errors, and temperature fluctuations (thus making the offset temperature dependent [37]). Contemporary TMR magnetometers exhibit offsets of several mT even after the nullification setup [38, 39].

N. b. that additional corrective measures have to be employed for the ever present magnetic field of the earth. These are outside of the scope of these considerations.

1.3 Introduction to magnonics

From a naive micromagnetical standpoint, the existence of **micromagnetic waves** (to contrast them with electromagnetic waves) does not seem to be very exciting. Introduction of an oscillating outside stimulus (*i. e.* some external field) should create some propagating oscillating deviation in magnetization, as is the case for every aether. F. Bloch was able to show in 1930 [40] that harmonic micromagnetic waves are **eigenstates** of the ferromagnetic system, which provides justification for their importance. Since the ferromagnetic system relies on the exchange interaction between spins, this gives rise to the term **spin wave**. T. Holstein and H. Primakoff [41] introduced a quantized, bosonic formulation for those spin waves in 1940 (chapter 8). This makes it possible to treat spin waves as quasi-particles, and hence the term **magnon** was coined (though it was not possible to determine who introduced it; the earliest useage found was by C. Kittel in 1958 [42]).

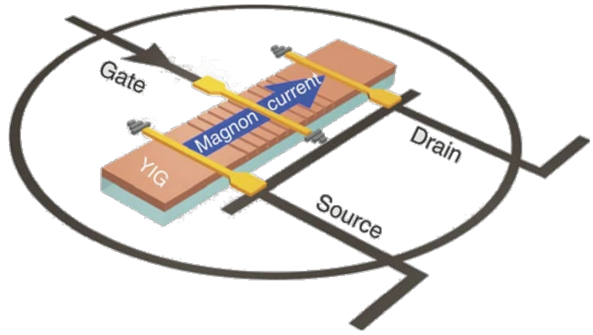

Figure 1.3: Schematic of a proposed magnon transistor. Reprinted from C h u m a k *et al.* [43].

Such spin waves possess properties that make them interesting as means for signal processing and computing [44, 45] (see also figure 1.3). Not only do they follow a **dispersion relation** (chapter 7), when the dipolar interaction between spins (subsection 2.2.5) enters the picture, qualitatively different dispersion relations are resulting for large wavelengths, with one of them exhibiting surface waves with very high group velocity (subsection 7.3.2) and another one exhibiting negative group velocity (subsection 7.3.1). The shape of the dispersion relation line generally is that of a Lorentz distribution, with the line width determined by the Gilbert damping of the material. The same damping value also determines the lifetime of the spin wave. The mean free path is on the order of several micrometers.

The dispersion relations are also influenced by any external field. Thus, it comes as no surprise that spin waves can principally act as **magnetometers**. Such concepts have been evaluated [26], but the general method used is by employing **magnonic crystals**: magnons, like phonons, do not posses a band gap. By engineering one into the system, magnetometers with very high sensitivity can be constructed [25, 46, 47].

One advantage of a magnetometer based on spin waves is that the wave's behavior is dependent on shape, material, material orientation, wave direction, and magnetization direction. This provides a lot of flexibility on how to engineer a suitable magnetometer.

1.4 About this work

Employing the flexibility to engineer a magnetometer on the basis of spin waves, the aim is to **design and evaluate a variant that provides offset-free behavior**, ideally from a single device.

In research, spin waves are usually detected by employing magneto-optical methods like the magneto-optical Kerr effect, or Brillouin-scattering methods. Such methods are not useful for applications. The alternative method investigated herein, is **spin-pumping** (part II) coupled with the **inverse spin-Hall effect** (section 3.4). Spin pumping has never been proposed as part of a magnetometer, although it is commonly used as a detection method in experimental magnonics [48, 49, 50].

The **first** examined design (part IV) is based on a **standing spin-wave**. Compared to a propagating wave, this offers some advantages, like more precise excitation and lower impact of the Gilbert damping parameter. The dispersion relation of the spin-wave is shifted by the field to be measured, yielding slightly different excitation efficiencies and, in turn, different wave amplitudes. Spin pumping and the inverse spin-Hall effect translate this into field-dependent voltages. By exploiting the shape anisotropy of the waveguide, the two possible longitudinal magnetization configurations provide two signals, enabling for comparative measurements, eliminating the offset. Conceptually, this follows the idea of the spinning current, using successive comparative measurements. The different measurements here always employ the very same parts of the system, and not different current paths and leads as for the spinning current, thereby eliminating possible sources of offset.

This is intended to be a qualitative study. As such, the parameters listed in section 1.2 are not computed, with the exception of the offset, for which a detailed analysis is provided.

The **second** examined design (part V) is based on **ferromagnetic resonance** in a nanoellipse. This is not strictly a magnon-based magnetometer, although even with a wave vector of zero it is still an eigenvector in the magnonic sense. This approach is based on the same shift of the dispersion relation by the field to be measured. Again, spin pumping and the inverse spin-Hall effect translate this into field-dependent voltages, as these concepts have been shown to hold promise. The shape anisotropy of the ellipse is used to eliminate the offset. The reasons for the move to a resonance-based magnetometer are the following: Firstly, fabrication is simplified. And secondly, the yielded voltage is much higher.

For this design, sensitivity and linear range are explicitly computed. An analysis of the offset is provided.

The examination is done purely on a numerical basis, based on **micromagnetics** and the **spin drift-diffusion** model. The functionality of the magnetometers is proven, and concepts for practical implementation are presented. This also means that offset drift, noise and detectivity are not accessible, as temperature has a large effect.

The computations are performed using the finite element-based micromagnetics solver suite MAGNUM.PI, which is an evolution of the earlier MAGNUM.FE [51]. It is based on the FIREDRAKE [52] finite-element framework. FIREDRAKE uses the PETSc [53] library and corresponding Python bindings [54]. Equation solvers are provided by the CVODE part of the SUNDIALS package [55]. Meshes of the geometry have been created with SALOME (`https://www.salome-platform.org/`), while refinement/manipulation/conversion was done with GMSH [56].

Part I provides the micromagnetic foundations: classic micromagnetics in chapter 2, spintronic extension in chapter 3, and the finite-element treatment in chapter 4. To facilitate spin-pumping computations, a **numerical solver mechanism** had to be developed. This is detailed in part II. Part III provides the analytical magnonic froundations: ferromagnetic resonance in chapter 6, classical dispersion relations in chapter 7, the quantized treatment in chapter 8, and the origins on non-linear behavior in micromagnetic simulations in chapter 9. The magnetometer design based on a standing spin wave is presented in part IV. Part V describes the design based on ferromagnetic resonance.

This research was carried out as part of the Austrian Science Fund (FWF) I 4917-N “Non-reciprocal 3D architectures for magnonic functionalities” project [57]. For this purpose, the author was employed by the University of Vienna. The computational results presented have been partly achieved using the Vienna Scientific Cluster (VSC).

1.5 Conventions in this work

The following conventions will be adhered to in this work:

- Vectors in running text, captions and figures will always be denoted by a right arrow over the variable, *i. e.* $\vec{x}$.
- Matrices in running text, caption and figures will always be denoted by a wide hat over the variable, *i. e.* $\widehat{A}$.
- Vectors and matrices in equations will always be represented in index notation, *i. e.* x_p or A_{pq}. A specific component is addressed when the index is a number.
- Sets of multiple, or all, components of the same vector, such as in the argument of a function, are denoted with curly brackets, *i. e.* $\{x_w\}$.
- Indices are always set in *italics*, whereas super- and subscripts are always set upright.
- Indices as subscripts are vector components, whereas indices as superscripts are for enumeration.
- *Einstein's summation convention* [58] will be followed, *i. e.* summation over all subscript indices appearing twice in a product is implicit. Should any subscript indices appear more than two times, summation starts at the right side of the product.
- ε_{pqr} in equations denotes the *Levi-Civita pseudotensor* [32, Permutation Symbol].
- Functional arguments are enclosed in square brackets to avoid ambiguity with multiplication.
- For quantum-mechanical treatments, the *bra-ket* formalism by P. A. M. Dirac [59] is employed.

Part I

Basics of micromagnetics and spintronics

This part is a modified and extended version of the one found in the author's Master's thesis [60].

The general concept of the micromagnetic model is to resolve the magnetic material at the mesoscale level, *i. e.* still above the atomic (and therefore quantum) level, but fine enough to resolve all magnetic structures that can form, *e.g.* domain walls. The general methods are compiled by W. F. Brown, jr. [61].

At the foundation, the atomic (or even electronic) magnetic moments need to be averaged over a suitable chunk of space. Hence, it is possible to define the **magnetization** $\overrightarrow{M}$,

$$M_p^{\Omega_\mathrm{m}} = \frac{1}{V_{\Omega_\mathrm{m}}} \sum_{i \in \Omega_\mathrm{m}} \mu_p^i, \tag{1.2}$$

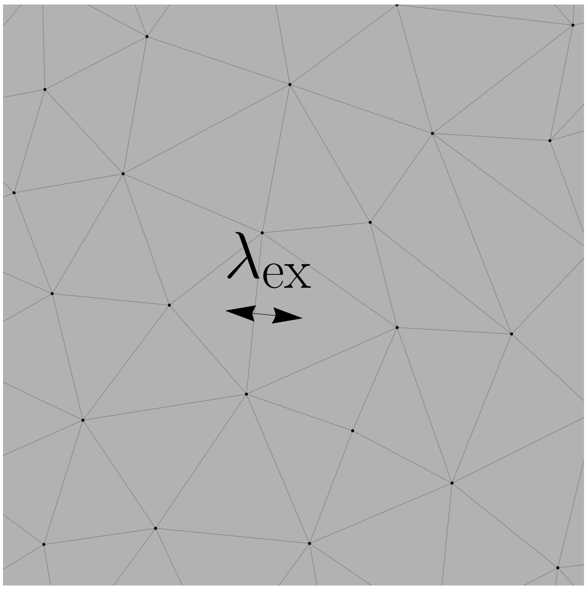

Figure 1.4: 2D tessellation of a magnetic material, showing the individual chunks. The distance between the centerpoints of the neighboring triangles should be below λ_ex for the micromagnetic assumption to be valid.

where the $\overrightarrow{\mu^i}$ are the individual magnetic moments that are summed up over the corresponding volume V_{Ω_m} and normalized.

Under the micromagnetic assumption that the magnetization can only vary at a length scale

$$\lambda_\mathrm{ex} = \sqrt{\frac{A_\mathrm{ex}}{K_\mathrm{eff}}}, \tag{1.3}$$

which is called **exchange length** (figure 1.4), the other variables will be explained in subsection 2.2.3, 2.2.4 and 2.2.5 where the ratio behind this term becomes clear), the magnetic moments in equation (1.2) can, in principle, be replaced by a field $\overrightarrow{M}[\vec{x}]$, and the summation by integration, such that

$$M_p^{\Omega_\mathrm{m}} = \frac{1}{V_{\Omega_\mathrm{m}}} \int_{\Omega_\mathrm{m}} M_p\left[\{x_w\}\right]\, \mathrm{d}V_{\Omega_\mathrm{m}}, \tag{1.4}$$

where $V_{\Omega_\mathrm{m}} < \lambda_\mathrm{ex}^3$. If the material is homogeneous at the scale of λ_ex, the magnetization can change its direction, but its magnitude remains a constant. This is generally true only for crystalline substances, however; for amorphous magnetic substances without a lattice, the norm does change in space. Hence, the **saturation magnetization** M_S, measured in A/m, can be factored out, and the magnetic moment defined as

$$\mu_p\left[\{x_w\}\right] = M_\mathrm{S}\, V_{\Omega_\mathrm{m}}\, m_p\left[\{x_w\}\right]. \tag{1.5}$$

Calculations can then be performed with this **normalized magnetization** $\vec{m}[\vec{x}]$. The term magnetization will usually be used instead of normalized magnetization in this work; but as always, *context is king*!

The micromagnetic model then also allows the normalized magnetization to be exchanged for an individual atomic magnetic moment in further treatments; whereas the individual moment occupied a volume on the order of a^3 (with a being the lattice constant), the magnetization now occupies a volume V_{Ω_m}.

As physics is based upon the definition of energies, an energy measure has to be introduced. The potential **energy of magnetization** in a magnetic field $\vec{H}\,[\vec{x}]$ can be rewritten from the classical relation (see, *e. g.*, J. D. Jackson [9, pp. 188–191]) to

$$\mathcal{E}_\mathrm{pot} = -\mu_0\, M_\mathrm{S} \int_{\Omega_\mathrm{m}} m_p\,[\{x_w\}]\ H_p\,[\{x_w\}]\ \mathrm{d}V_{\Omega_\mathrm{m}}, \tag{1.6}$$

where μ_0 is the magnetic constant. Therefore, it follows that the effective field corresponding to an energy term is

$$H_p^\mathrm{eff}\,[\{x_w\}] = -\frac{1}{\mu_0\, M_\mathrm{S}\, V_{\Omega_\mathrm{m}}} \frac{\delta \mathcal{E}_\mathrm{pot}}{\delta m_p\,[\{x_w\}]}, \tag{1.7}$$

where the differentiation is performed as a functional derivative (for rules on how to perform such operations, see, *e. g.*, N. Goldenfeld [62, pp. 156–157]). Since the magnetization is now defined as a field, the potential energy has to be an integral anyway, making this possible. *N. b.* that the functional derivative generally introduces a boundary term that is required to be equal to zero, therefore enforcing a boundary condition onto the system. These conditions are known as **Brown's conditions**.

Here, it is assumed that the magnetic volume does not depend on the magnetization, *i. e.*, magnetostrictive effects are ignored. For a short description of these effects, see, *e. g.*, K. M. Krishnan [30, pp. 217–226].

Chapter 2: Magnetization dynamics

2.1 General motion of magnetization

2.1.1 Free motion

Since the magnetization can be exchanged for a magnetic moment, the relation from classical electrodynamics ([9, pp. 188–191]) for the precession in a magnetic field can be rewritten into

$$\frac{\partial m_p\left[\{x_w\}, t\right]}{\partial t} = -\mu_0\ \gamma_\mathrm{e}\ \varepsilon_{pqr}\ m_q\left[\{x_w\}, t\right]\ H_r\left[\{x_w\}, t\right], \tag{2.1}$$

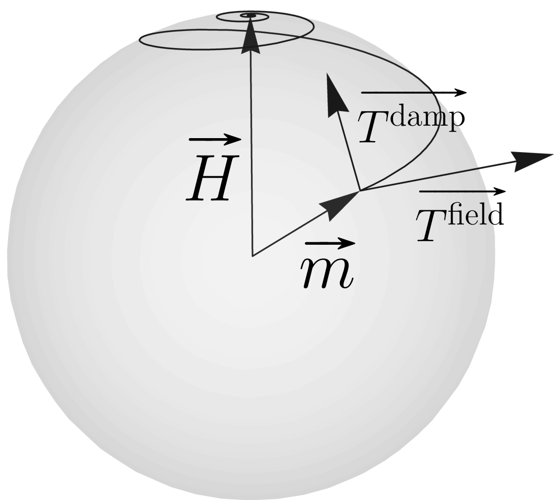

Figure 2.1: Motion of normalized magnetization vector on the surface of the unit sphere, as described by equation (2.5). The torques $\overrightarrow{T}^{\mathrm{field}}$ and $\overrightarrow{T}^{\mathrm{damp}}$ correspond to the two cross product terms in the LLG.

where the magnetic moment was replaced by the normalized magnetization. To transform the torque (equal to the change of the angular momentum), normally found on the left side, into the change of the magnetization, use was made of the fact that the angular momentum and magnetic moment are aligned co-linearly, with the relation provided by the electron gyromagnetic factor,

$$\gamma_\mathrm{e} = \frac{g_\mathrm{e}\ e}{2\ m_\mathrm{e}} = \frac{g_e\ \mu_\mathrm{B}}{\hbar}. \tag{2.2}$$

Here, e is the elementary charge, m_e is the electron mass, μ_B is Bohr's magneton, $\hbar$ is the reduced Planck's constant, and $g_\mathrm{e} \approx 2.002\ldots$ is the g-factor of an electron. This is of course not completely true, since γ for magnetic materials also includes orbital effects, and hence in principle g needs to be the Landé factor ([63, 64]) of the atom. This discrepancy is resolved by absorbing the difference into the definition (from an experimental stand point) of the saturation magnetization. g_e is then fixed at 2 to simplify the constant.

Equation (2.1) then describes the precessional motion of the magnetization under the effect of a magnetic field $\overrightarrow{H}\left[\overrightarrow{x}, t\right]$. Therefore, all interactions in the system need to be formulated as effective fields (section 2.2).

2.1.2 Phenomenological damping

It is evident in nature that the precessional movement described in subsection 2.1.1 is not maintained in perpetuity. Eventually, the magnetization aligns with the fields (or rather the effective field, being a sum of all acting fields) that are acting upon it. Such damping effects generally originate from spin-orbit coupling [65] (*Rashba-Edelstein effect* [66] or *Dresselhaus effect* [67]). As those are difficult to describe, the damping is treated phenomenologically. A first model was introduced by L. Landau and E. Lifshits [68], and added a damping term to equation (2.1), leading to

$$\begin{aligned}\frac{1}{\mu_0}\frac{\partial M_p\left[\{x_w\},t\right]}{\partial t} &= \varepsilon_{pqr}\ H_q\left[\{x_w\},t\right]\ M_r\left[\{x_w\},t\right] \\ &\quad + \alpha\left(H_p\left[\{x_w\},t\right] - \frac{M_p\left[\{x_w\},t\right]\ H_q\left[\{x_w\},t\right]\ M_q\left[\{x_w\},t\right]}{M_r\left[\{x_w\},t\right]\ M_r\left[\{x_w\},t\right]}\right).\end{aligned} \tag{2.3}$$

This is known as the Landau-Lifshits equation. α plays the role of a phenomenological damping constant. In such a form, however, infinite damping would lead to divergence instead of no motion at all. This was rectified by T. L. Gilbert [69], introducing

$$\frac{\partial m_p\left[\{x_w\},t\right]}{\partial t} = -\mu_0\ \gamma_\mathrm{e}\ \varepsilon_{pqr}\ m_q\left[\{x_w\},t\right]\ H_r\left[\{x_w\},t\right] + \alpha\ \varepsilon_{pqr}\ m_q\left[\{x_w\},t\right]\ \frac{\partial m_r\left[\{x_w\},t\right]}{\partial t}. \tag{2.4}$$

This simple form, known as **Landau-Lifshits-Gilbert equation (LLG)**, follows the standard form of damping (as proportional to the rate of change) and avoids the *caveats* of the earlier form. It is an implicit differential equation. It can be transformed by inserting it into its right side and calculating the products, to yield

$$\begin{aligned}\frac{\partial m_p\left[\{x_w\},t\right]}{\partial t} = &-\frac{\mu_0\ \gamma_\mathrm{e}}{1+\alpha^2}\left(\varepsilon_{pqr}\ m_q\left[\{x_w\},t\right]\ H_r\left[\{x_w\},t\right]\right. \\ &\left. + \alpha\ \varepsilon_{pqr}\ \varepsilon_{rln}\ m_q\left[\{x_w\},t\right]\ m_l\left[\{x_w\},t\right]\ H_n\left[\{x_w\},t\right]\right),\end{aligned} \tag{2.5}$$

the explicit form of the LLG. This is now similar in form to equation (2.3), if the cross products are replaced by dot products, but with different constants. The dimensionless **Gilbert damping constant** α then describes the damping behavior of the system. Part II will introduce an additional damping mechanism that is not covered by α.

By inserting the acting fields into the LLG, the dynamics of the system can be completely described. Figure 2.1 shows this schematically.

2.2 Effective fields

2.2.1 Zeeman field

In generalization of the quantum-mechanical *Zeeman effect* [70], a **Zeeman field** $\overrightarrow{H_\mathrm{Zee}}$ is any field that is enforced upon the system from outside and as such acts upon it, but is not affected by it. These are often position- and time-independent, but not necessarily.

2.2.2 Oersted field

Referring to H. C. Ørsted's discovery [71], an **Oersted field** $\overrightarrow{H_{\mathrm{Oe}}}$ is the magnetic field generated by a charge current. It is generally position- and time-dependent. It is described by *Ampere's law* [9, pp. 2–5],

$$\varepsilon_{pqr} \frac{\partial H_r^{\mathrm{Oe}}\left[\{x_w\}, t\right]}{\partial x_q} = \mu_0 \; j_p \left[\{x_w\}, t\right], \tag{2.6}$$

where $\overrightarrow{j}$ is the charge current density. An analytical solution is *Biot-Savart's law* [9, pp. 175–178], but for numerical computations, equation (2.6) is solved directly.

2.2.3 Exchange field

The concept of an exchange interaction was introduced by W. Heisenberg [72] to explain the origin of the molecular field introduced by P. Weiss [73]. It describes the origin of ferromagnetism. The quantum-mechanical interaction via electric fields and the *Pauli principle* [74] results in an exchange integral, giving rise to an **exchange energy** $\mathcal{E}_{\mathrm{ex}}$. This concept was brought by J. H. Van Vleck [75] into the familiar form,

$$\mathcal{E}_{\mathrm{ex}}^{ij} = -2 \; J^{ij} \; S_p^i \; S_p^j, \tag{2.7}$$

where $\overrightarrow{S^k}$ is the total angular momentum vector of the atom at lattice point k and $\widehat{J}$ is the matrix of the exchange integrals. Due to the sign, a positive value of J^{ij} prefers a parallel alignment of momentum (leading to **ferromagnetism**), while a negative value prefers an anti-parallel one (leading to **anti-ferromagnetism**). Ferromagnetism is the "natural" state for metals, while anti-ferromagnetism is very rare.

To turn this quantized exchange into a continuous field, some mathematical treatment is necessary.

To begin, assuming that $\overrightarrow{S^i} \cdot \overrightarrow{S^i} = \overrightarrow{S^j} \cdot \overrightarrow{S^j} = \hbar^2 \; s^2$ (which is clearly true for any pure metals, but as the continuous form is an average *per se* this approach is always valid), the magnitude is factored out, leading to

$$\mathcal{E}_{\mathrm{ex}}^{ij} = -2 \; \hbar^2 \; J^{ij} \; s_p^i \; s_p^j. \tag{2.8}$$

$\overrightarrow{s^k}$ is then the normalized angular momentum. These position dependent spins are replaced by a field $\overrightarrow{s}\left[\overrightarrow{x^k}, t\right]$ and yield

$$\mathcal{E}_{\mathrm{ex}}^{ij}\left[\left\{x_w^i\right\}, \left\{x_w^j\right\}, t\right] = -2 \; \hbar^2 \; J^{ij} \; s_p\left[\left\{x_w^i\right\}, t\right] \; s_p\left[\left\{x_w^j\right\}, t\right]. \tag{2.9}$$

Since a continuous field is required (and the inter-atomic distances $\overrightarrow{d^{ij}}$ are small in relation to the exchange length (equation (1.3)), it is possible to expand $\overrightarrow{s}\left[\overrightarrow{x^j}, t\right] \to \overrightarrow{s}\left[\overrightarrow{x^i} + \overrightarrow{d^{ij}}, t\right]$

to second order. Performing the expansion and calculating the product, the first order terms drop out, resulting in

$$\mathcal{E}_{\text{ex}}^{ij}\left[\left\{x_w^i\right\},t\right] = \hbar^2\ J^{ij}\left(-2+\frac{\partial s_p\left[\left\{x_w^i\right\},t\right]}{\partial x_q}d_q^{ij}\frac{\partial s_p\left[\left\{x_w^i\right\},t\right]}{\partial x_r}d_r^{ij}\right). \tag{2.10}$$

The exchange integrals $\widehat{J}$ were calculated by J. C. Slater [76]. They are

$$J^{ij} = \int_V \Psi_a^*\left[r^i\right]\ \Psi_b^*\left[r^j\right]\left(\frac{1}{r^{ab}}-\frac{1}{r^{aj}}-\frac{1}{r^{bi}}-\frac{1}{r^{ij}}\right)\Psi_a\left[r^i\right]\ \Psi_b\left[r^j\right]\ \mathrm{d}V. \tag{2.11}$$

They are based on wave functions $\Psi\left[r\right]$ of d-orbitals, where the sub-/superscripts a and b denote the two nuclei connected by the orbitals. As such, their value is nearly zero almost everywhere except for very small distances r. Hence, the calculation can be limited to nearest neighbors and the coordination number z introduced, to get

$$\mathcal{E}_{\text{ex}}^{i}\left[\left\{x_w^i\right\},t\right] = \hbar^2\sum_j^z J^{ij}\left(-2+\frac{\partial s_p\left[\left\{x_w^i\right\},t\right]}{\partial x_q}d_q^{ij}\frac{\partial s_p\left[\left\{x_w^i\right\},t\right]}{\partial x_r}d_r^{ij}\right). \tag{2.12}$$

To find the total exchange energy of a system, equation (2.12) needs to be integrated over the whole magnetic volume Ω_{m}:

$$\mathcal{E}_{\text{ex}}^{\text{tot}}\left[t\right] = ¢ + \int_{\Omega_{\text{m}}} A_{qr}\left[\left\{x_w\right\}\right]\frac{\partial m_p\left[\left\{x_w\right\},t\right]}{\partial x_q}\ \frac{\partial m_p\left[\left\{x_w\right\},t\right]}{\partial x_r}\ \mathrm{d}\Omega_{\text{m}}. \tag{2.13}$$

Here all constants were absorbed into a leading constant ¢ or the exchange matrix

$$A_{qr}\left[\left\{x_w\right\}\right] = \frac{1}{4}\ \frac{M_{\text{S}}}{\mu_{\text{B}}}\hbar^2\sum_j^z J^j\left[\left\{x_w\right\}\right]\ d_q^j\left[\left\{x_w\right\}\right]\ d_r^j\left[\left\{x_w\right\}\right], \tag{2.14}$$

which is assumed to be a material constant, *i. e.* it is no longer dependent on the index i. This is true, since on a crystal unit-cell level — for a perfect, infinite crystal — the exchange integrals and inter-atomic distances are constant. However, the exchange matrix is still inside of the integral, as the system may very well consist of multiple different materials. Additionally, the spin representation was replaced by the magnetization representation (introducing the normalization factor of 1/4) and the interaction integrals changed into a volume density; the additional factor to the sum is exactly the volume occupied by a spin. As that matrix is clearly symmetric and real (by virtue of the crystalline lattice), it can be diagonalized such that

$$\mathcal{E}_{\text{ex}}^{\text{tot}}\left[t\right] = \int_{\Omega_{\text{m}}} A_{qq}\left[\left\{x_w\right\}\right]\frac{\partial m_p\left[\left\{x_w\right\},t\right]}{\partial x_q}\frac{\partial m_p\left[\left\{x_w\right\},t\right]}{\partial x_q}\mathrm{d}\Omega_{\text{m}}, \tag{2.15}$$

which is the general form of the exchange energy; the constant, and therefore magnetization-independent, term was dropped. The eigenvalues of the exchange matrix are generally not degenerate, but since the discretization is done on the length scale of λ_{ex}, the small differences average out, and a single value remains. This is then the **exchange constant** A_{ex}, measured in J/m.

Applying equation (1.7), this energy can be transformed into a corresponding field, yielding

$$H_p^{\mathrm{ex}}\left[\{x_w\},t\right] = \frac{2}{\mu_0\, M_{\mathrm{S}}}\frac{\partial}{\partial x_q}\left(A_{\mathrm{ex}}\left[\{x_w\}\right]\frac{\partial m_p\left[\{x_w\},t\right]}{\partial x_q}\right). \tag{2.16}$$

This is then the **exchange field** $\overrightarrow{H_{\mathrm{ex}}}\left[\vec{x},t\right]$. Performing the functional derivative introduces the boundary condition

$$n_q\left[\{x_w\}\right]\frac{\partial m_p\left[\{x_w\},t\right]}{\partial x_q} = 0, \tag{2.17}$$

where $\vec{n}$ is the boundary normal. This states that the projection of the spatial change of the magnetization onto the boundary normal has to be zero, *i. e.*. it is not allowed to change along the normal.

2.2.4 Crystalline anisotropy

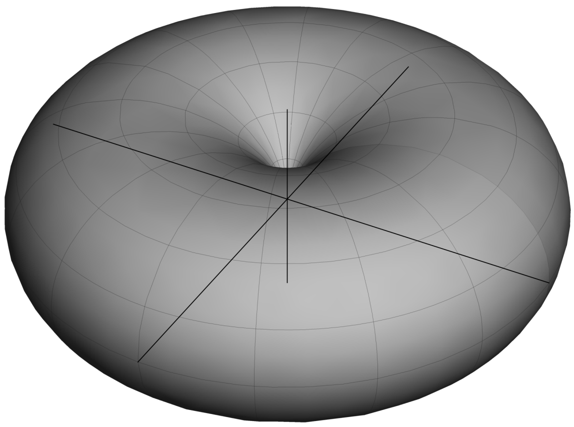

Figure 2.2: Energy surface for uniaxial anisotropy ($K^1 > 0$, $K^2 = 0$), showing the crystallographic *c*-axis as easy axis.

The Heisenberg form in subsection 2.2.3 is not limited to atom/atom interaction, but also extends to atom/electron interactions. As such it couples the (s and p-)electron's total moment with the atom's total moment, forming the total magnetic moment. This is known as spin-orbit coupling and will be elaborated in section 3.4.

On a practical scale, this means, that whenever the magnetization of a material changes its direction, the electronic orbitals, constituting the current loop responsible for the electronic moment, do so too. As those orbitals provide bonding in the material, and are therefore arranged in a lowest-energy configuration, any deviations from it result in a restoring force.

In the case of materials where the directions corresponding to the lowest-energy configuration are uniaxial (hexagonal close-packed or face-centered cubic), the **uniaxial anisotropy energy** $\mathcal{E}_{\mathrm{uni}}$ to model the restoring force can be expressed as an even power series of sines (see, *e. g.*, K. M. Krishnan [30, pp. 197–199]),

$$\frac{\mathcal{E}_{\mathrm{uni}}}{V_{\Omega_{\mathrm{m}}}} = \sum_{i=0}^{\infty} K^i\ \sin^{2i}\left[\theta\right], \tag{2.18}$$

where θ denotes the angle between the magnetization vector and the direction of lowest energy, the so called **easy axis**. The K^i are the **anisotropy constants**. For computation applications, the series is limited to $i = 2$; as K^0 is independent of the state, K^1 and K^2 are then the only relevant components. It is measured in $\mathrm{J/m^3}$. The energy surface resulting from equation (2.18) for positive K^1 is shown in figure 2.2.

For numerical applications, and also generally in magnonics, the anisotropy energy is alternatively formulated as [77, pp. 18–19]

$$\frac{\mathcal{E}_{\text{uni}}}{V_{\Omega_{\text{m}}}} = -\sum_{i=0}^{\infty} K^i \ \cos^{2i}[\theta] \,. \tag{2.19}$$

These anisotropy constants are not equal to the ones of the first formulation. Applying equation (1.7), equation (2.19) can be transformed into a corresponding, albeit fictitious, field, yielding

$$H_p^{\text{uni}}[\{x_w\}, t] = \frac{2}{\mu_0 \ M_{\text{S}}} e_q \ m_q[\{x_w\}, t] \ e_p \left(K^1 + 2 \ K^2 \left(e_q \ m_q[\{x_w\}, t]\right)^2\right). \tag{2.20}$$

This is then the **uniaxial anisotropy field** $\overrightarrow{H_{\text{uni}}}[\vec{x}, t]$. $\vec{e}$ is the easy axis, with the field's strength being modulated (up to being completely reversed), depending upon the orientation of the magnetization.

For materials where the directions corresponding to the lowest-energy configuration are orthogonal (cubic, tetragonal or orthorhombic), the **cubic anisotropy energy** $\mathcal{E}_{\text{cub}}$ to model the restoring force can be expressed as an even power series of cosines (see, *e. g.*, K. M. Krishnan [30, pp. 195–197]),

$$\frac{\mathcal{E}_{\text{cub}}}{V_{\Omega_{\text{m}}}} = \sum_{i=1}^{2} K^i \sum_{j=1}^{5-2i} \prod_{\substack{k=1,2,3\\ k\neq j i^2}} \cos^2\left[\alpha^k\right]. \tag{2.21}$$

where α^k denotes the angle between the magnetization vector and the kth **easy axis**. (The actual term is much simpler than the formula suggests, though not as compact.) The energy surface for positive K^1 is shown in figure 2.3. Again, applying equation (1.7), this can be transformed into a corresponding, albeit fictitious, field, yielding

$$\begin{aligned} H_p^{\text{cub}}[\{x_w\}, t] = \\ -\frac{2}{\mu_0 \ M_{\text{S}}} \Biggl(K^1 \Biggl(\sum_{i=1}^{3} \Biggl(\sum_{\substack{j=1\\ j\neq i}}^{3} m_r[\{x_w\}, t] \ R_{rq} \ \mathbf{e}_q^j \ m_r[\{x_w\}, t] \ R_{rq} \ \mathbf{e}_q^j \Biggr) m_r[\{x_w\}, t] \ R_{rq} \ \mathbf{e}_q^i \ R_{pq} \ \mathbf{e}_q^i \Biggr) \\ + K^2 \left(\prod_{i=1}^{3} m_r[\{x_w\}, t] \ R_{rq} \ \mathbf{e}_q^i \right) \Biggl(\sum_{i=1}^{3} \Biggl(\prod_{\substack{j=1\\ j\neq i}}^{3} m_r[\{x_w\}, t] \ R_{rq} \ \mathbf{e}_q^j \Biggr) R_{pq} \ \mathbf{e}_q^i \Biggr)\Biggr)\Biggr). \end{aligned} \tag{2.22}$$

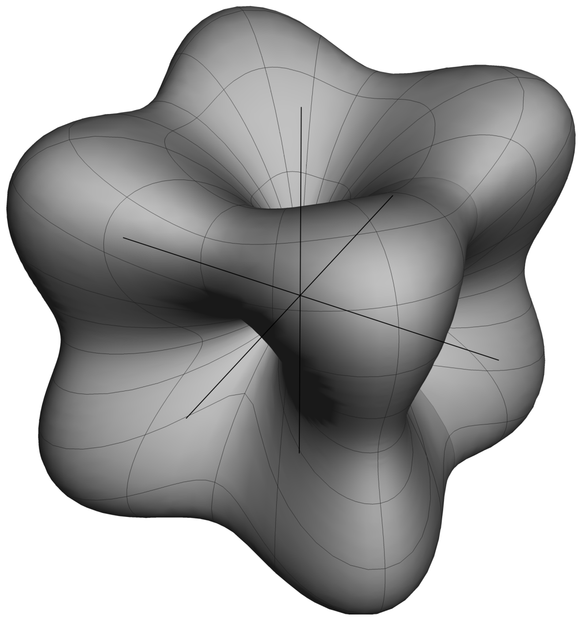

Figure 2.3: Energy surface for cubic anisotropy ($K^1 > 0$, $K^2 = 0$), showing the coordinate axes as easy axes.

This is then the **cubic anisotropy field** $\overrightarrow{H_{\text{cub}}}[\vec{x}, t]$. The $\vec{\mathbf{e}}^i$ are the three coordinate axes. This rather complicated form is the general form including a rotation matrix $\widehat{R}$. Both in experiments and in numerical simulations, the cubic structure does not necessarily align with the laboratory frame, necessitating this generalization.

Due to the way that the crystalline structure is distorted at phase boundaries, or surfaces in general, spin-orbit coupling can also create strong anisotropy effects close to boundaries. If the phase is sufficiently small, this **surface anisotropy** effects the whole of it. It is in general modelled as an uniaxial anisotropy, although that is only a sensible approximation for small ratios of system volume and affected surface.

2.2.5 Demagnetization field

Weiss introduced the notion of the molecular field because the fundamental magnetic interaction is not able to provide for ferromagnetism. The magnetic field of a dipole $\vec{\mu}$ [9, pp. 184–188],

$$H_p\left[\{x_w\}\right] = \frac{1}{4\,\pi}\,\frac{1}{(x_q\,x_q)^{3/2}}\left(3\,x_p\frac{x_q\,\mu_q}{x_r\,x_r} - \mu_p\right), \tag{2.23}$$

quite on the contrary, encourages other dipoles to assume an anti-parallel alignment (unless they are arranged in a special fashion). Therefore the effect of the exchange interaction is reduced (hence the term *demagnetization*).

As per *Maxwell's equations*,

$$\frac{\partial B_p\left[\{x_w\}, t\right]}{\partial x_p} = 0, \tag{2.24}$$

and, in absence of polarization and currents,

$$\varepsilon_{pqr}\,\frac{\partial H_r\left[\{x_w\}, t\right]}{\partial x_q} = 0, \tag{2.25}$$

the divergence of the magnetic field, which itself is the gradient of a potential $U[\vec{x}, t]$, has to vanish. But since in materials, there is

$$B_p\left[\{x_w\},t\right]=\mu_0\left(H_p\left[\{x_w\},t\right]+M_p\left[\{x_w\},t\right]\right), \tag{2.26}$$

equation (2.24) gets amended to

$$\frac{\partial}{\partial x_p}\left(M_p\left[\{x_w\},t\right]-\frac{\partial U\left[\{x_w\},t\right]}{\partial x_p}\right)=0. \tag{2.27}$$

Therefore, now a divergence of the magnetic field, contrary to vacuum, actually exists as long as a divergence of the magnetization exists.

Equation (2.27) is therefore a variant of *Poisson's equation* with the boundary condition at infinity and can be formally solved by using the method of *Green's functions* ([9, pp. 194–198]) to yield

$$\begin{aligned}U\left[\{x_w\},t\right]=\frac{1}{4\,\pi}\Bigg(&\int_{\partial\Omega_\mathrm{m}}\frac{n_p\left[\{y_w\}\right]\;M_p\left[\{y_w\},t\right]}{\sqrt{(x_q-y_q)(x_q-y_q)}}\mathrm{d}\partial\Omega_\mathrm{m}\left[\{y_w\}\right]\\&-\int_{\Omega_\mathrm{m}}\frac{\partial M_p\left[\{y_w\},t\right]}{\partial y_p}\,\frac{1}{\sqrt{(x_q-y_q)(x_q-y_q)}}\mathrm{d}\Omega_\mathrm{m}\left[\{y_w\}\right]\Bigg).\end{aligned} \tag{2.28}$$

The volume term results from *Green's function* for *Laplace's equation* for the magnetic potential and incorporates the natural (open) boundary condition, as $\overrightarrow{U}\left[\overrightarrow{x},t\right]$ exists everywhere, whereas the boundary term incorporates vanishing magnetization at the materials borders. Applying *Green's theorem* ([9, pp. 35–37]), this can be transformed into

$$U\left[\{x_w\},t\right]=\frac{1}{4\,\pi}\int_{\Omega_\mathrm{m}}M_p\left[\{y_w\},t\right]\frac{\partial}{\partial y_p}\,\frac{1}{\sqrt{(x_q-y_q)(x_q-y_q)}}\mathrm{d}\Omega_\mathrm{m}\left[\{y_w\}\right]. \tag{2.29}$$

This yields a **demagnetization field** $\overrightarrow{H_\mathrm{demag}}\left[\overrightarrow{x},t\right]$,

$$H_p^\mathrm{demag}\left[\{x_w\},t\right]=\int_{\Omega_\mathrm{m}}N\left[\{x_w\},\{y_w\}\right]\;M_p\left[\{y_w\},t\right]\;\mathrm{d}\Omega_\mathrm{m}\left[\{y_w\}\right], \tag{2.30}$$

where the **demagnetization tensor** field,

$$N\left[\{x_w\},\{y_w\}\right]=-\frac{1}{4\,\pi}\,\frac{\partial^2}{\partial x_p\,\partial y_p}\,\frac{1}{\sqrt{(x_q-y_q)(x_q-y_q)}}, \tag{2.31}$$

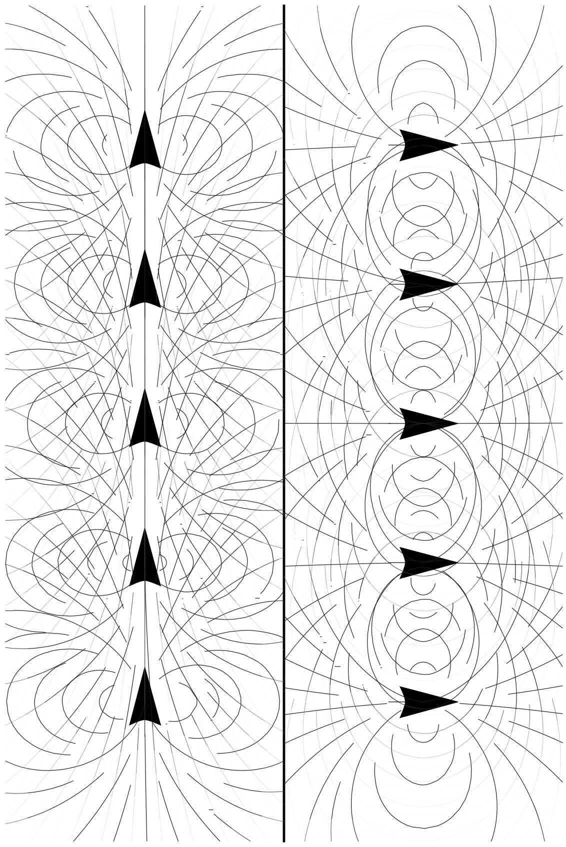

Figure 2.4: Field configurations for two arrangements of magnetic moments. In the stacked configuration (left), the field at a moments position has the same direction as the moment. In the non-stacked (right) configuration, the field has the opposite direction.

was introduced. The success of this formulation depends on the possibility to efficiently calculate this tensor and the global integration. This is, in general, not possible analytically, and numerically only when the integral in equation (2.30) can be replaced by a convolution operation (and therefore application of fast Fourier methods).

It can be seen from equation (2.23), that the parallel alignment of magnetic moments (resulting from the exchange interaction) is only preferred in such a configuration where the dipolar field acting on a moment has the same direction as all the moments. This is only possible when the individual moments are stacked along their direction, whereas a configuration where all the moments are rotated by 90°, while still satisfying exchange, would lead to strong fields and therefore (via equation (1.6)) high energy. This is exemplified in figure 2.4.

This gives rise to **shape anisotropy**, where the shape of the object determines preferred directions of magnetization. Generally, following the argumentation from the paragraph above, the magnetization prefers orientations along the axis/axes of longest extent of an object (*cf.* a bar magnet).

Much like the crystalline anisotropy in subsection 2.2.4, this anisotropy can in principle be modeled similarly to equation (2.18) (although the functional behavior is not the same), giving rise to an anisotropy constant. Both these anisotropies then yield a combined preferred direction of magnetization and a combined effective anisotropy constant K_{eff}. Equation (1.3) then provides a measure of how fast (or on which length scale) those anisotropies, that combat exchange, can change the orientation of the magnetization.

Chapter 3: The spin drift-diffusion model

3.1 Spin accumulation and diffusion

In 1988, **giant magnetoresistance (GMR)** was independently discovered by two groups [18, 19]. Aside from the technological implications, its theoretical modelling provides a reasoning behind the concept of *spin accumulation* that goes beyond the early *two-channel model* by N. F. Mott [78]. Differences in the density of states, depending on the conduction electron's spin, lead to back-scattering of currents at the boundaries of magnetic phases [79]. This results in different conductivities in the spin channels on both sides of the interface, leading to an accumulation of electrons with one spin configuration. This effectively creates a mismatch in the chemical potential μ of the two channels in the whole heterostructure. The concept of a *dynamical* (in the sense that it only exists when a current is imprinted onto the system) spin accumulation was put on proper footing by van Son *et al.* [80]. The difference

$$\Delta\mu\left[\{x_w\}\right] = \mu^{\uparrow}\left[\{x_w\}\right] - \mu^{\downarrow}\left[\{x_w\}\right], \tag{3.1}$$

is then the **spin accumulation (SA)**. In the case of no heterostructure, or at infinite distance from the interface (in reality, even at rather small distance), the spin accumulation has decayed to zero due to spin-flip scattering. Figure 3.1 shows the SA in the vicinity of an interface.

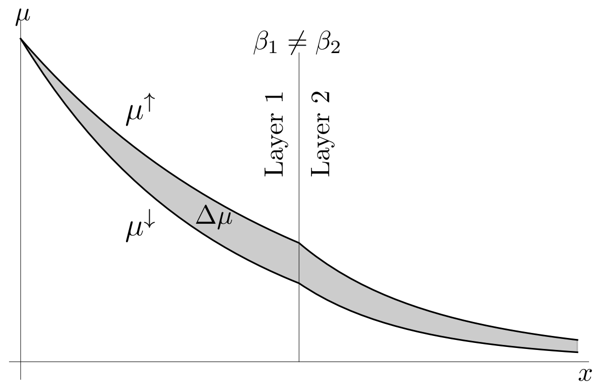

Figure 3.1: Electrochemical potentials of two spin channels and the resulting spin accumulation according to equation (3.1) at an interface.

The SA will be represented by $\vec{s}\left[\vec{x}\right]$ in the equations hereafter. As the spin accumulation results in a spin population shifted from equilibrium (*i. e.* the static spin polarization), it behaves like an effective field. Therefore, s has the unit of A/m.

3.2 The spin drift-diffusion model

The spin accumulation can be thought of as a transport property, and as such can be modeled with a Boltzmann-type transport equation [81],

$$\frac{\partial s_p\left[\{x_w\},t\right]}{\partial t} = -\frac{\partial j^{\mathrm{s}}_{pq}\left[\{x_w\},t\right]}{\partial x_q} - \frac{J}{\hbar}\varepsilon_{pqr}\, s_q\left[\{x_w\},t\right]\, m_r\left[\{x_w\},t\right] - \frac{s_p\left[\{x_w\},t\right]}{\tau_{\mathrm{sf}}}. \tag{3.2}$$

Here, J is the **coupling strength**, measured in J, from the SA to the magnetization, and τ_{sf} is the **spin-flip time**. $\widehat{j^{\mathrm{s}}}$ is the **spin current density** tensor; the index p designates the direction of spin and the index q designates the direction of flow. This equation then incorporates drift, diffusion (both as part of the current) and two relaxation terms. The first term is the torque exerted by the magnetization, and the second a phenomenological damping. This was proposed by Zhang *et al.* [82]. They modeled the necessary current density as

$$j^{\mathrm{s}}_{pq}\left[\{x_w\},t\right] = 2\;\beta\;C_0\frac{\mu_{\mathrm{B}}}{e}m_p\left[\{x_w\},t\right]\frac{\partial u\left[\{x_w\},t\right]}{\partial x_q} - 2\;D_0\frac{\partial s_p\left[\{x_w\},t\right]}{\partial x_q}. \tag{3.3}$$

Here, $u\left[\vec{x}\right]$ is the electrostatic potential, C_0 is the **conductivity divided by two** (measured in S/m), D_0 is the **electronic diffusion constant** (measured in m^2/s), β is the dimensionless **conductive electronic polarization**, and β' the dimensionless **diffusive electronic polarization**. $\beta \neq \beta'$ in general, but is often assumed to be equal. Solving equation (3.2) and 3.3 for s necessitates knowledge of the local potential. Alternatively, the continuity equation

$$\frac{\partial j^{\mathrm{e}}_p\left[\{x_w\},t\right]}{\partial x_p} = 0, \tag{3.4}$$

resulting from charge conservation, can be solved. The **charge current density** $\vec{j}^{\mathrm{e}}$ is modeled as

$$j^{\mathrm{e}}_p\left[\{x_w\},t\right] = -2\;C_0\frac{\partial u\left[\{x_w\},t\right]}{\partial x_p} + 2\;\beta'\;D_0\frac{e}{\mu_{\mathrm{B}}}m_q\left[\{x_w\},t\right]\frac{\partial s_q\left[\{x_w\},t\right]}{\partial x_p}. \tag{3.5}$$

Additionally, both currents have to obey natural boundary conditions, or rather, two variants of the same condition. The boundary condition for the charge current is the *Neumann condition*

$$n_p\left[\{x_w\}\right]\frac{\partial u\left[\{x_w\},t\right]}{\partial x_p} = 0, \tag{3.6}$$

which is the same as for the magnetization, equation (2.17). This means that no charge current can enter or leave the system, except where it is forced to do. The boundary condition for the spin accumulation current is, quite unsurprisingly,

$$n_q\left[\{x_w\}\right]\frac{\partial s_p\left[\{x_w\},t\right]}{\partial x_q} = 0, \tag{3.7}$$

which states exactly the same for the SA. Via the Einstein relation [83], the spin-flip time can be translated into a corresponding **spin-flip length**,

$$\lambda_{\mathrm{sf}} = \sqrt{2\;D_0\;\tau_{\mathrm{sf}}}. \tag{3.8}$$

Measurements of τ_{sf} yield a time scale for the relaxation process of the SA that is many orders of magnitude below the one for the magnetization. Therefore, it is possible to consider the static case where equation (3.2) is set to zero (*adiabatic approximation*).

Inserting equation (3.5) and (3.3) into (3.4) and (3.2) yields a coupled system of equations. By employing proper initial and boundary conditions, this system can be solved for any configuration of $\vec{m}\,[\vec{x}]$, thereby providing the fields of $u\,[\vec{x}]$, the potential in the material, and $\vec{s}\,[\vec{x}]$. This will be shown in subsection 4.2.6 and 4.2.7.

3.3 Spin torque

As the SA behaves like an effective field, it is expected for it to exert a torque onto the local magnetization. “Inverting” the torque term from equation (3.2) yields

$$\frac{\partial m_p\left[\{x_w\}, t\right]}{\partial t} = -\frac{J}{\hbar\, M_{\mathrm{S}}} \varepsilon_{pqr}\, m_q\left[\{x_w\}, t\right]\; s_r\left[\{x_w\}, t\right], \tag{3.9}$$

the **spin torque**, *i.e.* the torque exerted by the spin accumulation upon the magnetization. Comparison with the LLG, equation (2.4), then establishes an effective field

$$H_p^{\mathrm{ST}}\left[\{x_w\}, t\right] = \frac{J}{\hbar\, \mu_0\, \gamma_{\mathrm{e}}\, M_{\mathrm{S}}} s_p\left[\{x_w\}, t\right]. \tag{3.10}$$

This field is added to the other contributions in the LLG, with the salient difference, that it is now in principle a dynamic one. With the SA being calculated as stated above, the new magnetization can then be calculated, and inserted into the drift-diffusion model again (see Abert *et al.* [84, 85]). As the SA influences the magnetization, the magnetization influences the SA.

3.4 Spin-orbit coupling

The well known *Hall effect* [15] is actually only a special case of a complete class of effects that describe interactions between currents and magnetic fields. Of special interest have always been the so-called anomalous Hall effects. The **spin-Hall effect (SHE)** was first described by R. Karplus and J. M. Luttinger [86] to be based upon spin-orbit coupling. The total orbital momentum of the conduction electrons is the responsible quantity for that effect. It is not limited to ferromagnets, but has also been found in paramagnets, where a charge current is split into spin currents due to different scattering of the spin directions (the initial experimental confirmation by Y. K. Kato [87] was in a semiconductor). In a simple qualitative picture, this coupling, or rather the energy difference arising from it, can be given by [30, pp. 61–63]:

$$\mathcal{E}_{\mathrm{SOC}} \approx \frac{\mu_0\, \mu_{\mathrm{B}}^2\, Z^4}{\pi\, a_0^3\, \hbar^2} l_p\, s_p, \tag{3.11}$$

where a_0 is Bohr's radius and, most important, Z is the atomic number. $\vec{l}$ and $\vec{s}$ are the orbital angular momentum and the spin, respectively. The coupling is therefore generally large for heavier metals; indeed, most metals with large coupling are $5d$-transition metals.

Independent of the actual mechanics behind SHE, a simple phenomenological description is given by M. I. Dyakonov [88], where it is modeled as a spin current as a result of a charge current;

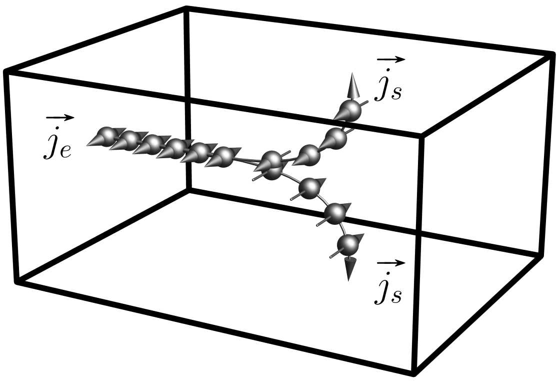

Figure 3.2: The effect of the SHE shown schematically. A charge current $\vec{j}^{\mathrm{e}}$ is split up into spin currents.

$$j^{\mathrm{s}}_{qp} = j^{\mathrm{s}}_{qp} + \frac{\mu_{\mathrm{B}}}{e}\Theta_{\mathrm{SH}}\,\varepsilon_{qpr}\,j^{\mathrm{e}}_{r}, \tag{3.12}$$

where Θ_{SH} denotes the dimensionless **spin-Hall angle**, (*cf.* conventional Hall angle) which is then a parameter measuring the spin-current-generating power of a material. The interaction defined in equation (3.12) is shown schematically in figure 3.2.

As per the Onsager relations [89], an inverse effect, the **inverse SHE (ISHE)** [90], also exists. Per [88], this can be written as

$$j^{\mathrm{e}}_{p} = j^{\mathrm{e}}_{p} - \frac{e}{\mu_{\mathrm{B}}}\Theta_{\mathrm{SH}}\,\varepsilon_{pqr}\,j^{\mathrm{s}}_{qr} \tag{3.13}$$

The way that these equations should be understood, is that they are inserted in equation equation (3.2) and 3.4, and then the current definitions from equation equation (3.3) and 3.5 used in them. In that way a circular relation, with a charge current generating a spin current, which itself will generate a charge current, is avoided.

Chapter 4: Numerical computation using finite elements

The theory introduced in chapters 2 and 3 is the basis for conducting actual calculations of systems. As is usually the case, such calculations can no longer be performed analytically. Therefore, numerical means need to be applied. The spatial and time integration will be treated in the following sections.

The generally used computational method approximates differential operators as difference operators, where the difference is then some small, but finite value. Hence it is called **finite-difference method (FDM)**. Such an implementation discretizes the fields encountered in such a way that they are defined on some, regularly spaced, support points. The space between those support points can then be Voronoi tesselated [91] into regular cuboids, with the field represented by an effective, piecewise constant, function.

While FDM generally offers efficient solving behavior, it exhibits some significant **downsides**:

1. The requirement to represent the considered volume as an aggregate of cuboids leads to a *blocky* representation of any shapes which are not cuboid themselves. This is obviously the case for any cylindrically or spherically shaped objects, but even simple angles are turned into step functions. The **shape fidelity** of FDM is limited, and a proper representation can necessitate a fine discretization. This can make the numerical algorithms very costly.
2. The concept of a surface, be it boundaries or interfaces, does not really exist. It can be argued that the boundaries of the individual cuboids are surfaces, but they are not accessible in computations. Only the support points can be accessed. This can lead to **problems wherever interfaces exist**, especially for cases where interface interactions are modelled (see, *e. g.*, Suess *et. al* [92] for such a case).
3. The support points are **regularly spaced**. Since the interactions that need to be discretized may not be equal everywhere in the simulated volume(*e. g.* different exchange lengths (equation (1.3))), or the requirements on numerical fidelity may not be constant, this can lead to either low computational efficiency (for overall small spacing) or increased errors (for overall large spacing).

For spintronic applications, especially the problems with surfaces are a major obstacle, as there heterostructures with material interfaces are a common appearance. The **finite-element method (FEM)** offers solutions to these problems. But these increased capabilities come with a cost: the method is generally computationally costly. This is especially true for the demagnetization field, where a different formulation to subsection 2.2.5 has to be employed.

4.1 Finite-element method

An FEM is not a method for solving differential equations. Instead, it employs a different discretization approach as well as a different mathematical method to solve equations in general.

A general treatment of FEM, including the steps presented herein, can be found in, *e. g.*, C. Johnson [93]. An abridged recipe is:

1. Prepare a **triangulation** of the considered system Ω. In three dimensions, this means decomposing the system into a mesh of tetrahedra $\{K^i\} \in \Omega$. The mechanics of this process are outside of the scope of this work. A commonly employed method, also used in this work, is the NETGEN algorithm [94]. *N. b.* that the decomposition has to be fine enough to still be in the micromagnetic regime, *cf.* figure 1.4. It has to be noted that the triangulation does not need to be with tetrahedra, also other shapes are possible (like hexahedra, cuboids, that produce the same discretization as FDM).

2. Choose a suitable set of **basis functions** $\psi[\vec{x}]$. A common choice are polynomials of degree n, where usually $n = 1$ for the interesting fields and $n = 0$ for material parameters.

3. Construct **solution functions** $\vec{\phi}[\vec{x}]$ from the $n = 1$ basis functions such that

$$\phi_p^i[\{x_w\}] = \sum_{j=1}^{4} \eta_p^j \, \psi^{ij}[\{x_w\}] \,. \tag{4.1}$$

   These functions have to be smooth in every K^i, which they are per construction. They also have to obey any boundary conditions. For each vertex j of a tetrahedron i, a polynomial $\psi^{ij}[\vec{x}]$ is constructed, with a value of unity on that vertex and a value of zero on every other one. This is depicted in figure 4.1 for the 2D case. A linear combination of four polynomials (one for each vertex), with coefficients η^j (those may be vector or scalar), is then the basis function ϕ^i for one K^i such that there are as many solution functions as there are tetrahedra. This means that the solution is approximated by affine functions in each of the tetrahedra.

4. Construct **material functions** $\vec{\xi}[\vec{x}]$ from the $n = 0$ basis functions such that

$$\xi_p^i[\{x_w\}] = \eta_p^i \, \zeta[\{x_w\}]. \tag{4.2}$$

   $\zeta[\vec{x}] = 1$ is a constant function, that is modulated by η^i on K^i such that $\vec{\xi^i}[\{x_w\}]$ is piecewise constant.

5. Construct **field functions** from the fields required for solution akin to equation (4.1). The coefficients are selected in such a way as to directly provide the function value on each of the tetrahedral vertices. Construct **material functions** from the material parameters required for solution akin to equation (4.2). The coefficients are selected in such a way as to directly provide the parameter value on each of the tetrahedra. This means that the fields are approximated by affine functions in each of the tetrahedra, while the material parameters are approximated by constant functions.

All fields introduced in section 2.2 therefore need to be brought into an FEM formulation, which is done in the following sections.

By doing so, it may be possible to turn the considered problem into a variational problem according to the *Ritz method* [95]. It is not *a priori* clear that this is possible and the variational problem is indeed equivalent to the differential equation. The existence of solutions of the spin-diffusion model in such a formulation was proven by C. J. Garcia-Cervera and X. P. Wang [96]. Doing so, the initial problem can be written as a matrix equation, *i. e.* a system of equations. That matrix is a sparse one, as per the construction mentioned above, products of the basis function equal zero in most cases. The matrix equation can then be solved by employing general linear algebra methods for sparse matrices (see, *e. g.*, W. H. Press *et al.* [97, pp. 75–93]).

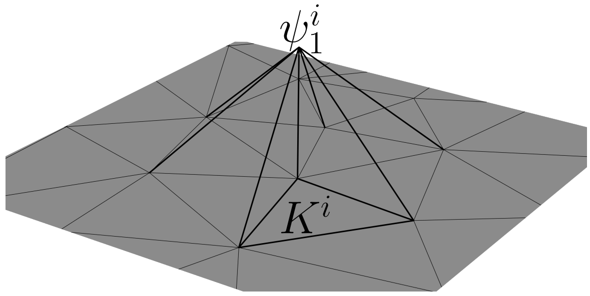

Figure 4.1: The scalar vertex polynomial ψ_1^i for the first vertex of the triangle K^i, with the height above the discretized plane showing the function value. The complete basis function ϕ^i is then a sum of the three vertex polynomials.

In the following subsections, the arguments of the functions are left out for the sake of brevity. Generally, in those derivations, systems with interfaces are considered, such that the material parameters can change inside the system. This is especially important for the currents. This means that the parameters can no longer be treated as constants, but have to be considered in differentiations and integrations — they are in principle functions and have the position as argument. This also means that the parameters are not bound to any constraints, as the adherence to the boundary conditions and conditions of smoothness and continuity are guaranteed by the basis functions.

4.2 Spatial integration

4.2.1 Zeeman field

The Zeeman field is discretized simply according to equation (4.1), where the $\vec{\eta}^j$ are the field values at each vertex.

4.2.2 Exchange field

The starting point is equation (2.16):

$$H_p^{\mathrm{ex}} = \frac{2}{\mu_0\, M_{\mathrm{S}}} \frac{\partial}{\partial x_q} \left(A_{\mathrm{ex}} \frac{\partial m_p}{\partial x_q} \right). \tag{4.3}$$

This is multiplied by a test function $\vec{v}[\vec{x}]$ (which is a numerical approximation of $\overrightarrow{H^{\mathrm{ex}}}$) and integrated over the complete volume Ω to get:

$$\int_{\Omega} H_p \, v_p \, \mathrm{d}\Omega = \frac{2}{\mu_0} \int_{\Omega} \frac{1}{M_\mathrm{S}} \frac{\partial}{\partial x_q} \left(A_\mathrm{ex} \frac{\partial m_p}{\partial x_q} \right) v_p \, \mathrm{d}\Omega. \tag{4.4}$$

To be able to use equation (4.1) to express the magnetization with the basis functions, the second derivative needs to be eliminated. In a basis of affine functions it would yield zero, thereby rendering the discretization useless. It will therefore be a common theme in the following subsections to transform the integrals. Applying *Green's theorem* ([9, pp. 35–37]), the right side can be transformed to yield

$$\int_{\Omega} H_p \, v_p \, \mathrm{d}\Omega = \frac{2}{\mu_0} \left(\int_{\partial\Omega} \frac{A}{M_\mathrm{S}} \frac{\partial m_p}{\partial x_q} v_p \, n_q \, \mathrm{d}\partial\Omega - \int_{\Omega} A \frac{\partial m_p}{\partial x_q} \frac{\partial}{\partial x_q} \left(\frac{1}{M_\mathrm{S}} v_p \right) \mathrm{d}\Omega \right). \tag{4.5}$$

But since equation (2.17) provides a necessary boundary condition, the boundary integral yields zero on boundaries where magnetization exists. On boundaries of subvolumes where the magnetization does not exist (*i. e.* $\vec{m} = 0$), the boundary integral yields zero too. Still, in this formulation, differentiations exist that may not be doable as the fields are only piecewise differentiable. This is especially true for the surface normal vectors $\vec{n}$, that are, for all intents and purposes, material parameters, and piecewise constant. Instead, the term inside the integral is decomposed into a sum of the terms for each K^k, as each of these pieces can be processed:

$$\sum_k \int_{\Omega} H_p^k \, v_p^k \, \mathrm{d}\Omega = -\frac{2}{\mu_0} \sum_k \int_{\Omega} A \frac{\partial m_p^k}{\partial x_q} \frac{\partial}{\partial x_q} \left(\frac{1}{M_\mathrm{S}} v_p^k \right) \mathrm{d}\Omega. \tag{4.6}$$

The fields and material constants are now expressed with the basis functions to yield

$$\sum_i \chi_p^i \sum_k \int_{\Omega} \psi^{ik} \, \psi^{jk} \, \mathrm{d}\Omega = \sum_i \mu_p^i \sum_k -\frac{2}{\mu_0} \int_{\Omega} \frac{A^k}{M_\mathrm{S}^k} \frac{\partial \psi^{ik}}{\partial x_q} \frac{\partial \psi^{jk}}{\partial x_q} \mathrm{d}\Omega, \tag{4.7}$$

where $\vec{\chi^i}$ is the coefficient vector of the exchange field, while $\vec{\mu^i}$ is the coefficient vector of the magnetization. This exploits the fact that all the coordinate dependence is limited to the basis functions. This can be written as the matrix equation

$$\sum_i A^{ij} \, \chi_p^i = \sum_i B^{ij} \, \mu_p^i, \tag{4.8}$$

where the integrals are treated as matrices. This system then needs to be inverted to provide $\vec{\chi^i}$. The integrals can be calculated analytically (but are computed numerically in computations, as it is faster but still, except for rounding errors, exact), as the basis functions are polynomials and are zero almost everywhere except for small tetrahedral volumes. The system that needs to be solved here is therefore of size n^2, but the matrices are sparse. The necessary operators, and the inversion, need only to be constructed once, as they are dependent only on the geometry of the problem.

4.2.3 Crystalline anisotropy

The starting point is equation (2.20):

$$H_p = \frac{2}{\mu_0\ M_\mathrm{S}} e_q\ m_q\ e_p \left(K^1 + 2\ K^2 \left(e_q\ m_q\right)^2\right). \tag{4.9}$$

As before, this is multiplied by a test function $\vec{v}[\vec{x}]$ and integrated over the complete volume Ω to get:

$$\int_\Omega H_p\ v_p\ \mathrm{d}\Omega = \int_\Omega \frac{2}{\mu_0\ M_\mathrm{S}} e_q\ m_q\ e_p \left(K_1 + 2\ K_2 \left(e_q\ m_q\right)^2\right) v_p\ \mathrm{d}\Omega. \tag{4.10}$$

Again, the term inside the integral is decomposed into a sum of the terms for each K^k, as each of these pieces can be processed:

$$\sum_k \int_\Omega H_p^k\ v_p^k\ \mathrm{d}\Omega = \frac{2}{\mu_0\ M_\mathrm{S}} \sum_k \int_\Omega e_q\ m_q\ e_p^k \left(K_1 + 2\ K_2 \left(e_q\ m_q\right)^2\right) v_p^k\ \mathrm{d}\Omega. \tag{4.11}$$

Again, the fields and material constants are expressed with the basis functions to yield

$$\begin{aligned}
&\sum_i \chi_p^i \sum_k \int_\Omega \psi^{ik}\ \psi^{jk}\ \mathrm{d}\Omega = \\
&\sum_i \mu_q^i \sum_k \frac{2}{\mu_0} \left(\int_\Omega \frac{e_q^k\ e_p^k\ K_1^k}{M_\mathrm{S}^k} \psi^{ik}\ \psi^{jk}\ \mathrm{d}\Omega + \sum_{l,m} 2\ \mu_r^l\ \mu_s^m \int_\Omega \frac{e_q^k\ e_r^k\ e_s^k\ e_p^k\ K_2^k}{M_\mathrm{S}^k} \psi^{lk}\ \psi^{mk}\ \psi^{ik}\ \psi^{jk}\ \mathrm{d}\Omega \right).
\end{aligned} \tag{4.12}$$

This can be written that as the matrix equation

$$\sum_i A^{ij}\ \chi_p^i = \sum_i C_{pq}^{ij} \mu_q^i + \sum_{i,l,m} D_{pqrs}^{ijlm}\ \mu_r^l\ \mu_s^m \mu_q^i. \tag{4.13}$$

For the sake of brevity, the derivation of the cubic anisotropy is skipped.

4.2.4 Demagnetization field

Equation (2.30) provides a solution for the demagnetization field. As has been mentioned there, this solution is only feasible if the integral can be computed efficiently. This is not possible for FEM.

Directly solving equation (2.27) in an FEM formulation may seem a proper way, but the physical boundary condition for the potential exists only at infinity. This would mean discretizing the space outside the magnetic material, the “airbox”, for a finite distance where the boundary condition is enforced at. That distance is selected such that the computation is sufficiently close to the true result. While this is indeed a possible method (*airbox solver*), depending on the evaluated geometry, the computation time may increase by orders of magnitude.

D. Fredkin and T. Koehler [98] presented an alternative approach. Equation (2.27) exists in three distinct regions: 1) inside the magnetic material, with its form unchanged; 2) outside of the magnetic material, reduced to *Laplace's equation*, and 3) at the boundary, where a discontinuity exists. The global solution consists of a homogeneous and inhomogeneous part. $U[\vec{x},t]$ is now linearily decomposed $U[\vec{x},t] \to U^{\mathrm{i}}[\vec{x},t] + U^{\mathrm{h}}[\vec{x},t]$, the **i**nhomogeneous part inside the material (such that $U^{\mathrm{i}}[\vec{x},t] = 0$ outside of it), and the **h**omogeneous part everywhere. This method is generally known as **Fredkin-Koehler method** or **hybrid FEM/BEM** (for *boundary-element method*).

The starting point is equation (2.27), inside of the magnetic material,

$$\frac{\partial}{\partial x_p}\left(M_{\mathrm{S}}\, m_p - \frac{\partial U^{\mathrm{i}}}{\partial x_p}\right) = 0. \tag{4.14}$$

The boundary conditions that are inevitably needed follow from classical electrodynamics (*e. g.* [9, pp. 16–19]). The important one is

$$B_p^-\, n_p = B_p^+\, n_p \tag{4.15}$$

where the signs denote inside ($-$) or outside ($+$) of the material. Since, per construction, only U^{i} is generated by magnetization, $U_-^{\mathrm{i}} = U_-^{\mathrm{h}}$, and hence $U_+^{\mathrm{h}} = 2\ U_-^{\mathrm{i}}$. The total potential has to be continuous at the boundary, but the individual parts are not. Using equation (2.26), the first boundary condition translates to

$$\frac{\partial U^{\mathrm{i}}}{\partial x_p} n_p = M_{\mathrm{S}}\, m_p\, n_p. \tag{4.16}$$

As before, equation (4.14) is multiplied by a test function $v[\vec{x}]$ and integrated over the complete volume Ω to get:

$$\int_\Omega \frac{\partial^2 U^{\mathrm{i}}}{\partial x_p\, \partial x_p} v\ \mathrm{d}\Omega = \int_\Omega \frac{\partial\left(M_{\mathrm{S}}\, m_p\right)}{\partial x_p} v\ \mathrm{d}\Omega. \tag{4.17}$$

Applying *Green's theorem* ([9, pp. 35–37]), the left side can be transformed to yield

$$\int_{\partial\Omega} \frac{\partial U^{\mathrm{i}}}{\partial x_p} n_p\ v\ \mathrm{d}\partial\Omega - \int_\Omega \frac{\partial U^{\mathrm{i}}}{\partial x_p} \frac{\partial v}{\partial x_p} \mathrm{d}\Omega = \int_\Omega \frac{\partial\left(M_{\mathrm{S}}\, m_p\right)}{\partial x_p} v\ \mathrm{d}\Omega. \tag{4.18}$$

Using the boundary condition, this can be reworked to

$$\int_\Omega \frac{\partial U^{\mathrm{i}}}{\partial x_p}\,\frac{\partial v}{\partial x_p}\mathrm{d}\Omega = \int_{\partial\Omega} M_{\mathrm{S}}\; m_p\; n_p\; v\;\mathrm{d}\partial\Omega - \int_\Omega \frac{\partial\left(M_{\mathrm{S}}\; m_p\right)}{\partial x_p} v\;\mathrm{d}\Omega. \tag{4.19}$$

Again using *Green's theorem*, the right side can be transformed to yield

$$\int_\Omega \frac{\partial U^{\mathrm{i}}}{\partial x_p}\,\frac{\partial v}{\partial x_p}\mathrm{d}\Omega = \int_\Omega M_{\mathrm{S}}\; m_p \frac{\partial v}{\partial x_p}\mathrm{d}\Omega. \tag{4.20}$$

Again, the fields and material constants are expressed with the basis functions, and the sum over all K^k, to yield

$$\sum_i v^i \sum_k \int_\Omega \frac{\partial \psi^{ik}}{\partial x_p}\,\frac{\partial \psi^{jk}}{\partial x_p}\mathrm{d}\Omega = \sum_i \mu_p^i \sum_k \int_\Omega M_{\mathrm{S}}^k\; \psi^{ik}\frac{\partial \psi^{jk}}{\partial x_p}\mathrm{d}\Omega. \tag{4.21}$$

This can be written as the matrix equation

$$\sum_i E^{ij}\; v^i = \sum_i F_p^{ij}\; \mu_p^i. \tag{4.22}$$

Thus, calculation of U^{i} is possible. *Green's theorem*, now applied to U^{h}, yields

$$U_-^{\mathrm{h}}\left[\{x_w\}\right] = \frac{1}{4\pi}\int_{\partial\Omega} U_-^{\mathrm{h}}\left[\{y_w\}\right]\frac{\partial}{\partial y_q}\left(\frac{1}{\sqrt{(x_q - y_q)(x_q - y_q)}}\right) n_q\;\mathrm{d}\left[\{y_w\}\in\partial\Omega\right], \tag{4.23}$$

where the fact is exploited, that *Green's function* for *Poisson's equation* is not uniquely defined. In this way, one of the boundary terms can be eliminated. The equation is obviously a *catch-22*, so this needs to be repaired. Since at the boundary, the total potential is generated by equation (4.14), $U^{\mathrm{h}} = U^{\mathrm{i}}$.

For computational reasons, U^{h} is not computed everywhere directly, but only at the boundaries. This seems to be another *catch-22*. The form at hand computes the potential inside the volume (the left side) via the potential at its boundary (the right side). To compute the potential at the boundary, a limit has to be taken. A detailed derivation can be found *e. g.* in [99, pp. 110–120], but this yields:

$$\begin{aligned} &U_-^{\mathrm{h}}\left[\{x_w\}\in\partial\Omega\right] = \\ &\frac{1}{4\,\pi}\left(\int_{\partial\Omega} U_-^{\mathrm{i}}\left[\{y_w\}\right]\frac{\partial}{\partial y_q}\left(\frac{1}{\sqrt{(x_q - y_q)(x_q - y_q)}}\right) n_q\;\mathrm{d}\partial\left[\{y_w\}\in\partial\Omega\right] - \kappa\; U_-^{\mathrm{i}}\left[\{x_w\}\in\partial\Omega\right]\right), \end{aligned} \tag{4.24}$$

where κ denotes the solid angle subtended at the boundary (2π for a smooth surface). This operation can be easily discretized as

$$
\begin{aligned}
&U^{\mathrm{h}}_{-}\left[\{x_w\} \in \partial\Omega\right] = \\
&\sum_j \upsilon^j \sum_k \frac{1}{4\,\pi} \int_{\partial\Omega} \psi^{jk} \frac{\partial}{\partial y_q} \left(\frac{1}{\sqrt{(\xi^{ij}_q - y_q)(\xi^{ij}_q - y_q)}} \right) n_q \, \mathrm{d}\partial\left[\{y_w\} \in \partial\Omega\right] - \frac{\kappa}{4\,\pi} \upsilon^i \\
&= \beta^i = \sum_j G^{ij}\ \upsilon^j - \frac{\kappa}{4\,\pi} \upsilon^i
\end{aligned}
\tag{4.25}
$$

where $\vec{\beta}$ is the coefficient vector for the boundary values. The ξ's are the distances between the considered points i and j. Thus, calculation of U^{h} is possible at the boundary. Equation (2.27), reduced to *Laplace* form, is the next step:

$$
\frac{\partial^2 U^{\mathrm{h}}}{\partial x_p \, \partial x_p} = 0. \tag{4.26}
$$

This is multiplied by a test function $v\left[\vec{x}\right]$ and integrated over the complete volume Ω. *Green's theorem* is applied, and the fields and material constants are expressed by the basis functions to yield:

$$
\sum_i \upsilon^i \sum_k \int_{\Omega} \frac{\partial \psi^{ik}}{\partial x_p} \, \frac{\partial \psi^{jk}}{\partial x_p} \, \mathrm{d}\Omega = \sum_i \beta^i \sum_k \int_{\partial\Omega} \frac{\partial \psi^{ik}}{\partial x_p} n_p \, \psi^{jk} \, \mathrm{d}\partial\Omega. \tag{4.27}
$$

This can be written as the matrix equation

$$
\sum_i E^{ij}\ \upsilon^i = \sum_i H^{ij}\ \beta^i. \tag{4.28}
$$

To transform the potential values into a demagnetization field, $\vec{H} = -\vec{\nabla}\, U$ needs to be transformed into an FEM formulation. This yields:

$$
\sum_i \chi^i_p \sum_k \int_{\Omega} \psi^{ik}\ \psi^{jk} \, \mathrm{d}\Omega = \sum_i \upsilon^i \sum_k \int_{\Omega} -\frac{\partial \psi^{ik}}{\partial x_p} \psi^{jk} \, \mathrm{d}\Omega, \tag{4.29}
$$

or, in matrix form,

$$
\sum_i A^{ij}\ \chi^i_p = \sum_i J^{ij}\ \upsilon^i. \tag{4.30}
$$

To end with the proper demagnetization field, a total of three matrix equations have to be solved, and a fourth calculated. It is pretty obvious that this process is considerably more involved and takes more computational effort than the simple FDM implementation in equation (2.30). Additionally, the matrix in equation (4.25) is dense, which is problematic for numerical implementation due to memory constraints. To reduce the storage size, $\mathcal{H}^2$-compression [100] is implemented in application.

4.2.5 Oersted field

Directly solving equation (2.6), as simple as it seems, suffers from the same problem as the demagnetization field: The boundary condition is only defined at infinity. The numerical treatment of the Oersted field was delayed until the *Fredkin-Koehler method* was introduced, as it is the solution method for the Oersted field too. Equation (2.6) also exists in the same three distinct regions, and can be treated identically. The analogy is only briefly shown, and the derivation not repeated.

The starting point is equation (2.6), inside of the charge-current carrying volume:

$$\varepsilon_{pqr} \frac{\partial H_r^{\mathrm{i}}}{\partial x_q} = \mu_0 \, j_p, \tag{4.31}$$

to which another cross product is applied:

$$\varepsilon_{lnp} \, \varepsilon_{pqr} \frac{\partial^2 H_r^{\mathrm{i}}}{\partial x_q \, \partial x_n} = \mu_0 \, \varepsilon_{lnp} \frac{\partial j_p}{\partial x_n}. \tag{4.32}$$

Eliminating the double cross-products leads to

$$-\frac{\partial^2 H_p^{\mathrm{i}}}{\partial x_q \, \partial x_q} = \mu_0 \, \varepsilon_{pqr} \frac{\partial j_r}{\partial x_q}, \tag{4.33}$$

where one of the terms was eliminated since a magnetic field is required to be source-free. As before, this is multiplied by a test function $v\,[\vec{x}]$ and integrated over the complete volume Ω to get:

$$-\int_\Omega \frac{\partial^2 H_p^{\mathrm{i}}}{\partial x_q \, \partial x_q} v_p \, \mathrm{d}\Omega = \mu_0 \int_\Omega \varepsilon_{pqr} \frac{\partial j_r}{\partial x_q} v_p \, \mathrm{d}\Omega. \tag{4.34}$$

Applying *Green's theorem* ([9, pp. 35–37]), both sides can be transformed to yield

$$\int_\Omega \frac{\partial H_p^{\mathrm{i}}}{\partial x_q} \frac{\partial v_p}{\partial x_q} \mathrm{d}\Omega = -\mu_0 \int_\Omega \varepsilon_{pqr} \, j_r \frac{\partial v_p}{\partial x_q} \mathrm{d}\Omega. \tag{4.35}$$

This is the analogon to equation (4.20). Everything else in subsection 4.2.4 can be applied similarly, by replacing $U^{\mathrm{i}} \to H_p^{\mathrm{i}}$ and $U^{\mathrm{h}} \to H_p^{\mathrm{h}}$. The steps are not repeated here. Harmonic behavior of the current density can be relegated to a multiplier of the computed field, then one-time computation of the field suffices.

4.2.6 Charge current

The starting point is equation (3.4), which is inserted into it the charge current equation (3.13) with the spin-Hall contribution, and the charge current equation (3.5) and spin current equation (3.3) from the spindrift-diffusion model, to yield

$$\begin{aligned}-\frac{\partial}{\partial x_p}\left(C_0\frac{\partial u}{\partial x_p}\right)+\frac{e}{\mu_\mathrm{B}}\left(\frac{\partial}{\partial x_p}\left(\beta'\ D_0\frac{\partial s_q}{\partial x_p}m_q\right)\right.\\-\frac{\partial}{\partial x_p}\left(\beta\ C_0\ \Theta_\mathrm{SH}\ \varepsilon_{pqr}\ m_q\frac{\partial u}{\partial x_r}\right)+\left.\frac{\partial}{\partial x_p}\left(D_0\ \Theta_\mathrm{SH}\ \varepsilon_{pqr}\frac{\partial s_q}{\partial x_r}\right)\right)=0,\end{aligned} \tag{4.36}$$

the differential equation that needs to be solved. Again multiplying by a test function $v\left[\vec{x}\right]$ and integrating over the complete volume Ω, leads to

$$\begin{aligned}-\int_\Omega\frac{\partial}{\partial x_p}\left(C_0\frac{\partial u}{\partial x_p}\right)v\ \mathrm{d}\Omega+\frac{e}{\mu_\mathrm{B}}\left(\int_\Omega\frac{\partial}{\partial x_p}\left(\beta'\ D_0\frac{\partial s_q}{\partial x_p}m_q\right)v\ \mathrm{d}\Omega\right.\\-\int_\Omega\frac{\partial}{\partial x_p}\left(\beta\ C_0\ \Theta_\mathrm{SH}\ \varepsilon_{pqr}\ m_q\frac{\partial u}{\partial x_r}\right)v\ \mathrm{d}\Omega+\left.\int_\Omega\frac{\partial}{\partial x_p}\left(D_0\ \Theta_\mathrm{SH}\ \varepsilon_{pqr}\frac{\partial s_q}{\partial x_r}\right)v\ \mathrm{d}\Omega\right)=0.\end{aligned} \tag{4.37}$$

Applying *Green's theorem* ([9, pp. 35–37]) on each integral yields:

$$\begin{aligned}\int_\Omega C_0\frac{\partial u}{\partial x_p}\ \frac{\partial v}{\partial x_p}\mathrm{d}\Omega+\frac{e}{\mu_\mathrm{B}}\left(-\int_\Omega\beta'\ D_0\ m_q\frac{\partial s_q}{\partial x_p}\ \frac{\partial v}{\partial x_p}\mathrm{d}\Omega\right.\\-\int_{\partial\Omega}\beta\ C_0\ \Theta_\mathrm{SH}\ \varepsilon_{pqr}\ m_q\frac{\partial u}{\partial x_r}n_p\ v\ \mathrm{d}\partial\Omega+\int_\Omega\beta\ C_0\ \Theta_\mathrm{SH}\ \varepsilon_{pqr}\ m_q\frac{\partial u}{\partial x_r}\ \frac{\partial v}{\partial x_p}\mathrm{d}\Omega\\+\int_{\partial\Omega}D_0\ \Theta_\mathrm{SH}\ \varepsilon_{pqr}\frac{\partial s_q}{\partial x_r}n_p\ v\ \mathrm{d}\partial\Omega-\left.\int_\Omega D_0\ \Theta_\mathrm{SH}\ \varepsilon_{pqr}\frac{\partial s_q}{\partial x_r}\ \frac{\partial v}{\partial x_p}\mathrm{d}\Omega\right)=0.\end{aligned} \tag{4.38}$$

The two boundary conditions, equation (3.6) and equation (3.7), were used the eliminate two integrals. In principle, the charge boundary condition can be overwritten when a current is applied to the system, but external current is not used in the presented work. Expressing the fields and the potential with the basis functions yields

$$\begin{aligned}&\sum_i\left(v^i\left(\sum_k C_0^k\int_\Omega\frac{\partial\psi^{ik}}{\partial x_p}\ \frac{\partial\psi^{jk}}{\partial x_p}\mathrm{d}\Omega\right.\right.\\&\quad+\mu_q^i\left(\sum_k\frac{e}{\mu_\mathrm{B}}\beta^k\ C_0^k\ \Theta_\mathrm{SH}^k\ \varepsilon_{pqr}\left(\int_\Omega\psi^{ik}\frac{\partial\psi^{ik}}{\partial x_r}\ \frac{\partial\psi^{jk}}{\partial x_p}\mathrm{d}\Omega-\int_{\partial\Omega}\psi^{ik}\frac{\partial\psi^{ik}}{\partial x_r}n_p^k\ \psi^{jk}\ \mathrm{d}\partial\Omega\right)\right)\right)\\&\quad+\sigma_q^i\left(\sum_k\frac{e}{\mu_\mathrm{B}}D_0^k\ \Theta_\mathrm{SH}^k\ \varepsilon_{pqr}\left(\int_{\partial\Omega}\frac{\partial\psi^{ik}}{\partial x_r}n_p^k\ \psi^{jk}\ \mathrm{d}\partial\Omega-\int_\Omega\frac{\partial\psi^{ik}}{\partial x_r}\ \frac{\partial\psi^{jk}}{\partial x_p}\ \mathrm{d}\Omega\right)\right.\\&\quad\left.\left.-\mu_q^i\sum_k\frac{e}{\mu_\mathrm{B}}\beta'^k\ D_0^k\int_\Omega\psi^{ik}\frac{\partial\psi^{ik}}{\partial x_p}\ \frac{\partial\psi^{jk}}{\partial x_p}\mathrm{d}\Omega\right)\right)=0,\end{aligned} \tag{4.39}$$

or, in matrix form,

$$\sum_i K^{ij} v^i + \sum_i L_q^{ij} \sigma_q^i = 0, \tag{4.40}$$

where $\vec{\sigma}$ is the coefficient vector of the spin accumulation, and $\vec{v}$ the coefficient vector of the electric potential. It is important to note here that the magnetization is treated as a material parameter. The solution will be held off until the end of the next subsection, as $\vec{\sigma}$ is currently unknown.

4.2.7 Spin current

The starting point is equation (3.2), that is inserted into the charge current equation (3.12) with the spin-Hall contribution, and the charge current equation (3.5) and spin current equation (3.3) from the spin drift-diffusion model, to yield

$$\begin{aligned} -2\left(\frac{\partial}{\partial x_q}\left(\beta'\ D_0\ \Theta_{\mathrm{SH}}\ \varepsilon_{pqr}\ m_l \frac{\partial s_l}{\partial x_r}\right) - \frac{\partial}{\partial x_q}\left(D_0 \frac{\partial s_p}{\partial x_q}\right)\right. \\ \left. + \frac{\mu_{\mathrm{B}}}{e}\left(\frac{\partial}{\partial x_q}\left(\beta\ C_0\ m_p \frac{\partial u}{\partial x_q}\right) - \frac{\partial}{\partial x_q}\left(C_0\ \Theta_{\mathrm{SH}}\ \varepsilon_{pqr} \frac{\partial u}{\partial x_r}\right)\right)\right) - \frac{J}{\hbar}\varepsilon_{pqr}\ s_q\ m_r - \frac{s_p}{\tau_{\mathrm{sf}}} = 0, \end{aligned} \tag{4.41}$$

the differential equation that needs to be solved. Again multiplying by a test function $\vec{v}\,[\vec{x}]$ and integrating over the complete volume Ω yields

$$\begin{aligned} -2\left(\int_\Omega \frac{\partial}{\partial x_q}\left(\beta'\ D_0\ \Theta_{\mathrm{SH}}\ \varepsilon_{pqr}\ m_l \frac{\partial s_l}{\partial x_r}\right) v_p\ \mathrm{d}\Omega - \int_\Omega \frac{\partial}{\partial x_q}\left(D_0 \frac{\partial s_p}{\partial x_q}\right) v_p\ \mathrm{d}\Omega\right. \\ \left. + \frac{\mu_{\mathrm{B}}}{e}\left(\int_\Omega \frac{\partial}{\partial x_q}\left(\beta\ C_0\ m_p \frac{\partial u}{\partial x_q}\right) v_p\ \mathrm{d}\Omega - \int_\Omega \frac{\partial}{\partial x_q}\left(C_0\ \Theta_{\mathrm{SH}}\ \varepsilon_{pqr} \frac{\partial u}{\partial x_r}\right) v_p\ \mathrm{d}\Omega\right)\right) \\ - \frac{1}{\hbar}\int_\Omega J\ \varepsilon_{pqr}\ s_q\ m_r\ v_p\ \mathrm{d}\Omega - \int_\Omega \frac{s_p}{\tau_{\mathrm{sf}}} v_p\ \mathrm{d}\Omega = 0. \end{aligned} \tag{4.42}$$

Applying *Green's theorem* ([9, pp. 35–37]) to the first four integrals leads to:

$$\begin{aligned} -2\left(-\int_\Omega \beta'\ D_0\ \Theta_{\mathrm{SH}}\ \varepsilon_{pqr}\ m_l \frac{\partial s_l}{\partial x_r}\frac{\partial v_p}{\partial x_q}\mathrm{d}\Omega + \int_{\partial\Omega} \beta'\ D_0\ \Theta_{\mathrm{SH}}\ \varepsilon_{pqr}\ m_l \frac{\partial s_l}{\partial x_r} n_q\ v_p\ \mathrm{d}\partial\Omega\right. \\ + \int_\Omega D_0 \frac{\partial s_p}{\partial x_q}\frac{\partial v_p}{\partial x_q}\mathrm{d}\Omega + \frac{\mu_{\mathrm{B}}}{e}\left(-\int_\Omega \beta\ C_0\ m_p \frac{\partial u}{\partial x_q}\frac{\partial v_p}{\partial x_q}\mathrm{d}\Omega + \int_\Omega C_0\ \Theta_{\mathrm{SH}}\ \varepsilon_{pqr} \frac{\partial u}{\partial x_r}\frac{\partial v_p}{\partial x_q}\ \mathrm{d}\Omega\right. \\ \left.\left. - \int_{\partial\Omega} C_0\ \Theta_{\mathrm{SH}}\ \varepsilon_{pqr} \frac{\partial u}{\partial x_r} n_q\ v_p\ \mathrm{d}\partial\Omega\right)\right) - \frac{1}{\hbar}\int_\Omega J\ \varepsilon_{pqr}\ s_q\ m_r\ v_p\ \mathrm{d}\Omega - \int_\Omega \frac{s_p}{\tau_{\mathrm{sf}}} v_p\ \mathrm{d}\Omega = 0. \end{aligned} \tag{4.43}$$

The two boundary conditions equation (3.6) and equation (3.7) were used to eliminate two integrals. Expressing the fields and the potential with the basis functions yields

$$\begin{aligned}\sum_i \Bigg(\sigma_l^i\, \mu_l^i \Bigg(\sum_k -2\, \beta'^k\, D_0^k\, \Theta_{\mathrm{SH}}^k\, \varepsilon_{pqr} \Bigg(-\int_\Omega \psi^{ik} \frac{\partial \psi^{ik}}{\partial x_r}\, \frac{\partial \psi^{jk}}{\partial x_q} \mathrm{d}\Omega + \int_{\partial\Omega} \psi^{ik} \frac{\partial \psi^{ik}}{\partial x_r} n_q^k\, \psi^{jk}\, \mathrm{d}\partial\Omega\Bigg)\Bigg)\\ + \upsilon^i \Bigg(\sum_k -2\, C_0^k\, \Theta_{\mathrm{SH}}^k\, \varepsilon_{pqr} \Bigg(\frac{\mu_{\mathrm{B}}}{e} \int_\Omega \frac{\partial \psi^{ik}}{\partial x_r}\, \frac{\partial \psi^{jk}}{\partial x_q}\, \mathrm{d}\Omega - \int_{\partial\Omega} \frac{\partial \psi^{ik}}{\partial x_r} n_q^k\, \psi^{jk}\, \mathrm{d}\partial\Omega\Bigg)\\ - \mu_p^i \sum_k -2 \frac{\mu_{\mathrm{B}}}{e} \beta^k\, C_0^k \int_\Omega \psi^{ik} \frac{\partial \psi^{ik}}{\partial x_q}\, \frac{\partial \psi^{jk}}{\partial x_q} \mathrm{d}\Omega\Bigg) - \sigma_q^i\, \mu_r^i \sum_k \frac{J^k}{\hbar} \varepsilon_{pqr} \int_\Omega \psi^{ik}\, \psi^{ik}\, \psi^{jk}\, \mathrm{d}\Omega\\ + \sigma_p^i \Bigg(\sum_k -2\, D_0^k \int_\Omega \frac{\partial \psi^{ik}}{\partial x_q}\, \frac{\partial \psi^{jk}}{\partial x_q} \mathrm{d}\Omega - \frac{1}{\tau_{\mathrm{sf}}^k} \int_\Omega \psi^{ik}\, \psi^{jk}\, \mathrm{d}\Omega\Bigg)\Bigg) = 0,\end{aligned} \tag{4.44}$$

or, in matrix form,

$$\sum_i M_p^{ij} \upsilon^i + \sum_i N^{ij} \sigma_p^i + \sum_i P_{pq}^{ij} \sigma_q^i = 0. \tag{4.45}$$

Equation (4.40) and (4.45) now constitute a system of matrix equations which can be solved for the coefficients of the spin accumulation and the potential. As a combination of a vector field and a scalar field, the resulting system needs to be solved for 4 n coefficients and is therefore of size 16 n^2.

4.3 Temporal integration

The time integration of a differential equation is in principle a straight forward process and there exist numerous different methods to accomplish it [101, 102, pp. 32–35]. Considerations of stability and convergence, however, coupled with the constraint that the norm of the magnetization vector has to be preserved, limit the available choices. There is also a difference if an FDM or FEM version is considered. For FDM, the classic *Runge-Kutta-Fehlberg (RKF) algorithm* [103] is generally used. The **backward differentiation formula (BDF)**, introduced by C. F. Curtiss and J. O. Hirschfelder [104], was proven to be well suited to integrate the LLG, equation (2.5), in FEM [105].

BDF is a generalization of the basic *backward Euler method* to a multistep algorithm up to sixth order, *i. e.*, it considers up to six previous time steps in computing the differential. This generalization reads

$$\sum_{j=0}^{s} \alpha^j\, m_p\left[(k-j)\Delta t\right] = \Delta t\, \beta \frac{\partial m_p\left[k\, \Delta t\right]}{\partial t}, \tag{4.46}$$

where the right side is effectively the LLG. The coefficients α and β depend upon the order s of the algorithm and can be found in tables. Writing this as

$$\sum_{j=0}^{s} \alpha^j \; m_p \left[(k-j)\Delta t\right] - \Delta t \; \beta \frac{\partial m_p \left[k \; \Delta t\right]}{\partial t} = 0, \tag{4.47}$$

it becomes clear that the problem is equivalent, as is expected for an implicit method, to finding a root. The *Newton-Raphson method* [106] can be employed here, leading to an iteration

$$m_p^{n+1} \left[k \; \Delta t\right] = m_p^n \left[k \; \Delta t\right] - \frac{\alpha^0 \; m_q^n \left[k \; \Delta t\right] + \sum_{j=1}^{s} \alpha^j \; m_q \left[(k-j)\Delta t\right] - \Delta t \; \beta \frac{\partial m_q^n [k \; \Delta t]}{\partial t}}{\alpha^0 \; \delta_{pq} - \Delta t \; \beta \; \frac{\partial m_p^n [k \; \Delta t]}{\partial t \; \partial m_q [t]}}, \tag{4.48}$$

where n denotes the iteration steps. δ_{pq} is the Kronecker delta [32, Kronecker Delta]. To avoid the inversion operation, this can be rewritten as

$$A_{pq}^n \left[k \; \Delta t\right] \; \Delta m_p^n \left[k \; \Delta t\right] = -F_q^n \left[k \; \Delta t\right], \tag{4.49}$$

where the matrix $\widehat{A}$ replaces the terms that were formerly located in the denominator of the rhs, the matrix $\widehat{F}$ contains the remainder of the rhs, and a difference term was introduced. It is evident that this is yet another matrix equation.

In principle, this is not only an iteration for a single vector component, or even a single vector, but for all vector components in the complete system, *i. e.*, three components for every vertex. Equation (4.49) therefore has additional indices, but can still be written in a vector/matrix form.

4.4 Krylov-space matrix solver

The time integration, as well as all the field components and the drift-diffusion equation, all reduce to a matrix equation in the end. Effectively, in each case, some matrix would need to be inverted. Such an inversion is a costly operation and therefore replaced by specialized solvers. Matrix solvers generally work iteratively, yielding some variant of equation (4.49). In each of those cases it is hence possible to perform the iteration via the iteration of the residual of the solution $\vec{r}$, which is here specifically shown for time integration,

$$m_p^n \left[k \; \Delta t\right] = m_p^0 \left[k \; \Delta t\right] + q \left[A_{pq}^n \left[k \; \Delta t\right]\right] \; r_q^0 \left[k \; \Delta t\right] \tag{4.50}$$

where q denotes a polynomial operator of degree $n-1$ that is constructed from $\widehat{A}$. If iterated to infinity, this process would provide the correct solution for equation (4.49); the “correct”, *i. e.* analytical, solution for the LLG can of course not be provided due to the limitations of the BDF.

There exist specialized methods, *Krylov space solvers* [107], like *e. g.* the prototypical *conjugate gradient method* [108], that can construct the polynomial operator and perform the iteration in a limited number of steps. They do so by constructing an energy norm inside the *Krylov space*, which is the vector space constructed from all the polynomials. While the iteration of the residual leads to a complicated path inside this space, minimization of this energy norm is heading straight (that is to be taken literally) for the solution.

However, even finite time might still be too long, as the convergence speed of these methods can be rather low. Equation (4.49) can be transformed into

$$A^n_{pq}\left[k\ \Delta t\right]\ P^{-1}_{qr}\left[k\ \Delta t\right]\ P_{rl}\left[k\ \Delta t\right]\ \Delta m^n_l\left[k\ \Delta t\right] = -F^n_p\left[k\ \Delta t\right], \tag{4.51}$$

with equation (4.50) becoming

$$m^n_q\left[k\ \Delta t\right] = m^0_q\left[k\ \Delta t\right] + q\left[A^n_{pq}\left[k\ \Delta t\right]\ P^{-1}_{qr}\left[k\ \Delta t\right]\right]\ r^0_q\left[k\ \Delta t\right]. \tag{4.52}$$

$\widehat{P}$ is a preconditioning matrix, selected in such a way as to $\widehat{A}\ \widehat{P}^{-1} = \widehat{1}$. This greatly improves convergence speed, at the price of additional matrix inversions [105]. $\widehat{P}$ is essentially the Jacobian matrix of the LLG, or a close approximation of it, such that $\widehat{A}\ \widehat{P}^{-1}$ is close to unity, but also enabling cheap inversion of the operator.

Part II

Micromagnetically integrated numerical model of spin pumping based on spin diffusion

An abridged version of the research presented here has been published in *Physical Review B* [109] in July of 2022.

5.1 Introduction

The interaction between localized and mobile spins in magnetic materials has been introduced in chapter 3. This includes spin torque, the action of spin accumulation on the precession of magnetization. But the inverse effect also exists (by virtue of Onsager's reciprocity relation [110]): the precession of magnetization has an effect on spin accumulation, in that it can be the origin of it. This is generally known as **spin pumping**. More specifically, the term means the outflow of spins from a magnetic material into a non-magnetic material [111]. This effect has been proven in numerous experiments, *e.g.* [111, 48, 112]. As an extension of an earlier work ([82]), this was modeled by Zhang and Li [113] on a spin drift-diffusion foundation.

As the drift-diffusion model can only be analytically (or with low computational effort) solved for very simple cases, approximations for common applications are generally used. This includes J. C. Slonczewski [114] and Zhang and Li (introduced also in [113]) for spin drift-diffusion without spin pumping. Analytical treatments of spin pumping are generally calculated using the formalism of Buettiker *et al.* [115] (see, e.g. Omelchenko *et al.* [116]), which describes a surface-constant spin current. Such a formulation can in principle be used in micromagnetic computations, but only for homogeneous precession; for magnonic applications, the full drift-diffusion model needs to be employed. This has not been done prior to this work. Although the drift-diffusion model is also employed by other groups (*cf.* [117, 118]), these implementations of the model do not incorporate spin pumping. Note that the package presented in [118] is able to simulate spin pumping, but only by a pre-built current term (similarly to [116]).

Such a **fully micromagnetical implementation** is of prime interest, since this can use all the already implemented magnetization dynamics, and is therefore well suited to support magnonic simulations (and experiments); including the work in this thesis. Based upon [113], such an implementation was developed.

5.2 Derivation

This repeats the derivation of [113], with modifications where needed. Magnetism emerges from the spin property of a quantum-mechanical object. In a first order approximation, the spins in a material can be decomposed into those supplied by quasi-static objects, *i.e.* cations localized on their lattice sites, and those from mobile objects, *i.e.* conduction electrons. The spins, or, in a continuous sense, the magnetization of those conduction electrons, can then be treated as a transport quantity. This makes it possible to start with a Boltzmann-type transport equation for the magnetization carried by conduction electrons $\overrightarrow{M^{\mathrm{e}}}$,

$$\frac{\partial M_p^{\mathrm{e}}\left[\{x_w\},t\right]}{\partial t} = -\frac{\partial j_{qp}^{\mathrm{s}}\left[\{x_w\},t\right]}{\partial x_q} - \frac{J}{\hbar}\varepsilon_{pqr}\, M_q^{\mathrm{e}}\left[\{x_w\},t\right]\, m_r\left[\{x_w\},t\right] - \frac{s_p\left[\{x_w\},t\right]}{\tau_{\mathrm{sf}}}. \quad (5.1)$$

This is the generalized form of equation (3.2). To link the magnetization of the conduction electrons and the spin accumulation together, the former can be decomposed into a component parallel to $\vec{m}$ and an additional one, such that

$$M_p^{\mathrm{e}}\left[\{x_w\},t\right] = \chi_{\mathrm{e}}\, M_{\mathrm{S}}\, m_p\left[\{x_w\},t\right] + s_p\left[\{x_w\},t\right]. \tag{5.2}$$

These two components represent a permanently existing one (where it is assumed that the conduction-electrons' spins align in the cation's field at equilibrium), and the spin accumulation as an additional one (the deviation from that equilibrium). This does not mean that the two components are necessarily orthogonal to each other; for multi-magnetic-layer systems (like in [116]) they are not. For the systems which will be used to test the implementation, with single magnetic layers, they are. Therefore $\vec{m}\cdot\vec{s}=0$, which can be shown for the analytical results in the next section. The prefactor was introduced by S. Takahashi [119]. It offers the advantage that it can be easily calculated using material parameters that are already in use in the drift-diffusion framework. He defines the **susceptibility of the conduction electrons** χ_{e} as:

$$\chi_{\mathrm{e}} = \mu_0\, \mu_{\mathrm{B}}^2\, n\left[\mathcal{E}_{\mathrm{F}}\right] \frac{J}{\hbar\, \mu_0\, \gamma_{\mathrm{e}}\, M_{\mathrm{S}}} = \frac{\mu_{\mathrm{B}}\, C_0\, J}{e^2\, M_{\mathrm{S}}\, D_0}, \tag{5.3}$$

where $C_0 = n\left[\mathcal{E}_{\mathrm{F}}\right] e^2 D_0/2$ is used, a variant of Sommerfeld's conductivity formula [120]. This susceptibility is a product of the paramagnetic susceptibility of the conduction electrons and a dimensionless interaction constant (*cf.* equation (3.10)). $n\left[\mathcal{E}_{\mathrm{F}}\right]$ is the density of states for conduction electrons at the Fermi level.

Inserting equation (5.2) in equation (5.1), the adiabatic approximation $\partial\vec{s}/\partial t = 0$ (due to the relaxation-time scale of $\vec{s}$ being much smaller than of $\vec{m}$) can be applied, which yields ([113]):

$$\chi_{\mathrm{e}}\, M_{\mathrm{S}} \frac{\partial m_p\left[\{x_w\},t\right]}{\partial t} = -\frac{\partial j_{qp}^{\mathrm{s}}\left[\{x_w\},t\right]}{\partial x_q} - \frac{J}{\hbar}\varepsilon_{pqr}\, s_q^{\mathrm{e}}\left[\{x_w\},t\right]\; m_r\left[\{x_w\},t\right] - \frac{s_p\left[\{x_w\},t\right]}{\tau_{\mathrm{sf}}}. \tag{5.4}$$

For spin drift-diffusion computations in spintronics (*cf.* equation (3.2)), the left side is generally ignored, as spin accumulation is forced into the system via charge current boundary conditions. These currents are generally much stronger than the spin-pumping effects.

This is the **standard form of spin pumping** and is generally used for analytic treatment. If the left side of equation (5.4) is non-zero, *i.e.* magnetization is precessing, a spin current is generated, or pumped. For numerical applications, it is important to understand that the left side (*i.e.* the driving term for spin pumping) is a function of $\vec{s}$ itself, since

$$\begin{aligned}
\frac{\partial m_p\left[\{x_w\},t\right]}{\partial t} &= -\frac{\mu_0\,\gamma_{\mathrm{e}}}{1+\alpha^2}\varepsilon_{pqr}\, m_q\left[\{x_w\},t\right]\Bigg(H_r^{\mathrm{eff}}\left[\{x_w\},t\right] + \frac{J}{\hbar\,\mu_0\,\gamma_{\mathrm{e}}\,M_{\mathrm{S}}} s_r\left[\{x_w\},t\right] \\
&\quad + \alpha\,\varepsilon_{rln}\, m_l\left[\{x_w\},t\right]\left(H_n^{\mathrm{eff}}\left[\{x_w\},t\right] + \frac{J}{\hbar\,\mu_0\,\gamma_{\mathrm{e}}\,M_{\mathrm{S}}} s_n\left[\{x_w\},t\right]\right)\Bigg) = \\
&T_p\left[\left\{H_w^{\mathrm{eff}}\left[\{x_w\},t\right]\right\}\right] - \frac{J}{\hbar\, M_{\mathrm{S}}\left(1+\alpha^2\right)}\varepsilon_{pqr}\, m_q\left[\{x_w\},t\right]\left(s_r\left[\{x_w\},t\right]\right. \\
&\quad \left. + \alpha\,\varepsilon_{rln}\, m_l\left[\{x_w\},t\right]\; s_n\left[\{x_w\},t\right]\right).
\end{aligned} \tag{5.5}$$

This is the explicit form of the LLG equation (2.5), where the spin torque generated by spin pumping has been split off from the remaining fields ($\overrightarrow{H_{\mathrm{eff}}} = \overrightarrow{H_{\mathrm{Zee}}} + \overrightarrow{H_{\mathrm{ex}}} + \overrightarrow{H_{\mathrm{demag}}} + \overrightarrow{H_{\mathrm{uni}}} + \overrightarrow{H_{\mathrm{cub}}} + \ldots$), that are then combined in the torque operator $\overrightarrow{T}\left[\overrightarrow{H_{\mathrm{eff}}}\right]$. The spin accumulation generated by spin pumping exerts an influence on the causative precession. In analytic treatises this resolves itself in the end, but for explicit numerical computation, this influence needs to be considered directly in equation (5.4). Inserting equation (5.5) and collecting the spin-accumulation terms leads to

$$\begin{aligned}\chi_{\mathrm{e}}\, M_{\mathrm{S}}\, T_p\left[\left\{H_w^{\mathrm{eff}}\left[\{x_w\},t\right]\right\}\right] = &-\frac{\partial j_{qp}^{\mathrm{s}}\left[\{x_w\},t\right]}{\partial x_q} - \frac{J}{\hbar}\left(1+\frac{\chi_{\mathrm{e}}}{1+\alpha^2}\right)\varepsilon_{pqr}\, s_q\left[\{x_w\},t\right]\; m_r\left[\{x_w\},t\right] \\ &-\left(\frac{1}{\tau_{\mathrm{sf}}}+\frac{\chi_{\mathrm{e}}\, J\,\alpha}{\hbar\left(1+\alpha^2\right)}\right) s_p\left[\{x_w\},t\right] \\ &+\frac{\chi_{\mathrm{e}}\, J\,\alpha}{\hbar\left(1+\alpha^2\right)} m_q\left[\{x_w\},t\right]\; s_q\left[\{x_w\},t\right]\; m_p\left[\{x_w\},t\right].\end{aligned} \tag{5.6}$$

This form now enables **self-consistent** numerical computation of the spin accumulation as it incorporates the effects of spin torque on the precessional motion of magnetization. To solve equation (5.6), the $\overrightarrow{T}\left[\overrightarrow{H_{\mathrm{eff}}}\right]$ operator needs to be computed. The current terms and boundary conditions are the same as introduced in section 3.2.

It is important to note that the spin drift-diffusion equation can only be applied in conductive material, or else no spin current can exist. For spin pumping, this is exacerbated by the fact that the driving term is always zero as there are no conduction electrons. Application of this model to spin pumping from non-conductive material needs a special treatment in the simulation; this will be shown in the following section.

5.3 Numerical computation

The standard method hitherto employed to solve the drift-diffusion system was the *Generalized Minimal Residual (GMRES)* algorithm [121] with an *Algebraic Multigrid*

Table 5.1: Numerical computation settings for drift-diffusion/pumping.

Parameter	Old	New
Linear system solver	GMRES	DGMRES
GMRES restarts	100	300
Orthogonalization	Classical	Modified
Linear system relative tolerance	1×10^{-8}	1×10^{-8}
Preconditioner type	BoomerAMG	fieldsplit
Fieldsplit type		Schur complement
Saddle point detection		True
Left Schur inversion		Preconditioner only
Factorization shift		Nonzero

(BoomerAMG) preconditioner [122]. Trying to solve the pumping system with that method generally fails in the preconditioner step, due to saddle points encountered. Research in the relevant online discussion boards helped coming up with a new numerical method.

The new method uses the *Deflated Generalized Minimal Residual (DGMRES)* algorithm [123] with a *fieldsplit* type preconditioner [124, PCFIELDSPLIT] using the *Schur complement* [125]. Automated saddle point detection and value shift was used. Some other parameters have been optimized to help with convergence. The developed method has become standard for the general drift-diffusion computation as well.

On occasion, the spin-pumping computation still fails. As the underlying numerics tend to be very opaque, it is difficult to remedy this.

Table 5.1 shows a comparison of the old and new computation parameters.

5.4 Verification

To validate the implementation with analytical solutions from literature, numerical computation is performed on a defined state. Spin accumulation is extracted directly as a computation result, while the modification of the dynamical behavior is determined by projecting the total torque vector onto the cross product basis of the LLG and suitable renormalization. Those values are compared against those obtained from analytical formulas in the same state. *N.b.* that the provided analytical terms for the spin accumulation are achieved by solving equation (5.6) and thus do not concur with those found by the other authors (as they solve equation (5.4)). This originates from the fact that the implementation explicitly computes the spin accumulation. The core point is here that the analytical treatments that are referenced and the numerical computations presented here take a different path to their goal, but should agree in the end result, namely the enhanced Gilbert damping and decreased rate of precession.

5.4.1 Bulk system

The first validator considered is the bulk system calculated by Zhang and Li [113]. The authors suppose that the system is diffusion-less, *i.e.* $\vec{\nabla} \otimes \vec{m} \propto \hat{j}_\mathrm{s} = \emptyset$ (where $\otimes$ denotes the outer product), which is true for single-material bulk systems with homogeneous magnetization. Under that constraint, equation (5.6) can be solved to yield

$$s_p = -\frac{\Gamma_\mathrm{BS}\,\chi_\mathrm{e}\,M_\mathrm{S}}{1+\Gamma_\mathrm{BS}^2}\,\frac{\hbar\,(1+\alpha^2)}{J\,(1+\alpha^2+\chi_\mathrm{e})}\left(T_p\left[\left\{H_w^\mathrm{eff}\,[t]\right\}\right]+\Gamma_\mathrm{BS}\,\varepsilon_{pqr}\,m_q\,T_r\left[\left\{H_w^\mathrm{eff}\,[t]\right\}\right]\right). \quad (5.7)$$

This uses the definition

$$\Gamma_\mathrm{BS} = \frac{\tau_\mathrm{sf}\,J\,(1+\alpha^2+\chi_\mathrm{e})}{\hbar\,(1+\alpha^2)+\tau_\mathrm{sf}\,\alpha\,\chi_\mathrm{e}\,J}. \quad (5.8)$$

Solving equation (5.4) under the same constraint, and inserting the solution into equation (5.5), the form of the original LLG can be recreated by introducing modified γ_e and α parameters,

$$\gamma_\mathrm{SP} = \gamma_\mathrm{e} \frac{1+\Gamma_\mathrm{B}^2}{1+\Gamma_\mathrm{B}^2\left(1+\chi_\mathrm{e}\right)} \quad \text{and} \tag{5.9a}$$

$$\alpha_\mathrm{SP} = \frac{\alpha\left(1+\Gamma_\mathrm{B}^2\right)+\Gamma_\mathrm{B}\,\chi_\mathrm{e}}{1+\Gamma_\mathrm{B}^2\left(1+\chi_\mathrm{e}\right)}, \tag{5.9b}$$

where $\Gamma_\mathrm{B} = \tau_\mathrm{sf} J/\hbar$. This is a rewritten form of the result of [113]. These modifications to the Gilbert damping and to the rate of precession lead to an increase of the former and to a decrease of the latter. The damping from spin pumping is an important mechanism of damping in magnetic materials, especially for multi-layer systems (as will be seen in the next subsection).

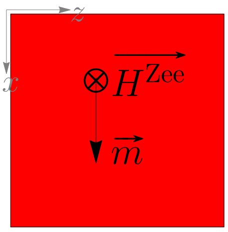

Figure 5.1: Bulk system, $(10 \times 10 \times 10)$ nm

To test the implementation against this result, a cube with homogeneous magnetization, as shown in figure 5.1, is set up. Such a setup, and having no internal interactions (*i.e.* $H_p^\mathrm{eff} = H_p^\mathrm{Zee}$), makes the system diffusion-less — it behaves as if it only consists of a single spin. The material parameters were chosen to simulate permalloy and are listed in table 5.2. The only exception is the exchange coupling strength J, or, via the relation $\lambda_\mathrm{c} = \sqrt{2D_0\hbar/J}$, the coupling length λ_c. Variations in the coupling length, although not achievable in experiments, provide a representative way to test the implementation. For the analytical calculation of equation (5.7), the torque is defined as

$$T_p\left[\left\{H_w^\mathrm{eff}[t]\right\}\right] = -\frac{\mu_0\,\gamma_\mathrm{e}\sqrt{H_q^\mathrm{Zee}\,H_q^\mathrm{Zee}}}{1+\alpha^2}\left((0,0,1)^\intercal - \alpha\,(0,1,0)^\intercal\right). \tag{5.10}$$

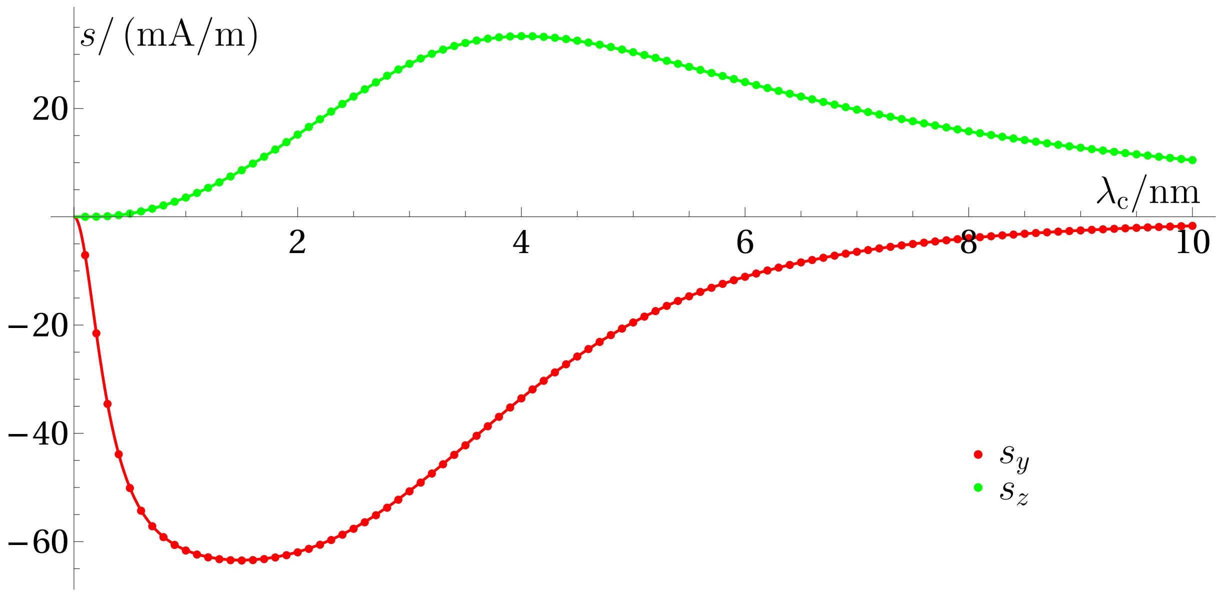

Figure 5.2: y and z components of $\vec{s}$, as function of λ_c for the bulk system. Data points are computed values, the solid line the analytical prediction; $\alpha = 0$.

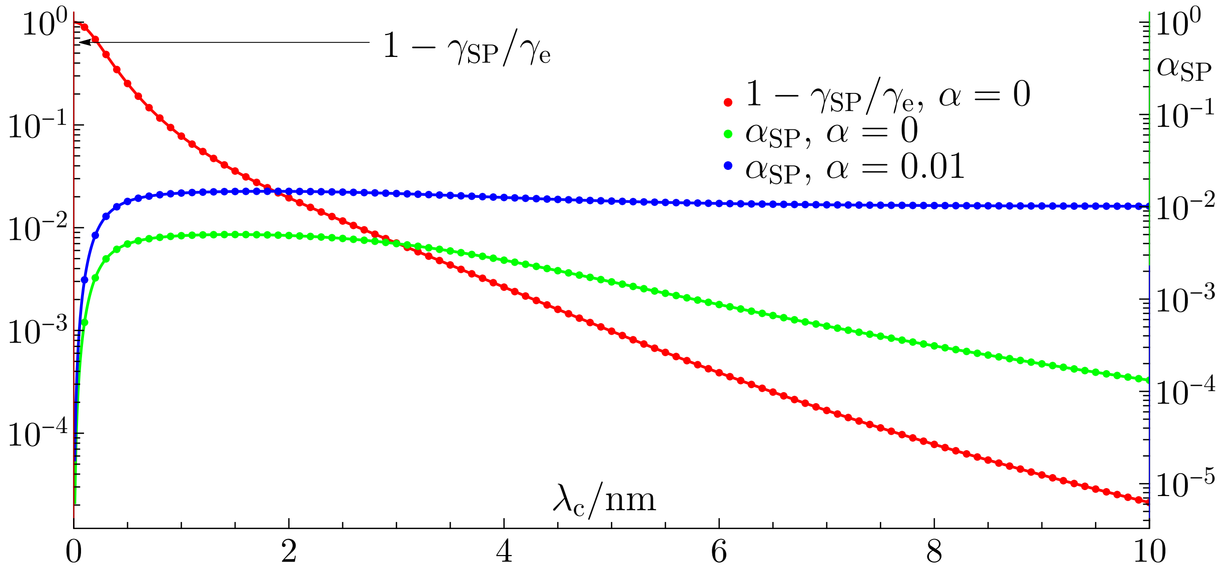

Figure 5.3: γ_{SP}/γ_e (left axis) and α_{SP} (right axis), as logarithmic function of λ_c for the bulk system. To facilitate logarithmic plotting for γ_{SP}, values have been recomputed. Data points are computed values, solid lines the analytical prediction.

Figure 5.2 shows the y and z components of the average computed spin accumulation compared to the values from equation (5.7). It can be seen that results are in good agreement with each other. The x component (not depicted) should equal zero, but numerical computation yields a finite value in the aA/m range due to numerical errors.

Table 5.2: Bulk system

Quantity	Value
M_S	900 kA/m
C_0	1 MS/m
D_0	10 cm^2/s
λ_{sf}	4 nm
$\lVert\overrightarrow{H_{Zee}}\rVert$	7.96 kA/m

Figure 5.3 shows the modified gyromagnetic ratio γ_{SP} and damping parameter α_{SP}, compared to the values from equation (5.9a) and 5.9b. Once again, the results are in good agreement with each other. The damping generated by spin pumping is about half the intrinsic damping at maximum. For realistic values of the coupling length for such a system, $\lambda_c \approx 3$ nm, it is still ≈ 40 %. The damping from spin pumping therefore constitutes an important part of the total damping in bulk systems.

5.4.2 Layer system

The second system considered is the interface system calculated by *Takahashi* [119, pp. 1462–1465]. His analytical formulation has been specifically introduced to extend the drift-diffusion's applicability to non-conductive material. Such a system, consisting of a non-conductive magnetic material and a non-magnetic conductor, is a good representation of the yttrium iron garnet (YIG, $Y_3Fe_5O_{12}$)/platinum-systems often employed in magnonics. This subsection is called *layer* because the interaction is modeled as an actual layer in the numerical computation. The localized interaction effectively decouples the $\vec{s}$-$\vec{m}$-term in equation (5.6) and enables solution of the diffusion equation in the case of homogeneous magnetization, using equation (3.3) as a homogeneous equation with boundary term as

$$s_p[z] = -\frac{\Gamma_{\text{IS}}\,\chi_{\text{e}}\,M_{\text{S}}}{1+\Gamma_{\text{IS}}^2}\,\frac{\hbar\,(1+\alpha^2)}{J\,(1+\alpha^2+\chi_{\text{e}})}\cosh\left[\frac{L-z}{\lambda_{\text{sf}}}\right]\operatorname{sech}\left[\frac{L}{\lambda_{\text{sf}}}\right] \times \left(T_p\left[\left\{H_w^{\text{eff}}[z=0,t]\right\}\right] + \Gamma_{\text{IS}}\,\varepsilon_{pqr}\,m_q\,T_r\left[\left\{H_w^{\text{eff}}[z=0,t]\right\}\right]\right). \tag{5.11}$$

Here, L is the length of the conductor and $\lambda_{\text{sf}} = \sqrt{2D_0\tau_{\text{sf}}}$ is the spin-flip length. This uses the definition

$$\Gamma_{\text{IS}} = \frac{a}{\lambda_{\text{sf}}}\coth\left[\frac{L+a}{\lambda_{\text{sf}}}\right]\Gamma_{\text{BS}}, \tag{5.12}$$

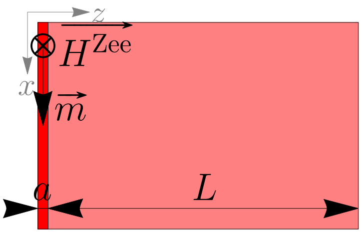

Figure 5.4: Layer system with (10×10) nm cross-section in the xy-plane. The red part with thickness $a = 0.5$ nm is magnetic and conducting, the pink one only conducting.

where a is the effective pumping length. This is to account for the fact that the $\vec{s}$-$\vec{m}$-coupling is not an interface effect and has to be given some coupling length. The saturation magnetization is, after all, a volume average, and needs to be transformed into an effective surface magnetization to be used as a boundary term. In the same way, the spin torque term in the LLG also gains a modulation length. Since it can be naively expected (and is confirmed by the computations, at least within numerical reason) that this effective torque length d is equal to a, the contributions cancel out and equation (5.9a) and 5.9b remain unchanged, except for

$$\Gamma_{\text{B}} \to \frac{a}{\lambda_{\text{sf}}}\coth\left[\frac{L+a}{\lambda_{\text{sf}}}\right]\Gamma_{\text{B}}, \tag{5.13}$$

the same modulation as above. The additional hyperbolic cotangent, modulating Γ (or a), results from the finite-sized system and the fact that the drop-off of spin accumulation is

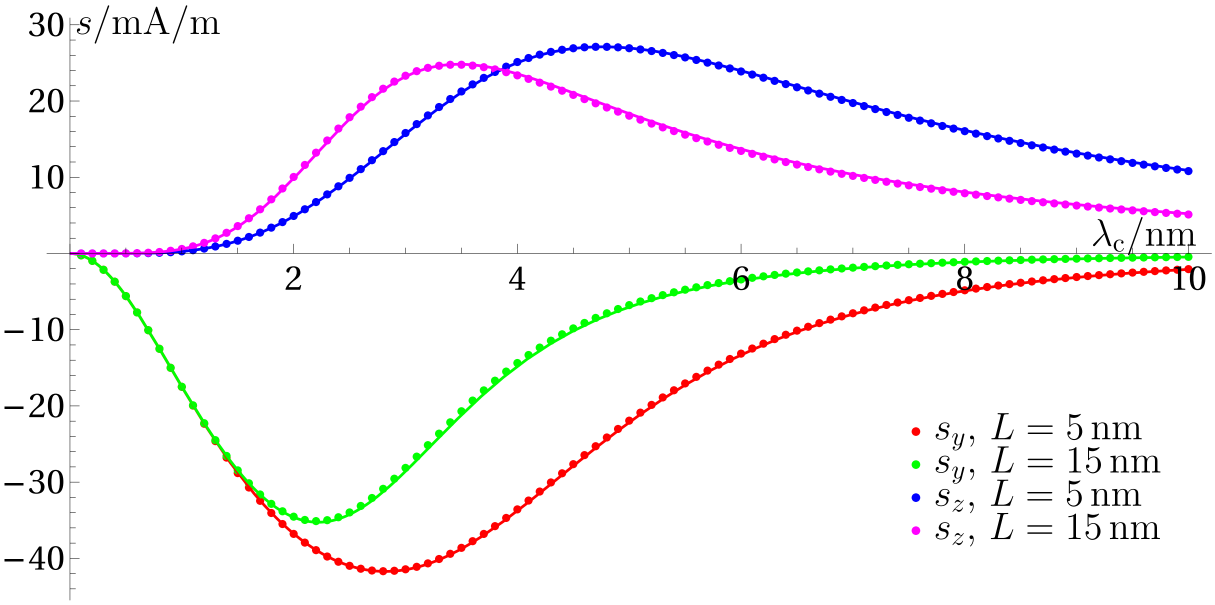

Figure 5.5: y and z-components of $\vec{s}$, as function of λ_{c} for the layer system, both long and short spin sinks. Data points are computed values, the solid lines the analytical prediction; $\alpha = 0$.

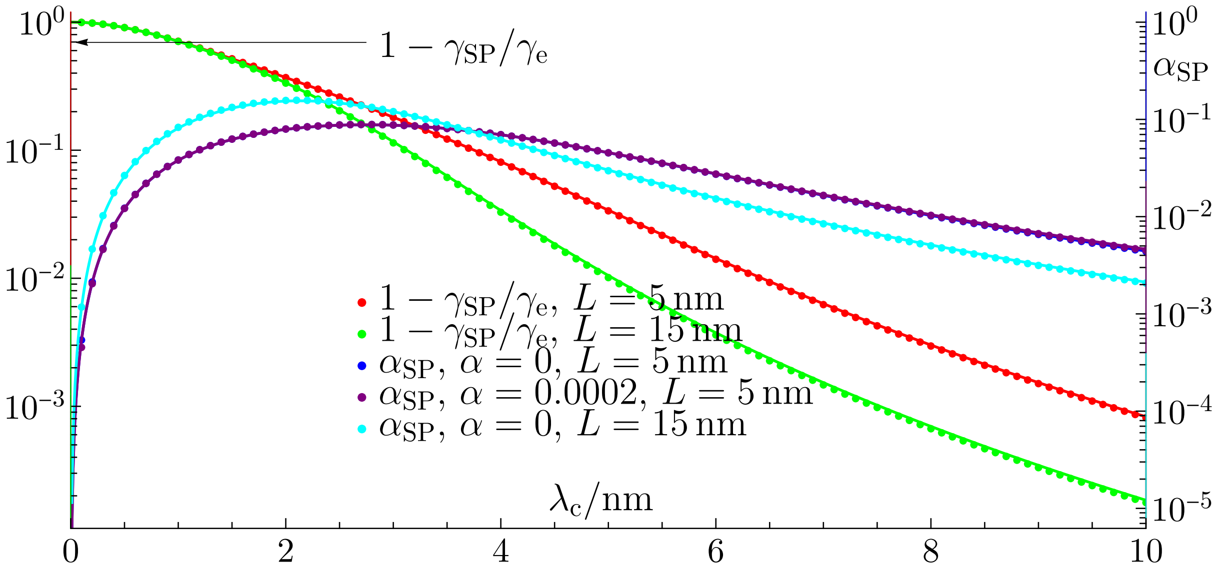

Figure 5.6: γ_{SP}/γ_e (left axis) and α_{SP} (right axis), as logarithmic function of λ_c for the layer system, both long and short spin sinks. To facilitate logarithmic plotting for γ_{SP}, values have been recomputed. Data points are computed values, solid lines the analytical prediction.

slower than for an open system. Hence more spin accumulation exists in the interaction layer, and it behaves similar to an increased interaction length.

To test against this result, a bar as shown in figure 5.4, with homogeneous magnetization in the magnetic region with thickness 0.5 nm, is set up. As the tetrahedral resolution is also 0.5 nm, this results in a single layer of tetrahedra carrying magnetization; hence $a = d = 0.5\,\mathrm{nm}$ is expected. The utilization of a distinctive interaction layer originates from the necessities of FEM (*cf.* section 4.1). As a differential equation is solved not on points in space (as with FDM), interactions on surfaces (other than full boundary conditions) are not possible. Moreover, since material parameters are defined as discontinuous functions (to model material interfaces), equation (5.3) is not even defined at the interface. And since the physical interaction is not really a surface interaction anyway, the layer method is more "correct" than any approximate surface terms.

Table 5.3: Layer system

Quantity	Magnetic	Conducting
M_S	140 kA/m	None
C_0	4.5 MS/m	
D_0	50 cm²/s	
λ_{sf}	14 nm	
$\left\|\overrightarrow{H_{Zee}}\right\|$	7.96 kA/m	None

Again, all internal interactions are ignored. The material parameters are chosen to simulate a YIG/Pt-system and are listed in table 5.3. It is important to understand here that the red part is simulated to be both magnetic and fully conducting — it is an interaction layer that is both YIG and Pt, at least simulation-wise. $\vec{T}\left[\overrightarrow{H_{\text{eff}}}\right]$ is identical to the preceding subsection. Figure 5.5 shows the y and z components of the average computed spin accumulation in the magnetic region, compared to the values from equation (5.11). Results again agree, but not as good as for the bulk system. This is to be expected: whereas the bulk system eliminates all non-localities by eliminating diffusion, here the computation has to be done on a mesh, introducing discretization errors.

Figure 5.6 shows the average modified gyromagnetic ratio γ_{SP} and damping parameter α_{SP} in the magnetic region, compared to the values from equation (5.9a) and 5.9b. Once again, the results are in good agreement with each other. The additional damping generated by the spin torque is very noticeable: the base value of $\alpha = 2 \times 10^{-4}$ is increased by two orders of magnitude in the interaction layer. The difference in L now also leads to different damping curves.

The dependence of the achieved damping upon the spin sink length is also evident from figure 5.6. This has also been shown in prior experiments [116].

5.5 Magnonic damping

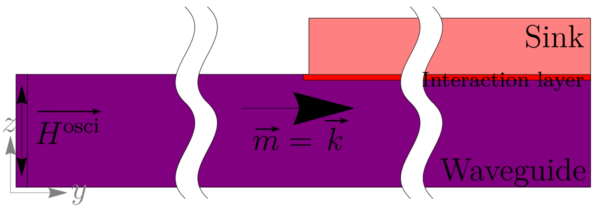

Figure 5.7: The magnonic damping system. The magnetic waveguide with $(10 \times 1251 \times 10)$ nm is in purple; the magnetic and conducting interaction layer with thickness 0.5 nm is in red, and the conducting spin sink with thickness 5 nm is in pink.

To test the implementation against a dynamic (and somewhat real-world) case, the propagation of a magnon is simulated. The increased Gilbert damping due to the spin torque from spin pumping should quickly suppress the magnon.

To this end, the layer system gets extended to the fully fledged waveguide seen in figure 5.7. The length of the waveguide is 1251 nm, of which the first 1 nm is subject to a linearly polarized external field $\vec{H}_{\text{osci}}$, oscillating in z direction and driving the magnon (with both the initial magnetization and the wavevector $\vec{k}$ of the magnon in y direction). After 251 nm, a spin-sink layer is placed atop the waveguide, with a corresponding interaction layer beneath it. The material parameters are shown in table 5.4. *N.b.* that $\alpha = 0$, hence all damping observed originates from spin pumping.

Table 5.4: Magnonic damping system

Quantity	Waveguide	Interaction	Sink
M_S	140 kA/m	140 kA/m	None
A	200 fJ/m	200 fJ/m	None
C_0	None	10 MS/m	10 MS/m
D_0	None	50 cm^2/s	50 cm^2/s
λ_{sf}	None	2 nm	2 nm
λ_{c}	None	2 nm	None
K	10 kJ/m^3	10 kJ/m^3	None
$\lVert\vec{H}_{\text{osci}}\rVert$	first 1 nm: 79.6 kA/m		None
f	first 1 nm: 30 GHz		None

The setup of a non-conducting magnetic material was chosen to limit the computation of spin pumping to a smaller part of the system. Furthermore, the material parameters were modified to achieve a small-wavelength exchange-magnon and high damping. In addition, demagnetization-field contributions were not computed, both for performance and implementation reasons. Instead, the restoring force on the magnetization is simulated by an uniaxial-anisotropy field along the y axis. The system parameters are specifically chosen to demonstrate the implementation's capabilities and not to mimic an actual experimental setup.

Figure 5.8 shows the transversal component of the magnetization along the waveguide centerline after 2.4 ns. The magnon has penetrated the whole waveguide, with the spin-torque-enhanced damping successfully suppressing the magnon along its path. Fitting a simple exponential function to the magnetization for $y > 250$ nm (where the waveguide is

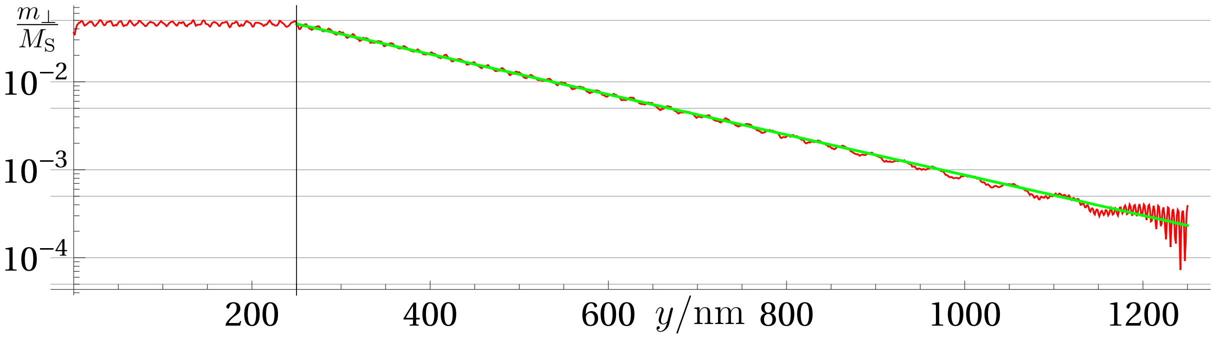

Figure 5.8: Transversal component $m_\perp$ of $\vec{m}$ (= wave amplitude) at $x = z = 5\,\text{nm}$ (the waveguide center), as logarithmic function of coordinate for the magnonic damping system after 2.4 ns. Red are computed values, green is a fitted exponential decay with the magnon free path $l = 190\,\text{nm}$. The black vertical marks the beginning of the spin sink layer.

covered by the spin sink), a free path of $l = 190\,\text{nm}$ can be obtained. It is clearly visible that considerable damping exists, even with $\alpha = 0$.

Figure 5.9 shows the modified gyromagnetic ratio γ_{SP} and damping parameter α_{SP} along a line at $z = 9.5\,\text{nm}$, compared to the values from equation (5.9a) and 5.9b. Although the propagating magnon exhibits non-homogeneous, wavelike precession (in space), the modified parameters do not reflect that behavior and behave as if the precession is indeed homogeneous. Also, the deviation from "normal" values ($\gamma_{\text{SP}} = \gamma$ and $\alpha_{\text{SP}} = 0$) is less pronounced than expected. Both effects can be attributed to the cross-diffusion of spin accumulation in the interaction layer: The analytical solution for homogeneous magnetization assumes the effect of only the locally produced spin accumulation on the precessional motion. For a magnon, spin accumulation produced at some point can diffuse to other points in the vicinity, effecting the precession there as well. In return, the effect on the precession at the point were it was produced is reduced. This cross-diffusion then equilibrates the spin accumulation, generally reducing it, and therefore its effects. This behavior generally depends upon the relation between the magnon wavelength and λ_{sf}.

The rapid oscillations at the end of the waveguide ($y > 1100\,\text{nm}$) most likely originate from numerical errors. The magnetization is almost coaligned with the longitudinal axis, which is a regime where the integration errors from numerically solving equation (5.5) are easily of the same magnitude as the precession angle. There is some additional structure

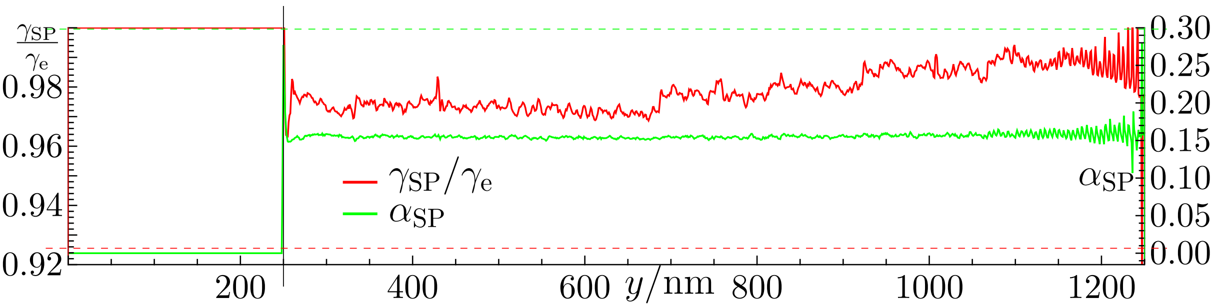

Figure 5.9: $\gamma_{\text{SP}}/\gamma_e$ (left axis) and α_{SP} (right axis) at $x = 5\,\text{nm}$, $z = 9.5\,\text{nm}$ (the interface of the waveguide and the interaction layer), as function of coordinate for the magnonic damping system after 2.4 ns. The black vertical marks the beginning of the spin sink layer; the dashed lines mark the corresponding expected analytical values from eqs. (5.9a) and (5.9b).

for γ_{SP}, including noticeable steps (around 700 nm and 900 nm). The nature of those is currently not known.

Part III

Basics of magnonics

The concept of *magnonics* can be approached, at least if considered analytically, from two directions. In a classical, continuous way, based upon the basics described in chapter 2, or in a quantized formulation. Computationally it is (at least in this work) always classical, and that is a valid approximation for the application cases presented.

The quantized approach serves three purposes:

1. It provides a justification for why the term *magnon*, *i. e.* treating magnetic waves as particles, is possible.
2. It shows where the continuous treatment is no longer valid.
3. It makes the linear nature of the analytical process visible. There is a plethora of phenomena when going beyond a linear quantized formulation. Two important ones will be analyzed.

Chapter 6: Ferromagnetic resonance

The concept of resonance is a very fundamental one in physics. See R. Feynman [126, Vol 1, chapter 23] for the general idea and meanings. The following derivations not only provide the necessary parameters for resonance in a ferromagnetic context, thus generally designated **ferromagnetic resonance (FMR)**, but also provide analytical cases for magnetization dynamics and thus give insight into the often very complex behavior of a simulation.

N. b. that the derivation is performed in real numbers ($\mathbb{R}$). Physics describes real processes, after all; using phasor notation just out of mathematical convenience is something that should be avoided. This is not only a principal argument, but the terms and conditions that will be derived here, differ from the established ones. They include additional physical meaning, that gets lost in complex notation. The standard derivation can be found, *e. g.*, in [77].

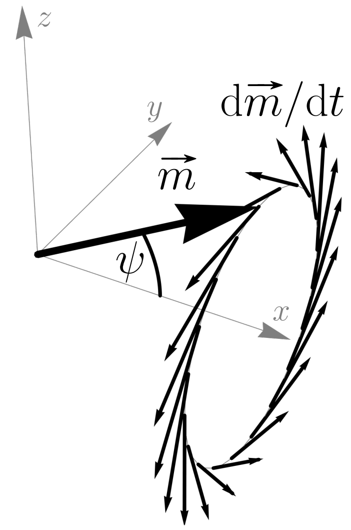

Figure 6.1: Precessional motion shown for simple FMR considerations.

The motion described in subsection 2.1.1 can be treated as 2-dimensional oscillation. With the addition of phenomenological damping in subsection 2.1.2, all of the requirements for resonance are in place. The starting point is the implicit LLG equation, equation (2.4), restricted to the case of homogeneous precession,

$$\frac{\partial m_p\left[t\right]}{\partial t} = -\mu_0\ \gamma_{\mathrm{e}}\ \varepsilon_{pqr}\ m_q\left[t\right]\ H_r^{\mathrm{eff}}\left[t\right] + \alpha\ \varepsilon_{pqr}\ m_q\left[t\right] \frac{\partial m_r\left[t\right]}{\partial t}. \tag{6.1}$$

The aim is to find an analytical solution for a specific field configuration. The solution to equation (2.1) is clearly a simple circular precession around some preferred direction, such that the ansatz

$$m_p\left[t\right] = \delta_{p1}\cos\left[\psi\right] + \left(\delta_{p2}\cos\left[\omega_{\mathrm{m}}\ t\right] + \delta_{p3}\sin\left[\omega_{\mathrm{m}}\ t\right]\right)\sin\left[\psi\right] \tag{6.2}$$

can be formulated, where ω_{m} is the **angular precession speed** of the magnetization. This is shown in figure 6.1. Assuming only small opening angles of precession ψ, a **linear approximation** is possible, such that . The time derivative of the magnetization is

$$\frac{\partial m_p\left[t\right]}{\partial t} = \omega_{\mathrm{m}}\ \varepsilon_{p1q}\ m_q\left[t\right]. \tag{6.3}$$

If the explicit LLG equation (2.5) was to be used, the damping term usually contains product terms like $m_2\ m_3$, necessitating linearization. By enforcing this derivative in equation (6.1) instead, the resulting equation is automatically linearized in presence of damping, hence providing the reason for selection.

$\overrightarrow{H^{\text{eff}}}[t]$ in equation (6.1) is decomposed to

$$H_p^{\text{eff}}[t] = H_p[t] + \Delta h_p[t], \tag{6.4}$$

where $\overrightarrow{\Delta h}[t]$ is a small field, such that the linearization is valid, responsible for the orthogonal deviation from the equilibrium field $\overrightarrow{H}[t]$. $\overrightarrow{\Delta h}[t]$ follows the same functional form as equation (6.2), only with ω_{h} as angular precession speed, some amplitude A, and $\psi = \pi/2$.

Using equation (6.3) and 6.4, equation (6.1) can be brought to the form

$$m_p[t] = \chi_{pq}[\omega_{\text{m}}]\ \Delta h_q[t], \tag{6.5}$$

with the **dynamic susceptibility tensor** $\widehat{\chi}$ (also known as the *Polder susceptibility tensor*, after D. Polder [127]). Even though the tensor is three-dimensional, only a 2x2-part is non-zero, per construction. The reason and meaning of the term *dynamic* can be understood in the following. The functional form of field and magnetization does only depend on ω_{m}, ω_{h}, ψ, and A. Hence, in a different coordinate representation,

$$\widehat{\chi} = \begin{pmatrix} \frac{\mathrm{d}\omega_{\text{m}}}{\mathrm{d}\omega_{\text{h}}} & \frac{\mathrm{d}\omega_{\text{m}}}{\mathrm{d}A} \\ \frac{\mathrm{d}\psi}{\mathrm{d}\omega_{\text{h}}} & \frac{\mathrm{d}\psi}{\mathrm{d}A} \end{pmatrix}. \tag{6.6}$$

The exact form of the susceptibility is now dependent upon the contributions to $\overrightarrow{H}[t]$. Equation (6.5) can also be inverted. This enables computation of the case where $\overrightarrow{\Delta h}[t] = 0$, *i. e.* the precessional motion is without external excitation. Setting the determinant

$$\det\left[\chi_{pq}^{-1}[\omega_{\text{m}}]\right] = 0, \tag{6.7}$$

this equation can be solved for the two eigenfrequencies ω_1 and ω_2. Technically not frequencies, they are colloquially called such and will be henceforth. Since the eigenfrequencies are not independently accessible in experiments, an average **eigenfrequency**

$$\omega_0 = \sqrt{\omega_1\,\omega_2} \tag{6.8}$$

is calculated by the geometric mean. The motivation behind this specific form will be obvious in a moment. In the following, the algebra will not be detailed and instead the results are simply listed. The susceptibility is always a symmetric matrix, and hence only two entries are important, the diagonal one χ_{d}, and the off-diagonal one χ_{o}.

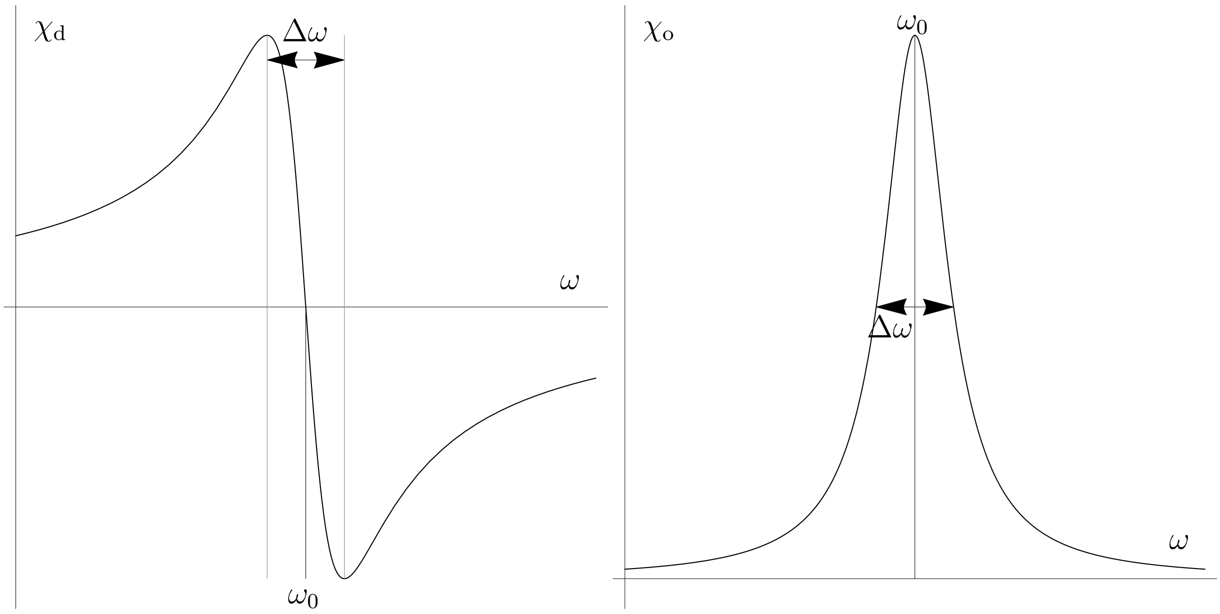

Figure 6.2: Diagonal component and off-diagonal component of the dynamic susceptibility tensor at arbitrary scale.

6.1 Zeeman field

The simplest case is the one where $\vec{H}[t]$ is a simple external Zeeman field in x-direction. This field will simply be denoted as H in the equations in the following chapter(s). Following the steps above, this yields

$$\omega_0 = \gamma_e \, \mu_0 \frac{H}{\sqrt{1+\alpha^2}} \tag{6.9}$$

and

$$\hat{\chi} = \frac{\gamma_e \, \mu_0 \, M_S}{(\gamma_e \, \mu_0 \, H - \omega)^2 + (\alpha \, \omega)^2} \begin{pmatrix} \gamma_e \, \mu_0 \, H - \omega & \alpha \, \omega \\ -\alpha \, \omega & \gamma_e \, \mu_0 \, H - \omega \end{pmatrix}. \tag{6.10}$$

Equation (6.9) is the expected *Larmor frequency*, modulated by an additional damping term. It follows the expected form from equation (2.5), since the non-linear contributions were specifically ignored. Irrespective of the exact form, the first consequence of damping is a **reduced resonance frequency**—even though the effect is miniscule. The two expected eigenfrequencies are degenerate in this case.

χ_o has the form of a **Lorentz distribution** (mathematically often known as *Cauchy distribution* [32, Cauchy distribution]). Both terms are schematically shown in figure 6.2.

A very basic interpretation of the two components, and their shapes, originates from equation (6.6). χ_d can be seen as $d\omega_m/d\omega_h$. At resonance, this is zero, as this is the preferred co-rotation at a phase shift of $\pi/2$ between $\overrightarrow{\Delta h}[t]$ and $\vec{m}$. Below resonance, the frequency wants to increase to achieve resonance, and above it, it wants to decrease. χ_o can be seen as $d\psi/dA$. Far away from resonance, only very small precession angles can be achieved. At resonance, on the other hand, very large precession angles can be achieved, limited only by damping. The second consequence of damping is thus that it **limits the angle of precession**. χ_o approaches a delta function (as the Lorentzian should) for very small damping, and thus very high precession angles. Strictly speaking, this is only true for experiments if the specific conditions allow for extension of the linearization to high angles of precession.

Even though the Lorentzian shape is no longer correct for real resonance curves, experimental values are often fitted to this distribution to extract vital statistics from the data. The third consequence of damping is that the **full width at half maximum (FWHM)**,

$$\Delta\omega = 2\ \alpha\ \omega_0, \tag{6.11}$$

increases with damping and the resonance frequency.

6.2 Demagnetization field

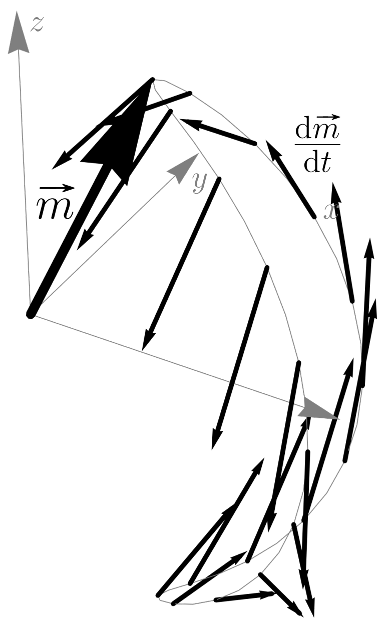

Figure 6.3: Precessional motion in thin films.

A very fundamental and interesting case results when demagnetization effects are added. The form of the demagnetization field in equation (2.30) can be simplified for the studied case. Homogeneous precession reduces demagnetization effects to surface (*i. e.* shape) effects. The integral gets dropped, and a simple vector-matrix multiplication results, with a distinct, shape-dependent, 3×3-matrix. The construction of these demagnetization tensors can be found, *e. g.*, in [30, pp. 31–34], and is based on the pioneering work by E. C. Stoner and E. P. Wohlfarth [128]. The results of FMR calculations for such cases were first obtained by C. Kittel [129]. The most interesting case, in the context of solid-state engineering, is a thin film. Using a demagnetization tensor

$$N = \begin{pmatrix} 0 & 0 & 0 \\ 0 & 1 & 0 \\ 0 & 0 & 0 \end{pmatrix}, \tag{6.12}$$

i. e. a thin film in the xz-plane, yields a resonance frequency

$$\omega_0 = \gamma_\mathrm{e}\ \mu_0 \sqrt{\frac{H(H + M_\mathrm{S})}{1 + \alpha^2}}. \tag{6.13}$$

This result is achieved via equation (6.8), originating from two distinct eigenfrequencies

$$\omega_{1,2} = \frac{\gamma_{\mathrm{e}}\,\mu_0}{1+\alpha^2}\left(H + \frac{M_{\mathrm{S}}}{2} \pm \sqrt{\left(\frac{M_{\mathrm{S}}}{2}\right)^2 - \alpha\,H\,(H+M_{\mathrm{S}})}\right). \tag{6.14}$$

These two eigenfrequencies can be assigned to the y and z direction. As the sample is now highly anisotropic, different demagnetization fields (courtesy of equation (6.12)) act, depending upon the phase of the magnetization. The precession gets distorted such that it is no longer circular, but **elliptic** (figure 6.3). This ellipticity is not resolvable in classic resonance experiments. Instead, an equivalent circular precession is measured; equivalent means here that the average swept area has to be the same. This is the generalization of *Kepler's second law* (see, *e. g.*, H. Goldstein [130, p. 73]) and results in equation (6.8).

Ellipticity occurs in basically any system without at least cylindrical symmetry. It should be noted that the curvature of the trajectory visible in figure 6.3 is negligible for the linear case examined here.

The susceptibility is given for the general case of a *Stoner-Wohlfarth particle*, *i. e.* an ellipsoid of rotation. The values of the demagnetization factors can be computed analytically [131]. In such a case, the demagnetization tensor is diagonal, yielding

$$\widehat{\chi} = \frac{\gamma_{\mathrm{e}}\,\mu_0\,M_{\mathrm{S}}}{(\gamma_{\mathrm{e}}\,\mu_0\,(H+M_{\mathrm{S}}\,(N_{22}-N_{11}))-\omega)\,(\gamma_{\mathrm{e}}\,\mu_0\,(H+M_{\mathrm{S}}\,(N_{33}-N_{11}))-\omega)+(\alpha\,\omega)^2}\times$$
$$\begin{pmatrix}\gamma_{\mathrm{e}}\,\mu_0\,(H+M_{\mathrm{S}}\,(N_{33}-N_{11}))-\omega & \alpha\,\omega \\ -\alpha\,\omega & \gamma_{\mathrm{e}}\,\mu_0\,(H+M_{\mathrm{S}}\,(N_{22}-N_{11}))-\omega\end{pmatrix}. \tag{6.15}$$

6.3 Nonlinear resonance

The treatment of resonance in this chapter so far was on a purely linear basis, *i. e.* for small $\overrightarrow{\Delta h}\,[t]$. It is indeed possible to extend the treatment to the nonlinear case, as has been shown by G. V. Skrotskii and Yu. I. Alimov [132, 133]. There are still some limitations to this process, as will become obvious.

Again starting from equation (6.1), the ansatz

$$\frac{\partial m_p\,[t]}{\partial t} = -\varepsilon_{pqr}\,m_q\,[t]\;\omega_r \tag{6.16}$$

is employed. This ansatz has the magnetization precess at the frequency ω, which is the frequency enforced on the system, around "some" field direction. Since Larmor's frequency is given by equation (6.9), this is equivalent to saying that the enforced frequency corresponds to "some" field $\overrightarrow{H}$, that is effectively enforced in the system. The direction of $\overrightarrow{\omega}$ is obviously the same as the bias field.

It should be noted here that it is indeed possible to also extend, at least in principle, the ansatz of equation (6.2) to the nonlinear case.

With equation (6.16), equation (6.1) becomes

$$\varepsilon_{pqr}\, m_q \left(\gamma_e\, \mu_0\, h_r - \omega_r\right) + \alpha\, m_q\, \omega_q\, m_p = \alpha\, \omega_p. \tag{6.17}$$

This is effectively a system of equations and can be solved for m_1, which previously was fixed at M_S.

6.3.1 Zeeman field

Replicating the case of section 6.1 yields a polynomial

$$m_1^4 - \left(1 - a^2 - \xi_0^2\right) m_1^2 - \xi_0^2 = 0, \tag{6.18}$$

with

$$a = \frac{\gamma_e\, \mu_0\, \sqrt{\Delta h_p\, \Delta h_p}}{\alpha\, \omega} \qquad \text{and} \qquad \xi_0 = \frac{\gamma_e\, \mu_0\, H - \omega}{\alpha\, \omega}, \tag{6.19}$$

that can be solved as

$$m_1 = \sqrt{\frac{1}{2}\left(1 - a^2 - \xi_0^2 + \sqrt{\left(1 - a^2 - \xi_0^2\right)^2 + 4\, \xi_0^2}\right)}. \tag{6.20}$$

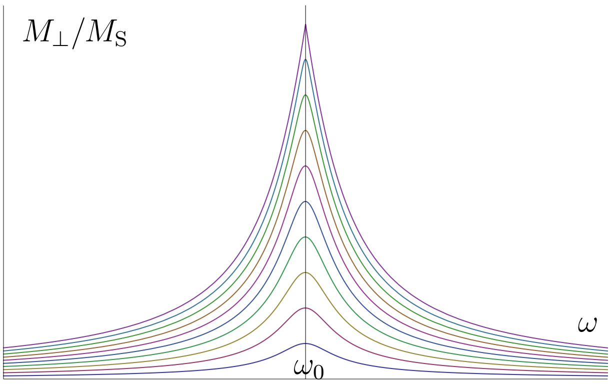

Figure 6.4: Orthogonal magnetization component (amplitude of precession) for nonlinear resonance in Zeeman field at arbitrary scale. Colored curves denote increasing $\overrightarrow{\Delta h}$. For small driving fields the shape is roughly equal to a Lorentzian, for larger ones no longer.

The orthogonal component, *i. e.* the precession amplitude and $\sqrt{1 - m_1^2}$, is plotted in figure 6.4. The curve should, in principle, be equivalent to χ_o; it is obvious that this is no longer true for higher driving fields. Following equation (6.5), the susceptibility can indeed be calculated as

$$\hat{\chi} = \frac{\gamma_e\, \mu_0\, m_1\, M_S}{\alpha\, \omega\, (\xi_0^2 + m_1^2)} \begin{pmatrix} \xi_0 & m_1 \\ -m_1 & \xi_0 \end{pmatrix}, \tag{6.21}$$

which is identical to equation (6.10), but now introduces a dependency on m_1. This susceptibility is not completely honest, as m_1 is a function of $\overrightarrow{\Delta h}$. Indeed, there does not exist a linear susceptibility (in the shape of $\mathrm{d}m_1/\mathrm{d}\Delta h_p$) since the equilibrium configuration is an extremum. Thus, the linear susceptibility is indeed only a valid approximation for small driving fields.

6.3.2 Demagnetization field

The contribution of shape effects can also be considered. The case of section 6.2 can not be replicated, however. To arrive at an analytical solution, a demagnetization tensor

$$N = \begin{pmatrix} 0 & 0 & 0 \\ 0 & 1/2 & 0 \\ 0 & 0 & 1/2 \end{pmatrix} \tag{6.22}$$

is employed. This is equivalent to an infinite rod in x-direction, or, more realistically, a long waveguide with square cross-section. The resulting polynomial is

$$\left(1+\xi_{\mathrm{N}}^2\right) m_1^4 - 2\,\xi_0\,\xi_{\mathrm{N}}\,m_1^3 - \left(1-a^2-\xi_0^2+\xi_{\mathrm{N}}^2\right) m_1^2 + 2\,\xi_0\,\xi_{\mathrm{N}}\,m_1 - \xi_0^2 = 0, \tag{6.23}$$

with

$$\xi_{\mathrm{N}} = -\frac{\gamma_{\mathrm{e}}\,\mu_0\,M_{\mathrm{S}}}{2\,\alpha\,\omega}. \tag{6.24}$$

Solving this polynomial, while in principle possible (quartic equation), produces not only a very cumbersome solution, but also introduces problems with numerical evaluation and graphical representation of the underlying physics. Instead, the polynomial can be solved for ω, yielding

$$\omega = \gamma_{\mathrm{e}}\,\mu_0 \left(\frac{H+\frac{M_\perp}{2}}{1+\left(\alpha\frac{M_\perp}{M_{\mathrm{S}}}\right)^2} \pm \sqrt{\frac{\Delta h_p\,\Delta h_p}{\left(1-\frac{M_\perp}{M_{\mathrm{S}}}\right)\left(1+\left(\alpha\frac{M_\perp}{M_{\mathrm{S}}}\right)^2\right)} - \alpha^2 \left(\frac{H+\frac{M_\perp}{2}}{1+\left(\alpha\frac{M_\perp}{M_{\mathrm{S}}}\right)^2}\right)^2} \right) \tag{6.25}$$

and the result plotted as function of $M_\perp$ and inverted graphically.

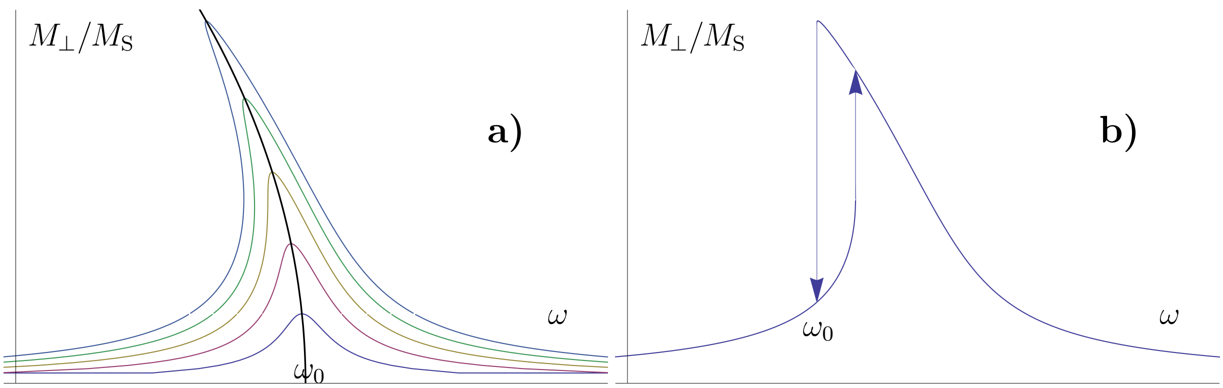

Figure 6.5: Orthogonal magnetization component (amplitude of precession) for nonlinear resonance in an infinite rod at arbitrary scale. **a)**: Colored curves denote increasing $\overrightarrow{\Delta h}$. For small driving fields the shape is roughly equal to a Lorentzian, for larger ones no longer. **b)**: Hysteresis loop for $\overrightarrow{\Delta h} > \overrightarrow{\Delta h^c}$. Arrows denote the loop direction.

The orthogonal component retrieved in such a way is plotted in figure 6.5 **a)**. For small fields, the curve is equivalent to χ_o. For larger fields, the change is now dramatic: Not only does the curve become sharper (as in figure 6.4), but it also starts to lean toward lower frequencies. This behavior is a direct result of the demagnetization contribution. The closer the system gets to resonance, the larger the precession amplitude gets. As the resonance frequency is

$$\omega_0 = \gamma_\mathrm{e}\,\mu_0 \frac{H + \frac{M_\perp}{2}}{1 + \left(\alpha \frac{M_\perp}{M_\mathrm{S}}\right)^2}, \tag{6.26}$$

the resonance frequency decreases for increasing amplitude. For $\omega < \omega_0$, ω_0 is moving toward ω until at some point they are equal and suddenly $\omega > \omega_0$. For $\omega > \omega_0$, ω_0 is moving away from ω which has to "catch" the resonance.

At a critical excitation field strength $\overrightarrow{\Delta h^c}$ (that can not be calculated analytically), the resonance peak begins to move to smaller frequencies than the $\omega < \omega_0$-curve. This is (quite aptly) called the **foldover**. This results in a **hysteresis loop** that is depicted in figure 6.5 **b)**.

Chapter 7: Classical dispersion relations

Following up from chapter 6, the requirement of homogeneous precession is dropped. Wavelike configurations are selected as specific non-homogeneous configuration, to create analytical models of magnons.

The starting point is again the implicit LLG equation, equation (2.4):

$$\frac{\partial m_p\left[\{x_w\},t\right]}{\partial t} = -\mu_0\;\gamma_{\mathrm{e}}\;\varepsilon_{pqr}\;m_q\left[\{x_w\},t\right]\;H_r\left[\{x_w\},t\right]. \tag{7.1}$$

Damping is completely ignored. It can in principle be incorporated, but does not provide any interesting new results (while making the derivation much more difficult). This time the ansatz is:

$$m_p\left[\{x_w\},t\right] = \delta_{p1}\cos\left[\psi\right] + \left(\delta_{p2}\cos\left[\omega_{\mathrm{m}}\;t\right] + \delta_{p3}\sin\left[\omega_{\mathrm{m}}\;t\right]\right)\sin\left[\psi\right]\sin\left[k_q\;x_q\right]. \tag{7.2}$$

This is equation (6.2), with an added **plane wave** contribution. In such a case, a **dispersion relation** $\omega\left[\vec{k}\right]$ is expected. The acting fields in the presented cases are

$$H_p\left[\{x_w\},t\right] = \delta_{p1}\;H^{\mathrm{Zee}} + H_p^{\mathrm{ex}}\left[\{x_w\},t\right] + H_p^{\mathrm{demag}}\left[\{x_w\},t\right], \tag{7.3}$$

i. e. the Zeeman, exchange and demagnetization fields.

7.1 Infinite media

It may seem that the derivation for an infinite medium is a pointless exercise, but this is not true. The exchange length, equation (1.3), provides a measure for the length scale on which demagnetization, *i. e.* shape, effects combat exchange. If the wavelength of the plane wave is sufficiently small compared to it, the shape effects become insignificant and the dispersion relation behaves accordingly. This is indeed true for a wide interval of wavelengths. Chapter 8 will show why this is not the true limit, however.

The first contribution is the exchange field, equation (2.16):

$$H_p^{\mathrm{ex}}\left[\{x_w\},t\right] = \frac{2\;A}{\mu_0\;M_{\mathrm{S}}}\;\frac{\partial^2 m_p\left[\{x_w\},t\right]}{\partial x_q\;\partial x_q}. \tag{7.4}$$

The ansatz, equation (7.2), can be used to rewrite that to

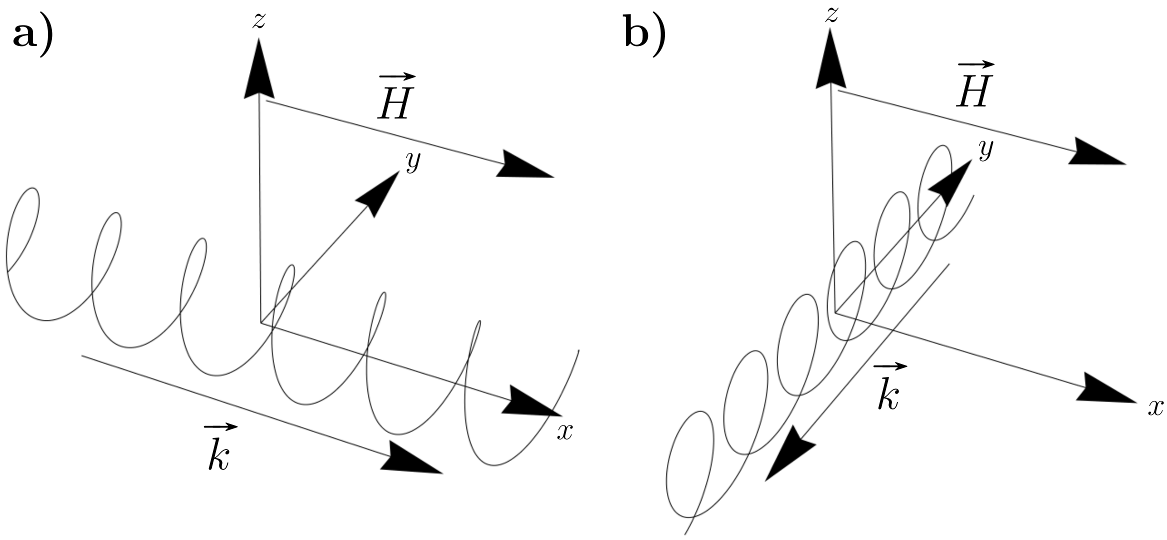

Figure 7.1: Magnetic wave in bulk material. **a)**: The wave vector $\vec{k_\parallel}$ is orthogonal to the plane of precession. **b)**: The wave vector $\vec{k_\perp}$ is in the plane of precession.

$$H_p^{\mathrm{ex}}\left[\{x_w\}, t\right] = -\frac{2\ A}{\mu_0\ M_\mathrm{S}} k_q\ k_q\ m_p\left[\{x_w\}, t\right]. \tag{7.5}$$

The time derivative of equation (7.2) again provides automatic linearization. In this linear case, the field is limited to the directions orthogonal to the Zeeman field.

The second contribution is the demagnetization field. As the magnetization is no longer uniform, a single 3×3-matrix is no longer applicable. No shape effects are present, and the demagnetization field is completely local. This makes it possible to analytically calculate the field.

Calculating the curl of equation (2.25) yields:

$$\frac{\partial^2 H_q\left[\{x_w\}, t\right]}{\partial x_p\ \partial x_q} - \frac{\partial^2 H_p\left[\{x_w\}, t\right]}{\partial x_q\ \partial x_q} = 0. \tag{7.6}$$

Inserting equation (7.2) into equation (2.26), and the result into equation (2.24), yields

$$\frac{\partial H_p\left[\{x_w\}, t\right]}{\partial x_p} = M_\mathrm{S}\ k_p\ m_p\left[\{x_w\}, t\right], \tag{7.7}$$

with the field limited to the directions orthogonal to the Zeeman field.

Applying a gradient yields a term that can be inserted in equation (7.6). In this linear case, equation (6.5) still holds. In addition, the susceptibility does not depend on position in an infinite medium, such that both $\vec{H}\left[\vec{x}, t\right]$ and $\vec{m}\left[\vec{x}, t\right]$ need to have the same position dependency, and hence, the same behavior under spatial differentiation. This makes it possible to also construct the second term in equation (7.6) and yields a demagnetization field

$$H_p^{\mathrm{demag}}\left[\{x_w\},t\right] = -M_{\mathrm{S}}\frac{k_q\, m_q\left[\{x_w\},t\right]}{k_r\, k_r}k_p, \tag{7.8}$$

where the dot product in the dividend is limited to directions orthogonal to the Zeeman field ($q = 2, 3$ in the presented case). This is again a consequence of the linearized magnetization.

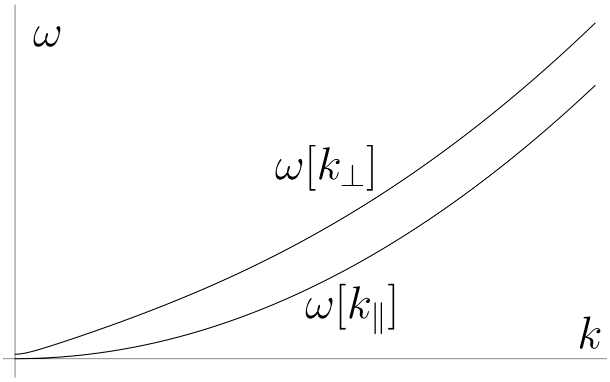

Figure 7.2: Dispersion relations for infinite medium at arbitrary scale, for wave vectors parallel and orthogonal to the bias field.

Solution for the eigenfrequencies can be performed as demonstrated in chapter 6. Equation (7.8) shows a clear dependence upon the wave vector's direction. The two limiting cases are a wave vector $\overrightarrow{k_\parallel}$ parallel to the Zeeman field, and one $\overrightarrow{k_\perp}$ orthogonal to it. The trajectory for the two cases is illustrated in figure 7.1. The different behavior of the magnetization is evident. This leads to two distinct eigenfrequencies

$$\omega\left[k_\parallel\right] = \frac{\gamma_{\mathrm{e}}}{\sqrt{1+\alpha^2}}\left(\frac{2\,A}{M_{\mathrm{S}}}k_\parallel^2 + \mu_0\,H\right) \text{ and} \tag{7.9a}$$

$$\omega\left[k_\perp\right] = \frac{\gamma_{\mathrm{e}}}{\sqrt{1+\alpha^2}}\sqrt{\left(\frac{2\,A}{M_{\mathrm{S}}}k_\perp^2 + \mu_0\,H\right)\left(\frac{2\,A}{M_{\mathrm{S}}}k_\perp^2 + \mu_0\left(H+M_{\mathrm{S}}\right)\right)}. \tag{7.9b}$$

The resulting dispersion relations are shown in figure 7.2. An angle-dependent manifold of dispersion relations is bounded by those limits. The presence of the bias field breaks the spherical symmetry of the system, even without any boundaries. Still, the general behavior is parabolic.

Also, the susceptibility can be calculated for that case:

$$\begin{aligned}\widehat{\chi} =& \frac{\gamma_{\mathrm{e}}\,\mu_0\,M_{\mathrm{S}}}{\left(\gamma_{\mathrm{e}}\left(\frac{2\,A}{M_{\mathrm{S}}}k^2 + \mu_0\,H\right) - \omega\right)^2 + (\alpha\,\omega)^2}\times \\ & \begin{pmatrix} \gamma_{\mathrm{e}}\left(\frac{2\,A}{M_{\mathrm{S}}}k^2 + \mu_0\,H\right) - \omega & \alpha\,\omega \\ -\alpha\,\omega & \gamma_{\mathrm{e}}\left(\frac{2\,A}{M_{\mathrm{S}}}k^2 + \mu_0\,H\right) - \omega \end{pmatrix}.\end{aligned} \tag{7.10}$$

In the linear case, it reproduces the same shape as for FMR.

7.2 Lifetime

The above observation, that the susceptibility reproduces the Lorentz shape of FMR, enables easy calculation of the lifetime of a specific ω-k-mode. From the characteristic function [32, Characteristic Function] of the distribution it follows immediately that the **characteristic time** can be defined as

$$t\left[m_2 = \frac{m_2\,[t=0]}{e}\right] = \tau = \frac{1}{\alpha\,\omega}. \tag{7.11}$$

This relation can also be extracted from the LLG equation by simple observation. The **lifetime** of a magnetic wave is thus **inversely proportional to its frequency**.

This relation holds in general. But as shown in subsection 6.3.2, when shape effects come into play, the precession frequency is no longer unambiguous. There are two precession frequencies, resulting in two characteristic times that are combined into an effective one. Since damping is not included in the following relations, this is not explicitly calculated.

By employing the **group velocity**

$$v_{\mathrm{gr}} = \frac{\mathrm{d}\omega}{\mathrm{d}\chi_{33}}\frac{\mathrm{d}\chi_{33}}{\mathrm{d}k}, \tag{7.12}$$

the **mean free path**

$$l = \tau\, v_{\mathrm{gr}}, \tag{7.13}$$

i. e. the distance that the wave travels during the characteristic time, can be calculated.

7.3 Thin film

Following up from the preceding section, the exchange interaction gets dropped, but shape effects are included. In inversion of the argument made in the first paragraph of the preceding section, this is then an approximation for large wavelengths. It is generally known as **magnetostatic approximation**. As in section 6.2, an infinitely extended thin film with a thickness d, centered at the origin, is examined. This calculation was initially performed by R. W. Damon and J. R. Eshbach [134].

Calculation of the demagnetization field is no longer possible purely locally, as shape effects come into play. The defining formula is equation (2.27), which can be modified using equation (6.5) to yield

$$\left(\frac{\partial^2}{\partial x_p\,\partial x_p} + \chi_{pq}\,[\omega_{\mathrm{m}}]\,\frac{\partial^2}{\partial x_p\,\partial x_q}\right) U\left[\{x_w\}\,,t\right] = 0. \tag{7.14}$$

This is **Walker's equation**, after L. R. Walker [135]. Outside of the film, $\widehat{\chi}$ is zero, and the equation simplifies to *Laplace's equation*. As in subsection 2.2.5, it is necessary to use the potential formulation since there is no defined boundary condition for the field.

Due to the problem's symmetry, the ansatz to solve equation (7.14) is a product of the in-plane and orthogonal contributions. Following equation (7.2), a cosine-wave is constructed in the film's plane. To cater for the boundary condition $U[x_3 = \infty] = 0$, simple exponentials are used outside of the film, and to cater for the film's two surfaces, a superposition of waves inside of it. The constructed solutions are thus

$$U^+\left[\{x_w\} \mid x_3 \geq +d/2\right] = A\cos\left[k_1\, x_1 + k_2\, x_2\right] \exp\left[-k_3^{\mathrm{out}}\, x_3\right] \tag{7.15a}$$

$$U\left[\{x_w\} \mid |x_3| \leq d/2\right] = \cos\left[k_1\, x_1 + k_2\, x_2\right] \left(B\cos\left[k_3^{\mathrm{in}}\, x_3\right] + C\sin\left[k_3^{\mathrm{in}}\, x_3\right]\right) \tag{7.15b}$$

$$U^-\left[\{x_w\} \mid x_3 \leq -d/2\right] = D\cos\left[k_1\, x_1 + k_2\, x_2\right] \exp\left[k_3^{\mathrm{out}}\, x_3\right], \tag{7.15c}$$

where A, B, C, and D are the unknown boundary parameters. This is clearly no longer a plane wave; it cannot be, since the demagnetization effects do not allow constant potential in z-direction. The constructed solution assumes a standing wave in the orthogonal direction, since this would form in an infinite plane. To determine the unknown parameters, the boundary conditions from classical electrodynamics (*e. g.* [9, pp. 16–19]) can be used again. The first one yields

$$U^+\left[x_3 = d/2\right] = U\left[x_3 = d/2\right] \tag{7.16a}$$

$$U^-\left[x_3 = -d/2\right] = U\left[x_3 = -d/2\right] \tag{7.16b}$$

i. e. that the potentials have to be continuous at the boundaries. The second one yields

$$\frac{\partial}{\partial x_p}\, U^+\left[x_3 = d/2\right] = \left(\frac{\partial}{\partial x_p} + \chi_{pq}\left[\omega_{\mathrm{m}}\right] \frac{\partial}{\partial x_q}\right) U\left[x_3 = d/2\right] \tag{7.17a}$$

$$\frac{\partial}{\partial x_p}\, U^-\left[x_3 = -d/2\right] = \left(\frac{\partial}{\partial x_p} + \chi_{pq}\left[\omega_{\mathrm{m}}\right] \frac{\partial}{\partial x_q}\right) U\left[x_3 = -d/2\right]. \tag{7.17b}$$

These four boundary conditions define a system of equations for the boundary parameters. Its solution depends on the specific system configuration. However, one piece is still missing: the k_3 components. Equation (7.15a) is the solution to equation (7.14) in Laplace form; inserting yields the condition

$$k_3^{\mathrm{out}}\, k_3^{\mathrm{out}} = k_1\, k_1 + k_2\, k_2. \tag{7.18}$$

Equation (7.15b) is the solution to equation (7.14); inserting yields the condition

$$k_3^{\text{in}}\ k_3^{\text{in}} = -\frac{k_1\ k_1 + (1+\chi_{22}\left[\omega_{\text{m}}\right])k_2\ k_2}{1+\chi_{33}\left[\omega_{\text{m}}\right]}. \tag{7.19}$$

This completes the system and allows solving for the respective configuration. Depending on the specific system considered, one or both components of the susceptibility may be part of the solution. This is important to distinguish and the reason why the indices are also maintained in equation (7.14). It is not necessary to solve for the boundary parameters; they are not interesting anyway. Instead the system can be written as

$$\widehat{O}\left[\chi_{pq}\left[\omega_{\text{m}}\right]\right]\{A,B,C,D\}^{\intercal} = 0 \implies \det\left[\widehat{O}\left[\chi_{pq}\left[\omega_{\text{m}}\right]\right]\right] = 0, \tag{7.20}$$

which allows to solve for the susceptibility, and hence the eigenfrequencies.

7.3.1 Backwards volume mode

The first case is when $\vec{k} \parallel \overrightarrow{H^{\text{Zee}}}$. Equation (7.20) can be solved analytically until reaching

$$\frac{2\,\imath\,\sqrt{1+\chi_{33}\left[\omega_{\text{m}}\right]}}{2+\chi_{33}\left[\omega_{\text{m}}\right]} = -\tan\left[\imath\frac{d\ k_1}{\sqrt{1+\chi_{33}[\omega_{\text{m}}]}}\right], \tag{7.21}$$

which can only be solved numerically. Here, only one component remains and therefore only one of the eigenfrequencies, for the out-of-plane direction, can be acquired. The second eigenfrequency is then simply — it can only be — the bulk case. The tangent has branched solutions, and hence multiple modes.

Equation (7.19) yields for this case

$$k_3^{\text{in}} = \pm\imath\frac{|k_1|}{\sqrt{1+\chi_{33}\left[\omega_{\text{m}}\right]}} \implies \chi_{33}\left[\omega_{\text{m}}\right] = -1-\left(\frac{k_1}{k_3^{\text{in}}}\right)^2. \tag{7.22}$$

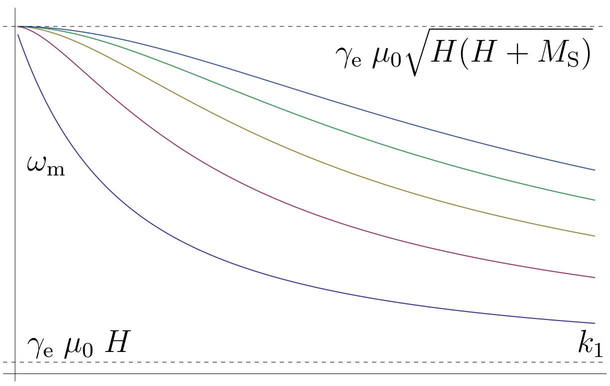

Figure 7.3: The first five modes of the dispersion relation of the backwards volume mode at arbitrary scale.

$k_1 = 0$ is the resonance case, equation (6.13), *i. e.* infinite wavelength, and hence $\chi_{33} = -1$. For increasing values of k_1, $\chi_{33} < -1$, such that $k_3^{\text{in}} < k_1$ for the limit $k_1 = \infty$. In the same limit $\chi_{33} = -\infty$, or the bulk resonance case, equation (6.9). At very large wavenumbers, the behavior is less and less determined by the demagnetization interaction as $\lambda \ll d$, and bulk-like behavior is achieved.

Hence it can be inferred that $k_3^{\text{in}} \in \mathbb{R}$. Therefore a proper standing wave is indeed

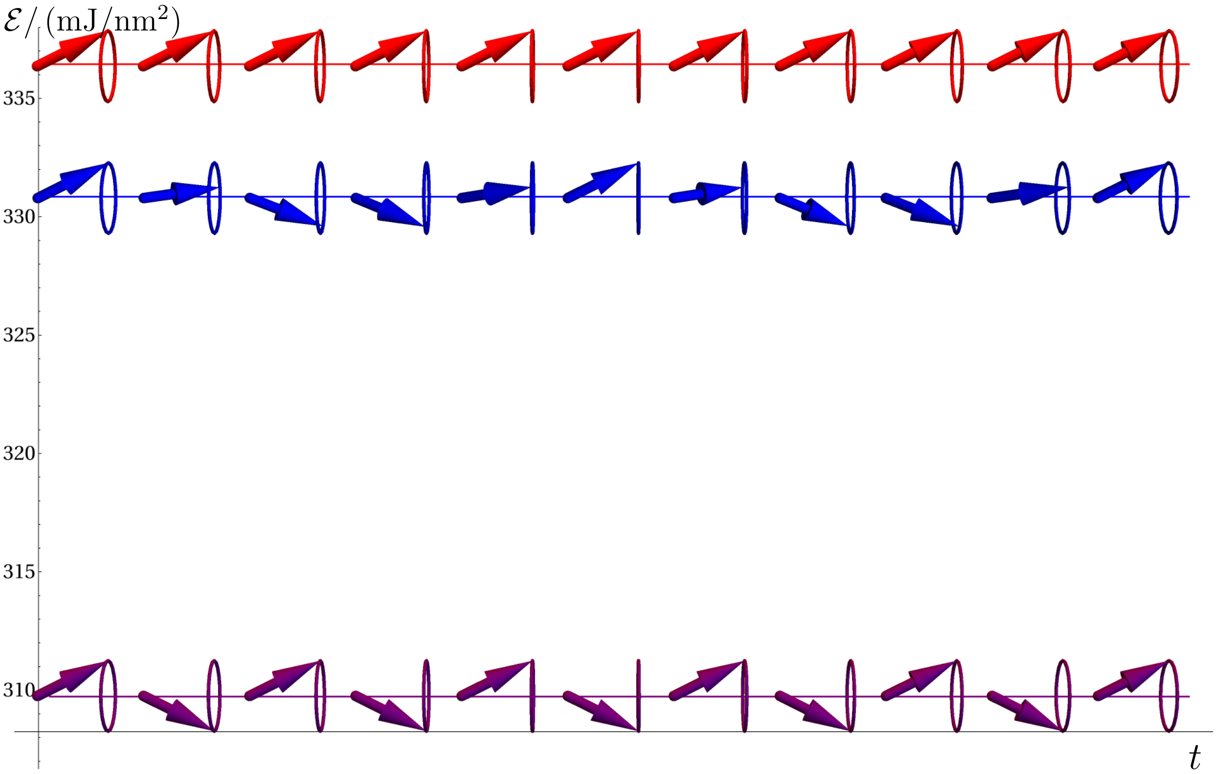

Figure 7.4: Demagnetization energy density of a spin-chain BVMSW in its own field, *modulo* the constant part, in permalloy, with different wavelengths over a full precession period. FMR (red) is on the top with highest energy, with decreasing energy for decreasing wavelength (1500 nm (blue) and 600 nm (purple)). Inserted are the corresponding magnetization configurations (precession angle exaggerated for clarity) at an arbitrary point in time. $\vec{k}$ and $\vec{H}$ are to the right.

formed in the z-direction. More than that, the group velocity of the wave

$$v_{\mathrm{gr}} \leq 0, \tag{7.23}$$

which means that the wave is traveling backwards. It is therefore generally known as a **backward volume magnetostatic wave (BVMSW)**. The first five modes are schematically shown in figure 7.3.

This behavior can be understood by examining figure 7.4. This shows one-dimensional (spin-chain) magnons along their path for three different values of k_1. In the FMR case, the demagnetization energy is maximized, while it decreases for increasing k_1. In the limit, a quasi anti-ferromagnetic configuration is reached, with minimum energy.

7.3.2 Surface mode

The second case is when $\vec{k} \perp \overrightarrow{H^{\mathrm{Zee}}}$. Equation (7.20) can then be completely solved analytically. Initially, a similar form to above is acquired,

$$\frac{2\,\imath\,\sqrt{1+\chi_{11}\left[\omega_{\mathrm{m}}\right]}\sqrt{1+\chi_{33}\left[\omega_{\mathrm{m}}\right]}}{1+(1+\chi_{11}\left[\omega_{\mathrm{m}}\right])(1+\chi_{33}\left[\omega_{\mathrm{m}}\right])} = -\tan\left[\imath\,d\,k_2\,\sqrt{\frac{1+\chi_{11}\left[\omega_{\mathrm{m}}\right]}{1+\chi_{33}\left[\omega_{\mathrm{m}}\right]}}\right]. \tag{7.24}$$

This contains both susceptibility components, so it should generate two solutions. The substitutions $\chi_{11}[\omega_\mathrm{m}] \to \chi_d[\omega_\mathrm{m}]$ and $\chi_{33}[\omega_\mathrm{m}] \to \chi_d[\omega_\mathrm{m}]$ considerably simplify the equation, such that it results in a quadratic equation providing solutions for both eigenfrequencies. For $k_2 = 0$, the resonance case, equation (6.13), is again expected. Solving the quadratic equation yields

$$\chi_d = -\left(1 + \coth[d\,k_2]\right) \pm \operatorname{csch}[d\,k_2]\,. \tag{7.25}$$

The resonance case results in $\chi_d = \{-\infty, -1\}$ as this has to reproduce equation (7.22). Calculating the eigenfrequencies from equation (7.25) and taking the geometric mean leads to

$$\omega_\mathrm{m} = \gamma_\mathrm{e}\,\mu_0\sqrt{\left(H + \frac{M_\mathrm{S}}{2}\left(1 - \exp[-d\,k_2]\right)\right)\left(H + \frac{M_\mathrm{S}}{2}\left(1 + \exp[-d\,k_2]\right)\right)}, \tag{7.26}$$

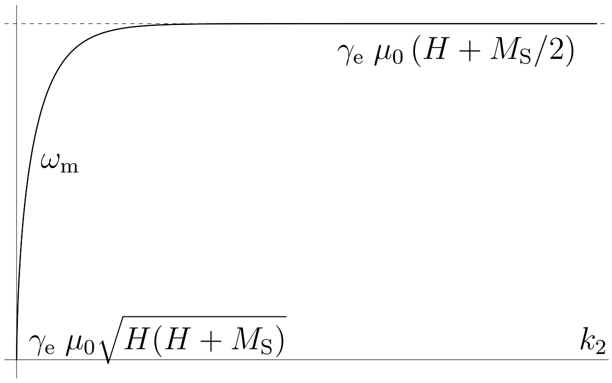

Figure 7.5: The dispersion relation of the surface volume mode at arbitrary scale.

which is shown in figure 7.5. Equation (7.19) can be calculated as

$$k_3^\mathrm{in} = \pm\imath\sqrt{\frac{1 + \chi_{11}[\omega_\mathrm{m}]}{1 + \chi_{33}[\omega_\mathrm{m}]}}\;|k_2|\,. \tag{7.27}$$

The only physical solution of equation (7.26) is for $k_2 \geq 0$, *i. e.* a wave propagating along $+y$. In that case, $k_3^\mathrm{in} \notin \mathbb{R}$, and no proper standing wave is formed. Instead, the wave has a strong maximum on one of the surfaces and propagates there. This asymmetry can be quantified by calculating the ratio of the boundary parameters inside the system. This yields

$$\frac{B}{C} = -\imath\frac{\exp[d\,k_2](2 + \chi_\mathrm{d}) + \chi_\mathrm{d}}{\exp[d\,k_2](2 + \chi_\mathrm{d}) - \chi_\mathrm{d}}. \tag{7.28}$$

Equation (7.25) provides the limits $\chi_\mathrm{d}[k_2 \to \infty] = -2$ and $\chi_\mathrm{d}[k_2 \to -\infty] = 0$. Hence the limits for the ratio are $\pm\imath$. For $k_2 \to \infty$, the wave travels along the $-z$-surface, for $k_2 \to -\infty$ along the $+z$-surface. It is therefore known as **magnetostatic surface wave (MSSW)**, or **Damon-Eshbach mode**, referring to the follow-up work of R. W. Damon and J. R. Eshbach [136].

This asymmetry can be understood by examining figure 7.6. This shows neighboring one-dimensional (spin-chain) magnons along their path for three different values of k_2. The energy of neighboring (blue/red) spin-chains in the central (uncolored) chain's field is not isotropic. This results from an asymmetric field distribution. As a consequence, the system arranges the magnetization in such a way that the maximum prospective energy is located outside of the system along on surface, such that it is not effective. Inverting k_2

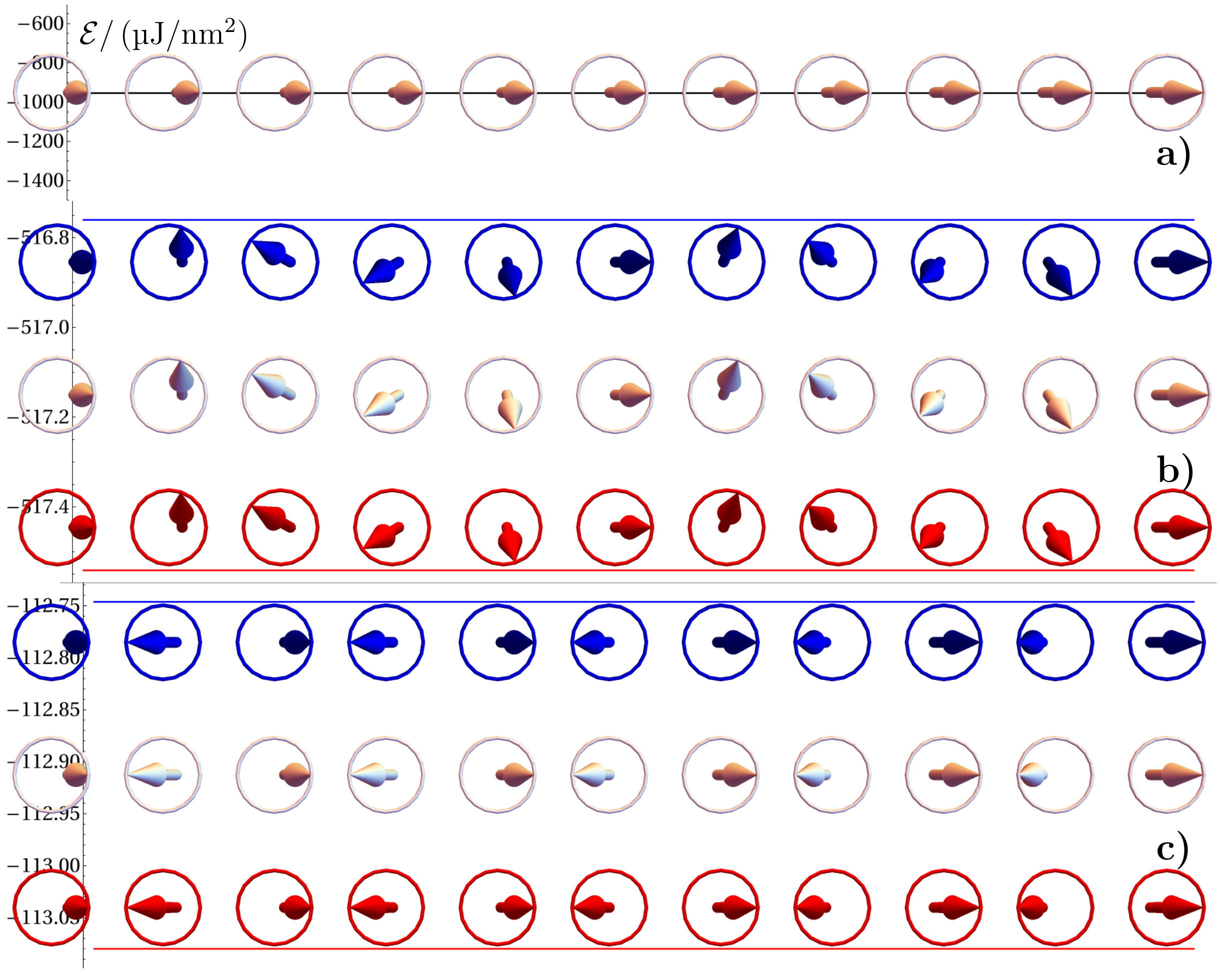

Figure 7.6: Demagnetization energy density of neighboring spin-chain MSSW (blue/red) in the field of a central (uncolored) chain, *modulo* the constant part, in permalloy, with different wavelengths. Values are the average over a full precession period. $\vec{k}$ is to the left and $\vec{H}$ out of the paper. Inserted are the corresponding magnetization configurations (precession angle exaggerated for clarity) at an arbitrary point in time. **a)**: FMR. All the neighboring chains have the same energy and are shown uncolored. **b)** (1500 nm) and **c)** (600 nm): The neighboring chains now have different energy, with the energy increasing with the wave vector.

puts it outside the opposite surface. Phenomenologically, the surface S along which the magnon is propagating can be described by

$$S_i = \varepsilon_{ijl}\, k_j\, h_l. \tag{7.29}$$

From equation (7.26), the upper limit $\omega_\mathrm{m} = \gamma_\mathrm{e}\, \mu_0\, \sqrt{H + M_\mathrm{S}/2}$ can be obtained. The group velocity of the wave is

$$v_\mathrm{gr} = \frac{\gamma_\mathrm{e}\, \mu_0}{2} \frac{d\, M_\mathrm{S}^2}{\sqrt{(2\, H + M_\mathrm{S})^2 - M_\mathrm{S}^2 \exp\left[-2\, d\, k_2\right]}} \exp\left[-2\, d\, k_2\right], \tag{7.30}$$

which can reach very high values for high wavelengths.

7.3.3 Forwards volume mode

The third case is when the Zeeman field is not in plane, but orthogonal to it. To stay in line with the backwards volume mode, $\vec{k} = k_1$. Equation (7.20) can be solved analytically until reaching

$$\frac{2\,\imath\,\sqrt{1+\chi_{11}\left[\omega_{\mathrm{m}}\right]}}{2+\chi_{11}\left[\omega_{\mathrm{m}}\right]} = -\tan\left[\imath\,d\,k_1\sqrt{1+\chi_{11}\left[\omega_{\mathrm{m}}\right]}\right], \tag{7.31}$$

which can only be solved numerically. Here, only one component remains and therefore only one of the eigenfrequencies, for the direction of the propagating wave, can be acquired. The second eigenfrequency is then simply — it can only be — the bulk case. The tangent has branched solutions, and hence multiple modes.

Equation (7.19) changes considerably to

$$k_3^{\mathrm{in}} = \pm\imath\;|k_1|\sqrt{1+\chi_{11}\left[\omega_{\mathrm{m}}\right]} \implies \chi_{11}\left[\omega_{\mathrm{m}}\right] = -1-\left(\frac{k_3^{\mathrm{in}}}{k_1}\right)^2. \tag{7.32}$$

$k_1 = 0$ is the bulk resonance case, equation (6.9), *i. e.* infinite wavelength, and hence $\chi_{11} = -\infty$. For increasing values of k_1, $\chi_{11} > \infty$, such that $k_3^{\mathrm{in}} > k_1$. Therefore the limit for $k_1 = \infty$ is $\chi_{11} = -1$, or the resonance case, equation (6.13). The behavior of the backwards volume case is simply inverted here.

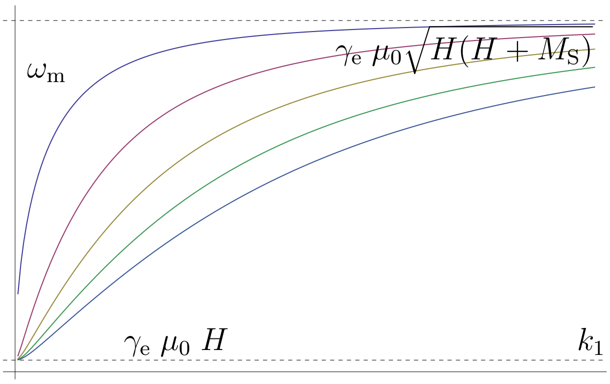

Figure 7.7: The first five modes of the dispersion relation of the forward volume mode at arbitrary scale.

Hence it can be inferred that $k_3^{\mathrm{in}} \in \mathbb{R}$. Therefore a proper standing wave is indeed formed in the z-direction. More than that, the group velocity of the wave

$$v_{\mathrm{gr}} \geq 0, \tag{7.33}$$

which means that the wave is traveling forward. It is therefore generally known as a **forward volume magnetostatic wave (FVMSW)**. The first five modes are schematically shown in figure 7.7.

The behavior can be understood by again referring to figure 7.6. The asymmetry in the orthogonal direction technically still exists here as well, but since the film is infinitely large, there is no energetical difference from pushing interaction to a surface. In real, finite systems, this will indeed happen, but practical considerations regarding magnon generation mean that this basically can not be observed.

7.4 Numerical dispersion relations

The dispersion relations obtained so far were for extremely simplified geometries. For real systems, the analytical approach is clearly not feasible. This raises the question how to obtain dispersion relations properly by numerical means.

The obvious approach would be to apply an oscillating field at one end of the geometry, solve the LLG for an appropriate amount of time, and determine the dispersion relation by time-and-space Fourier transformation of the recorded magnetization time steps. While this method has the advantage that it is not linearized, it can take a lot of computational effort to achieve sufficiently resolved data. Also, it may be desired to indeed obtain the linearized dispersion relation.

An alternative method is to try to obtain the eigenvectors and eigenvalues directly. Since the whole point of a numerical method is spatial and temporal discretization, the dispersion relation consists of discrete states. d'Aquino *et. al.* [137, 138] devised a method to extract those states directly. This is a very efficient numerical method that replaces integration of the LLG by solving a linearized eigenvalue equation.

The starting point is equation (2.4). Crossing in $\vec{m}$ from the left yields

$$\begin{aligned}&-\alpha\frac{\partial m_p\left[\{x_w\},t\right]}{\partial t}-\varepsilon_{pqr}\;m_q\left[\{x_w\},t\right]\frac{\partial m_r\left[\{x_w\},t\right]}{\partial t}=\\&\qquad\mu_0\;\gamma_{\mathrm{e}}\left(m_q\left[\{x_w\},t\right]\;H_q\left[\{m_w\},\right]\;m_p\left[\{x_w\},t\right]-H_p\left[\{m_w\},t\right]\right),\end{aligned}\tag{7.34}$$

where the dependence of the effective field on the magnetization is noted. For small oscillations, the magnetization can be decomposed into

$$m_p\left[\{x_w\},t\right]=m_p^0\left[\{x_w\}\right]+\Delta m_p\left[\{x_w\},t\right],\tag{7.35}$$

which is a static equilibrium component and a deviation from it. Since $\vec{m}\cdot\vec{m}=1$, the deviation can only be orthogonal to the equilibrium component. Linearization of equation (7.34) yields

$$\begin{aligned}&-\alpha\frac{\partial\Delta m_p\left[\{x_w\},t\right]}{\partial t}-\varepsilon_{pqr}\;m_q^0\left[\{x_w\}\right]\frac{\partial\Delta m_r\left[\{x_w\},t\right]}{\partial t}=\\&\mu_0\;\gamma_{\mathrm{e}}\left(\delta_{pr}-m_r^0\left[\{x_w\}\right]\;m_p^0\left[\{x_w\}\right]\right)\left(H_l^0\left[\{m_w\},t\right]\;m_l^0\left[\{x_w\}\right]\;\delta_{qr}-\frac{\partial H_r^0\left[\{m_w\}\right]}{\partial m_q^0\left[\{x_w\}\right]}\right)\Delta m_q\left[\{x_w\},t\right]\\&=\mathcal{P}_{pq}\left[\{x_w\}\right]\;\Delta m_q\left[\{x_w\},t\right].\end{aligned}\tag{7.36}$$

Much as in the analytical calculations, an ansatz has to be made to obtain the dispersion relation. In contrast to the analytical calculations, the wave is no longer enforced. Instead, a more general

$$\Delta m_p\left[\{x_w\},t\right] = \sum_{i=0}^{N} a^i \Big(k^{i,1}\left[\{x_w\}\right]\ \varepsilon_{pqr}\ m_q^0\left[\{x_w\}\right]\ v_r\ \cos\left[\omega^i\ t\right] \\ +k^{i,2}\left[\{x_w\}\right]\ \varepsilon_{pqr}\ \varepsilon_{rln}\ m_q^0\left[\{x_w\}\right]\ m_l^0\left[\{x_w\}\right]\ v_n\ \sin\left[\omega^i\ t\right]\Big) = \\ \sum_{i=0}^{N} a^i \Big(k^{i,1}\left[\{x_w\}\right]\ n_p^1\left[\{x_w\}\right]\ \cos\left[\omega^i\ t\right] + k^{i,2}\left[\{x_w\}\right]\ n_p^2\left[\{x_w\}\right]\ \sin\left[\omega^i\ t\right]\Big) \tag{7.37}$$

is used, where $\overrightarrow{v}$ is an arbitrary vector that has to be selected such that it is not parallel to $\overrightarrow{m^0}$. Thus, a basis $\overrightarrow{n^1}/\overrightarrow{n^2}$ to $\overrightarrow{m^0}$ is constructed, with the temporal eigenfunctions provided by the trigonometric functions, and the spatial ones by the $k^i\left[\{x_w\}\right]\overrightarrow{n^i}\left[\{x_w\}\right]$. Inserting the ansatz into equation (7.36) results in two eigenequations

$$\omega^i\ k^{i,1}\left[\{x_w\}\right]\Big(\alpha\ n_p^1\left[\{x_w\}\right] + n_p^2\left[\{x_w\}\right]\Big) - k^{i,2}\left[\{x_w\}\right]\ \mathcal{P}_{pq}\left[\{x_w\}\right]\ n_q^2\left[\{x_w\}\right] = 0 \tag{7.38a}$$

$$-\omega^i\ k^{i,2}\left[\{x_w\}\right]\Big(\alpha\ n_p^2\left[\{x_w\}\right] + n_p^1\left[\{x_w\}\right]\Big) - k^{i,1}\left[\{x_w\}\right]\ \mathcal{P}_{pq}\left[\{x_w\}\right]\ n_q^1\left[\{x_w\}\right] = 0 \tag{7.38b}$$

that can be solved for the ω^i and $k^i\left[\{x_w\}\right]$. Direct solution is not advised for $\alpha > 0$, so either damping has to be ignored (in which case the authors propose using the *Lanczos algorithm* [139] for solution), or a perturbation analysis has to be performed. This results in a set of eigenfrequencies and eigenvectors, from where the corresponding eigen-magnetization can be extracted by Fourier transformation.

This follows the general idea of computing the dispersion relation without any external stimuli, as in the analytical methods. But since a set of spatially-resolved eigenmodes is retrieved, it is possible to project any selected external excitation (*e. g.* the Oersted field of a stripline antenna) onto those eigenmodes, and hence yield the dispersion relation for this specific excitation.

Chapter 8: Quantized picture

The core idea of magnonics is the existence, at least in a mathematical picture, of quanta of wavelike magnetization-precession in materials. This is a common concept in solid state physics. Wavelike phenomena are the basis of phonons, plasmons, polarons, . . . — and magnons. Since they are obviously bosonic in nature, a formulation is necessary that brings the wavelike magnetization precession into such a picture. This has been initially presented by T. Holstein and H. Primakoff [41]. As is usual for quantum mechanics, the derivation is done in the complex. Therefore a dagger (†) means that an operator's conjugate is considered. The derivation is not strictly quantum-mechanical; its main point is that spins exists on a lattice while in a continuum formulation they exist everywhere.

8.0.1 Harmonic oscillator

Although it is not *a priori* certain that this is even possible, the bosonic picture, which is used, is that of a quantum-mechanical harmonic oscillator [140, p. 91], with the **Hamilton operator**

$$\mathcal{H} = \hbar\,\omega\,a^\dagger\,a + \mathcal{H}_0, \tag{8.1}$$

where $a^\dagger$ is the creation operator and a the annihilation operator. Both are commonly called ladder operators. $\mathcal{H}_0$ is some ground state contribution. The two operators are defined by their action on a state $|n\rangle$, where n is the oscillator's occupation number. This action is [140, p. 92]:

$$a\,|n\rangle = \sqrt{n}\,|n-1\rangle \tag{8.2a}$$
$$a^\dagger\,|n\rangle = \sqrt{n+1}\,|n+1\rangle. \tag{8.2b}$$

The operators therefore raise or lower the occupation number of the oscillator. Or, in the particle picture, they create or annihilate a particle. Since this magnon has as its key property the wave vector $\overrightarrow{k}$, equation (8.1) needs to be generalized to

$$\mathcal{H} = \hbar\sum_{\{k_w\}}\omega\left[\{k_w\}\right]\;a^\dagger\left[\{k_w\}\right]\;a\left[\{k_w\}\right] + \mathcal{H}_0, \tag{8.3}$$

which provides the requested form of the Hamiltonian.

8.0.2 Spin ladder operators

Since magnetization is, in a quantum-mechanical picture, determined by angular-momentum operators (spin, orbital and their interactions), a magnetization state is initially defined by its values of those. Similarly to above, ladder operators can be constructed. They are defined by their action [140, p. 197]

$$Z_{\pm}\,|s,z\rangle = \hbar\sqrt{(s \mp z)(s \pm z + 1)}\,|s, z \pm 1\rangle, \tag{8.4}$$

where the state $|s,z\rangle$ is defined by its spin vector $\vec{S}$, the vector's magnitude $s = \left\|\vec{S}\right\|/\hbar$, and its projection value on an axis — usually z, hence giving its value as $z = S_z/\hbar$. The operators then change the projection: $\vec{S}$ is either aligned along a preferred direction ($z = s$), determined by the bias field, or deflected from it, corresponding to an angle of precession ψ.

It is now required to transform the Hamiltonian from a spin ladder formulation into an oscillator ladder formulation. It is possible to construct a spin occupation number operator

$$\mathcal{N} = a^\dagger\, a = s - z, \tag{8.5}$$

that yields zero if the spin is aligned in the preferred direction, and increases if it gets deflected. Equation (8.4) can now be transferred into

$$Z_{+}\,|s,n\rangle = \hbar\sqrt{(2\,s - (a^\dagger\, a - 1))}\sqrt{n}\,|s, n-1\rangle \tag{8.6a}$$

$$Z_{-}\,|s,n\rangle = \hbar\sqrt{n+1}\sqrt{2\,s - a^\dagger\, a}\,|s, n+1\rangle, \tag{8.6b}$$

where use was made of the fact that the number operator reduces to the occupation number. This provides a relation between spin and oscillator ladder operators,

$$Z_{+}\,|n\rangle = \hbar\,\sqrt{2\,s}\sqrt{1 - \frac{a^\dagger\, a}{2\,s}}\;a\,|n\rangle \tag{8.7a}$$

$$Z_{-}\,|n\rangle = \hbar\,a^\dagger\,\sqrt{2\,s}\sqrt{1 - \frac{a^\dagger\, a}{2\,s}}\;|n+1\rangle. \tag{8.7b}$$

These relations are called **Holstein-Primakoff transformations**. Since $a^\dagger\, a$ is proportional to ψ, it is possible to employ a **linear approximation** here as well. This allows reducing the operators to

$$Z_{+}\,|n\rangle = \hbar\,\sqrt{2\,s}\;a\,|n\rangle \tag{8.8a}$$

$$Z_{-}\,|n\rangle = \hbar\,a^\dagger\,\sqrt{2\,s}\;|n+1\rangle. \tag{8.8b}$$

The consequences of not using the linear approximation will be explored later. The oscillator ladder operators obtained here are still entirely local, *i. e.* position dependent.

8.0.3 Momentum space

To arrive at a non-local interpretation, *i. e.* switching from position into momentum space, the ladder operators have to be Fourier transformed. The transformation reads

$$a\left[\{x_w\}\right] = \frac{1}{\sqrt{N}} \sum_{\{k_w\}}^{N} a\left[\{k_w\}\right] \exp\left[\imath\, k_p\, x_p\right]. \tag{8.9}$$

The exponential functions, which are the base functions, have to form an orthogonal basis per construction. Therefore, it is possible to compute the local operator product as:

$$a^\dagger\left[\left\{x_w^i\right\}\right]\; a\left[\left\{x_w^j\right\}\right] = \frac{1}{N} \sum_{\{k_w^i\},\{k_w^j\}}^{N} a^\dagger\left[\left\{k_w^i\right\}\right]\; a\left[\left\{k_w^j\right\}\right] \exp\left[\imath\left(k_p^i - k_p^j\right)\; x_p^i\right] \exp\left[\imath\; k_p^j\; d_p\right]. \tag{8.10}$$

d_p is the separation vector between interacting spins.

8.0.4 The meaning of quanta

It is a good idea to dwell on the concept of a magnon for a moment, and the operators introduced hitherto. The concept of momentum space obviously is only sensible for an extended system. Hence the spin ladder operators are to be applied non-locally, and the spin ladder is non-local. One rung of the spin-ladder is then a change of the **angular momentum of the whole system** by $\hbar$.

This change is, per set-up, not localized either. The Fourier transform distributes the rung wave-like over the whole system, even though a single spin-site can not support a fraction of a quantum. This makes it impossible to directly translate the quantized picture into a continuum one, and *vice versa*. However, using the proper definition of the exchange matrix, equation (2.14), the quantized picture will successfully replicate the continuum one in the limit of large wavelengths, as will be shown.

8.1 Infinite dispersion relation

For the first case, the quantized version of section 7.1 is considered, but limited to Zeeman and exchange contributions. A Hamilton operator

$$\mathcal{H} = -2\left(\mu_\mathrm{B}\; \mu_0\; H \sum_{i}^{N} z^i + \sum_{i,j}^{N} J^{ij}\; S_p^i\; S_p^j\right) \tag{8.11}$$

can be constructed, where an ensemble of spins at lattice points k is considered (*c. f.* equation (2.7)). The first step is transforming this form into one using the spin ladder operators. Applying the correct operator relation [140, p. 195], this yields

$$\mathcal{H} = -\left(2\,\mu_\mathrm{B}\,\mu_0\,H\sum_{i}^{N} z^i + \sum_{i,j}^{N} J^{ij}\left(Z_+^i\,Z_-^j + Z_-^i\,Z_+^j + 2\,\hbar^2\,z^i\,z^j\right)\right). \tag{8.12}$$

Changing into the oscillator Hamiltonian, employing equation (8.5) and (8.8), leads to

$$\begin{aligned}\mathcal{H} =& \hbar\sum_{i,j}^{N}\frac{2}{\hbar}\left(\left(\hbar^2\,s\,J^{ij} + \mu_\mathrm{B}\,\mu_0\,H\right)\delta_{ij} - 2\,\hbar^2\,s\,J^{ij}\right)a_i^\dagger\,a_j\\ &- 2\,N\,s\left(\mu_\mathrm{B}\,\mu_0\,H + \hbar^2\,s\sum_{j}^{N} J^j\right) = \hbar\sum_{i,j}^{N}\omega_{ij}\,a_i^\dagger\,a_j + \mathcal{H}_0,\end{aligned} \tag{8.13}$$

where non-linear terms were dropped and the commutation/anti-commutation relations for the oscillator ladder-operators [140, p. 90] employed. Using equation (8.10), this can be transferred into the wave picture, resulting in

$$\mathcal{H} = \hbar\sum_{\{k_w\}}\left(\sum_{\{d_w\}}\omega\left[\{d_w\}\right]\exp\left[\imath\,k_p\,d_p\right]\right)a^\dagger\left[\{k_w\}\right]\,a\left[\{k_w\}\right] + \mathcal{H}_0, \tag{8.14}$$

The term in brackets is then the dispersion relation. It can be calculated as

$$\omega\left[\{k_w\}\right] = \gamma_\mathrm{e}\,\mu_0\,H + 2\,\hbar\,s\,J\left(1 - 2\sum_{\{d_w\}}\cos\left[k_p\,d_p\right]\right), \tag{8.15}$$

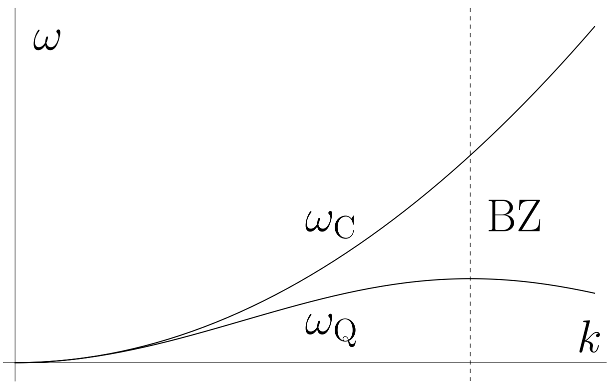

Figure 8.1: Quantized ω_Q and continuum ω_C dispersion relations for infinite medium at arbitrary scale. The limit of the Brillouin zone (BZ) is marked.

where a real quantity was introduced. What is obvious is that this derivation exhibits oscillatory behavior. Figure 8.1 shows the comparison between equation (8.15) and (7.9a). Whereas the continuum derivation (ω_C) grows uninhibited, the quantized derivation (ω_Q) introduces a maximum at $k = \pi/d$, which is the boundary of the **Brillouin zone** [141]. Although there is no band gap, the dispersion relation reaches a limit for wavelengths approaching the interatomic distance. This limit does not exist in a continuum treatment.

Taking the limit for small wave vectors in equation (8.15), thereby expanding the cosine to second order, completely replicates equation (7.9a). Although the continuum derivation clearly produces an unphysical result (as it is pretending that distances can be arbitrarily small), for realistically large wavelengths and small frequencies it is sufficiently accurate.

8.2 Demagnetization contribution

The demagnetization contribution is examined seperately. This is just to demonstrate the special method that needs to be employed for the non-linear case. The actual dispersion relation is not important here; it is difficult to calculate anyway without considering the material's structure and the introduced operators.

Equation (2.23) can be modified into a Hamilton operator

$$\mathcal{H} = -\frac{\gamma_\mathrm{e}^2\,\mu_0}{4\,\pi}\sum_{i,j}^{N}\frac{1}{\left(x_q^{ij}\,x_q^{ij}\right)^{3/2}}\left(\frac{3}{x_r^{ij}\,x_r^{ij}}x_p^{ij}\,S_p^j\,x_q^{ij}\,S_q^i - S_p^i\,S_p^j\right), \tag{8.16}$$

where again an ensemble of spins at lattice points k is considered. Applying the operator relation [140, p. 195] yields

$$\begin{aligned}\mathcal{H} = -\frac{\gamma_\mathrm{e}^2\,\mu_0}{4\,\pi}\sum_{i,j}^{N}\frac{1}{\left(x_q^{ij}\,x_q^{ij}\right)^{3/2}}&\left(-\frac{1}{2}\left(Z_+^i\,Z_-^j + Z_-^i\,Z_+^j + 2\,\hbar^2\,z^i\,z^j\right)\right.\\&\left.+\frac{3}{4\,x_r^{ij}\,x_r^{ij}}\left(x_+^{ij}\,Z_-^j + x_-^{ij}\,Z_+^j + 2\,\hbar\,x_3^{ij}\,z^j\right)\left(x_+^{ij}\,Z_-^i + x_-^{ij}\,Z_+^i + 2\,\hbar\,x_3^{ij}\,z^i\right)\right).\end{aligned} \tag{8.17}$$

This is more intricate than for the exchange interaction. Not only are spin ladder-operators used, but also distance ladder-operators.

$$x_\pm^{ij} = x_1^{ij} \pm \imath\,x_2^{ij} \tag{8.18}$$

These operators may not necessarily be sensible in a physical sense, but they allow employment of equation (8.5) and (8.8), leading to

$$\begin{aligned}\mathcal{H} = -\frac{\mu_0\,\mu_\mathrm{B}^2}{\pi}s\sum_{i,j}^{N}\frac{1}{\left(x_q^{ij}\,x_q^{ij}\right)^{3/2}}&\left(\frac{3\,x_+^{ij}\,x_+^{ij}}{2\,x_r^{ij}\,x_r^{ij}}a_j^\dagger\,a_i^\dagger + \frac{3\,x_-^{ij}\,x_-^{ij}}{2\,x_r^{ij}\,x_r^{ij}}a_j\,a_i + \right.\\&\left. 2\left(\frac{3\,x_+^{ij}\,x_-^{ij}}{2\,x_r^{ij}\,x_r^{ij}} - 1\right)a_i^\dagger\,a_j + 2\left(1 - \frac{3\,x_3^{ij}\,x_3^{ij}}{2\,x_r^{ij}\,x_r^{ij}}\right)(s-z)\right)\end{aligned} \tag{8.19}$$

where again non-linear terms were dropped and the commutation/anti-commutation relations for the oscillator ladder-operators [140, p. 90] employed. Again using equation (8.10), this can be transferred into the wave picture, resulting in

$$
\begin{aligned}
\mathcal{H} = -\frac{3\,\mu_0\,\mu_\mathrm{B}^2}{2\,\pi} s \sum_{\{k_w\}} \Bigg(\Bigg(\sum_{\{d_w\}} \frac{d_+\,d_+}{(d_q\,d_q)^{5/2}} \exp\left[-\imath\,k_p\,d_p\right] \Bigg) a^\dagger\left[\{k_w\}\right]\,a^\dagger\left[-\{k_w\}\right] \\
+ \Bigg(\sum_{\{d_w\}} \frac{d_-\,d_-}{(d_q\,d_q)^{5/2}} \exp\left[\imath\,k_p\,d_p\right] \Bigg) a\left[\{k_w\}\right]\,a\left[-\{k_w\}\right] \\
+ \Bigg(\sum_{\{d_w\}} \frac{4}{(3\,d_q\,d_q)^{3/2}} \Bigg(\Bigg(\frac{3\,d_+\,d_-}{2\,d_r\,d_r} - 1 \Bigg) \exp\left[\imath\,k_p\,d_p + 1\right] - \frac{3\,d_3\,d_3}{d_r\,d_r} \Bigg) \Bigg) a^\dagger\left[\{k_w\}\right]\,a\left[\{k_w\}\right] \Bigg) \\
= -\hbar \sum_{\{k_w\}} B^\dagger\left[\{k_w\}\right]\,a^\dagger\left[\{k_w\}\right]\,a^\dagger\left[-\{k_w\}\right] - \hbar \sum_{\{k_w\}} B\left[\{k_w\}\right]\,a\left[\{k_w\}\right]\,a\left[-\{k_w\}\right] \\
- \hbar \sum_{\{k_w\}} A\left[\{k_w\}\right]\,a^\dagger\left[\{k_w\}\right]\,a\left[\{k_w\}\right].
\end{aligned}
\tag{8.20}
$$

It is obvious that this form is very different from equation (8.3). While the Hamiltonian is supposed to be quadratic in the magnon operators, it also contains mixed terms here. Rewriting into a vector-matrix equation

$$
\mathcal{H} = -\hbar \sum_{\{k_w\}} \begin{pmatrix} a\left[\{k_w\}\right] \\ a^\dagger\left[-\{k_w\}\right] \end{pmatrix}^\dagger \begin{pmatrix} A\left[\{k_w\}\right] & B^\dagger\left[\{k_w\}\right] \\ B\left[\{k_w\}\right] & A\left[\{k_w\}\right] \end{pmatrix} \begin{pmatrix} a\left[\{k_w\}\right] \\ a^\dagger\left[-\{k_w\}\right] \end{pmatrix} \tag{8.21}
$$

shows that the central matrix needs to be diagonal for a quadratic Hamiltonian to result. In the most general case, it is possible to employ a **Bogoliubov-transformation** [142]

$$
\begin{pmatrix} a\left[\{k_w\}\right] \\ a^\dagger\left[-\{k_w\}\right] \end{pmatrix} = \begin{pmatrix} l\left[\{k_w\}\right] & m\left[\{k_w\}\right] \\ n\left[\{k_w\}\right] & p\left[\{k_w\}\right] \end{pmatrix} \begin{pmatrix} c\left[\{k_w\}\right] \\ c^\dagger\left[-\{k_w\}\right] \end{pmatrix}, \tag{8.22}
$$

as long as the new magnon operators obey the same commutation relations. This is then a **canonical transformation** that does not change the dynamics of the system; while the operators change, the Hamiltonian does not. From a physical standpoint, this is perfectly legal: the magnon operators in equation (8.3) were never defined aside from their effect, and the canonical transformation preserves just that.

Luckily, in this simple case, a principal axis transformation is a canonical transformation, and hence simply diagonalizing the operator is possible, yielding a quadratic Hamiltonian

$$
\mathcal{H} = -\hbar \sum_{\{k_w\}} \sqrt{A^2\left[\{k_w\}\right] - B^2\left[\{k_w\}\right]}\; c^\dagger\left[\{k_w\}\right]\,c\left[\{k_w\}\right]. \tag{8.23}
$$

8.3 Non-linear processes

For simple FMR, it was possible to examine the non-linear behavior in the continuum formulation. As was shown in section 6.3, this was possible by not forcing the system into a specific magnetization trajectory. This is not possible for a wave, as this is, by its very definition, a specific, time- and space-dependent, trajectory. The quantized formulation can offer remedy. While it does not easily allow quantitative analysis, it provides some qualitative insight.

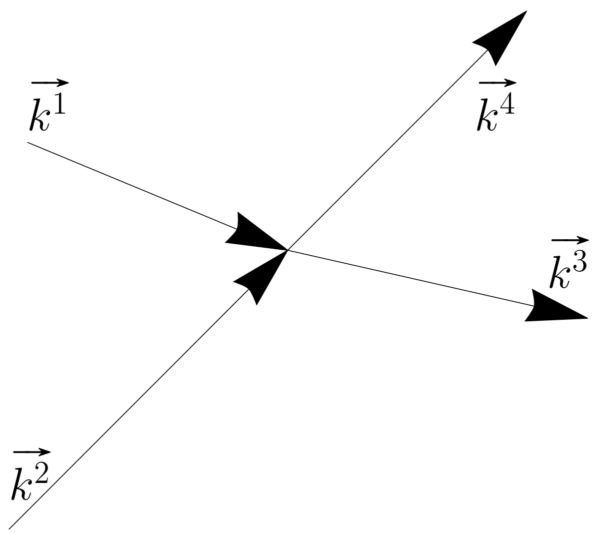

Figure 8.2: Illustration of a four-magnon scattering process.

8.3.1 Non-linear exchange

If equation (8.7) is expanded to the next higher order, additional contributions in equation (8.13) are introduced:

$$\begin{aligned}\mathcal{H} = \cdots - \hbar^2 \sum_{i,j}^{N} J^{ij} \left(2\, a_i^\dagger\, a_i\, a_j^\dagger\, a_j - \frac{1}{2}\left(a_i\, a_j^\dagger\, a_j^\dagger\, a_j + a_i^\dagger\, a_i\, a_i\, a_j^\dagger + a_i^\dagger\, a_j^\dagger\, a_j\, a_j + a_i^\dagger\, a_i^\dagger\, a_i\, a_j\right)\right) \\ - \hbar^2 \sum_{i,j}^{N} J^{ij} \frac{1}{8\, s} \left(a_i^\dagger\, a_i\, a_i\, a_j^\dagger\, a_j^\dagger\, a_j + a_i^\dagger\, a_i^\dagger\, a_i\, a_j^\dagger\, a_j\, a_j\right).\end{aligned} \tag{8.24}$$

In the wave picture, the four-operator contributions are transformed into

$$\begin{aligned}\mathcal{H} = \cdots + \hbar \sum_{\{k_w^i\},\{k_w^j\},\{k_w^l\},\{k_w^m\}} a^\dagger\left[\left\{k_w^i\right\}\right] a^\dagger\left[\left\{k_w^j\right\}\right] a\left[\left\{k_w^l\right\}\right] a\left[\{k_w^m\}\right] \times \\ \delta\left[\left\{k_p^i\right\} + \left\{k_p^j\right\} - \left\{k_p^l\right\} - \left\{k_p^m\right\}\right] \left(\frac{\hbar\, J}{2\, N} \sum_{\{d_w\}} \left(\exp\left[-\imath\, k_p^i\, d_p^j\right] + \exp\left[-\imath\, k_p^j\, d_p^j\right]\right.\right. \\ \left.\left. + \exp\left[\imath\, k_p^l\, d_p^j\right] + \exp\left[\imath\, k_p^m\, d_p^j\right] - 4 \exp\left[\imath\left(k_p^m - k_p^j\right) d_p^j\right]\right)\right).\end{aligned} \tag{8.25}$$

The operators in this contribution look very different from those in the linear treatment. The vector sum is now over four different vectors, indexed i, j, l and m, and two creation and two annihilation operators exist. This can be thus seen as a scattering event in which four magnons are taking part, **four-magnon scattering**. $\delta\left[\ldots\right]$ is the Dirac delta [143]; it ensures that **momentum conservation** is enforced in this scattering event. This process is illustrated in figure 8.2.

If the expansion of equation (8.7) is done to ever increasing orders, even-numbered scattering events will continually emerge. These processes, which are all sub-summed under four-magnon scattering, are mediated, as clearly observable by the derivation, by the exchange interaction and are therefore dominating for large wave vectors.

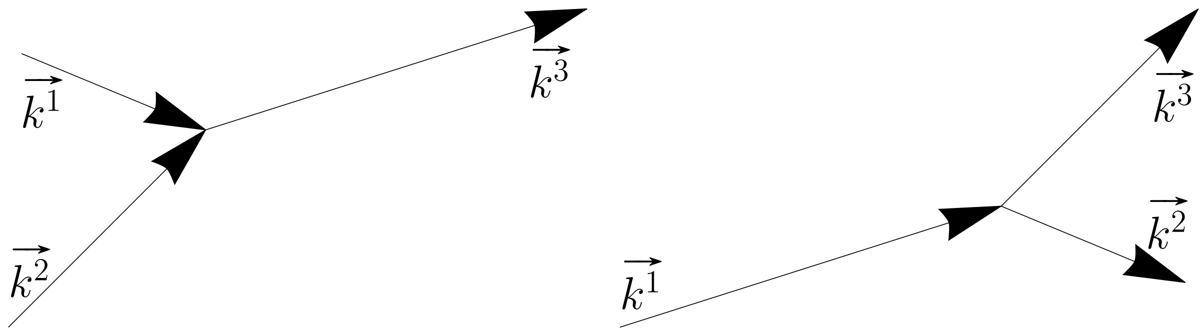

Figure 8.3: Illustration of the two possible three-magnon scattering processes.

8.3.2 Non-linear demagnetization

If equation (8.7) is expanded to the next higher order, additional contributions in equation (8.19) are introduced:

$$\begin{aligned}\mathcal{H} = \ldots + \frac{3\sqrt{2}\,\mu_0\,\mu_{\mathrm{B}}^2}{4\,\pi}\sqrt{s}\sum_{i,j}^{N}\frac{x_3^{ij}}{\left(x_q^{ij}\,x_q^{ij}\right)^{5/2}}&\left(-s\left(x_+^{ij}\,a_j^\dagger + x_-^{ij}\,a_j\right)\right.\\ &+\frac{1}{2}\left(x_+^{ij}\left(a_i^\dagger\,a_i^\dagger\,a_i + a_j^\dagger\,a_j^\dagger\,a_j\right) + x_-^{ij}\left(a_i^\dagger\,a_i\,a_i + a_j^\dagger\,a_j\,a_j\right)\right)\\ &\left.+2\left(x_+^{ij}\left(a_j^\dagger\,a_i^\dagger\,a_i + a_j^\dagger\,a_j\,a_i^\dagger\right) + x_-^{ij}\left(a_j\,a_i^\dagger\,a_i + a_j^\dagger\,a_j\,a_i\right)\right)\right).\end{aligned} \tag{8.26}$$

This is not a complete list. Terms with four, five and six operators have been dropped. In addition, summation over the terms with only one operator yields zero. In the wave picture, the three-operator contributions are transformed into

$$\begin{aligned}\mathcal{H} = \ldots + \hbar &\sum_{\{k_w^i\},\left\{k_w^j\right\},\left\{k_w^l\right\}}\\ &\left(a^\dagger\left[\left\{k_w^i\right\}\right]\;a\left[\left\{k_w^j\right\}\right]\;a\left[\left\{k_w^l\right\}\right]\delta\left[\left\{k_p^i\right\}-\left\{k_p^j\right\}-\left\{k_p^l\right\}\right]\right.\\ &\frac{3\,\gamma_{\mathrm{e}}\,\mu_0\,\mu_{\mathrm{B}}}{4\,\pi}\sqrt{\frac{s}{2\,N^3}}\sum_{\{d_w\}}\frac{d_3}{\left(d_q\,d_q\right)^{5/2}}\left(1+2\left(\exp\left[\imath\,k_p^j\,d_p\right]+\exp\left[-\imath\,k_p^l\,d_p\right]\right)\right)\\ &+a^\dagger\left[\left\{k_w^i\right\}\right]\;a^\dagger\left[\left\{k_w^j\right\}\right]\;a\left[\left\{k_w^l\right\}\right]\delta\left[\left\{k_p^i\right\}+\left\{k_p^j\right\}-\left\{k_p^l\right\}\right]\\ &\left.\frac{3\,\gamma_{\mathrm{e}}\,\mu_0\,\mu_{\mathrm{B}}^2}{4\,\pi}\sqrt{\frac{s}{2\,N^3}}\sum_{\{d_w\}}\frac{d_3}{\left(d_q\,d_q\right)^{5/2}}\left(1+2\left(\exp\left[\imath\,k_p^j\,d_p\right]+\exp\left[-\imath\,k_p^i\,d_p\right]\right)\right)\right)\end{aligned} \tag{8.27}$$

This time, a vector sum over three different vectors, indexed i, j, and l, is encountered, with either two creation and one annihilation operators, or *vice versa*. This can be seen as a scattering event in which three magnons are taking part, **three-magnon scattering**. Such processes are illustrated in figure 8.3.

If the expansion of equation (8.7) is done to ever increasing orders, both odd and even-numbered scattering events will continually emerge. Thus odd-numbered processes, which are all sub-summed under three-magnon scattering, are mediated, as clearly observable by the derivation, by the demagnetization interaction and are therefore dominating for small wave vectors.

Chapter 9: Real scattering processes

The scattering processes introduced in the preceding section necessitate the existence of magnons with different wave vectors. There are several processes that can introduce different vectors into a system, most of them also relevant for micromagnetical computations.

9.1 Temperature

With magnons being quasi-particles of a bosonic nature, it is obvious that their occupation numbers have to obey *Bose-Einstein statistics* [144, 145, 146],

$$n\left[\omega\right] = \frac{1}{\exp\left[\frac{\hbar\,\omega}{k_\mathrm{B}\,T}\right] - 1}. \tag{9.1}$$

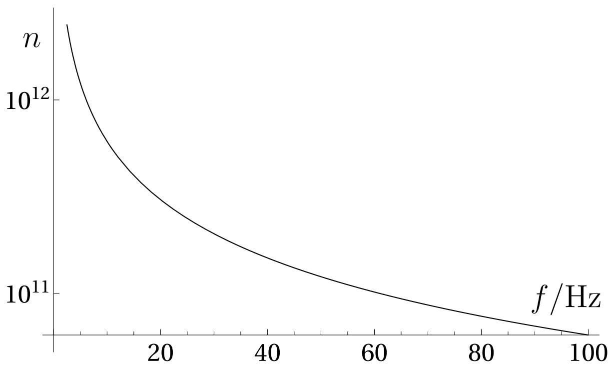

Figure 9.1: Bose-Einstein distribution at a temperature of 1 K.

This introduces the Boltzmann constant k_B and the temperature T. The distribution is shown in figure 9.1. In the sense of a continuum (classical) theory, these occupation numbers need to be coupled with the susceptibility of the dispersion relation. Below the resonance case, the susceptibility is very low, such that even the large values of the distribution for low ω result in almost no occupation. Only above the resonance case, the susceptibility is large enough to have magnons excited in such a way, even if the occupation numbers are principially very low [138]. While micromagnetic computations are always conducted in the ground state, for real systems those **thermal magnons** exist at all times. Depending on the temperature and system geometry, this may lead to significant noise in measured signals, be it in the laboratory or in application as a magnetometer.

Though out-of-scope of this work, an interesting effect that results from the bosonic behavior of magnons is their ability to undergo **Bose-Einstein condensation**, which has been shown experimentally [147].

9.2 Geometry

In real systems, and therefore also in their numerical counterparts, magnons are generally excited with stripline antennas on top of a waveguide. The Oersted field of such an antenna has a profile that follows its shape, *i. e.* the antenna's width. Figure 9.2 shows the Oersted field z-component directly below a stripline antenna in y-direction (figure 9.3 **a)** — assuming magnetization in x-direction for the BVMSW case).

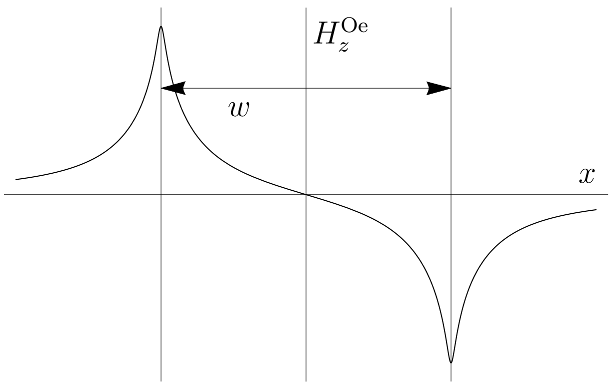

Figure 9.2: Oersted field profile of the z-component of a stripline in y-direction with width w, taken directly below the stripline.

Ideally, such an antenna should excite a wave length of twice its width w. In reality, the Oersted field is nothing like a sine-wave with that wave length. It is obvious that a large collection of different magnons will be excited, which can lead to scattering events for high enough excitation.

To optimize excitation of a specific wave vector, a straight-forward, and often experimentally employed, method is the use of a meandering antenna, as depicted in figure 9.3 **b)**. Since the Oersted field reverses phase between each arm of the antenna, the separation of the arms need to be λ, or twice the arm's width. Between the different arms a standing wave is created by interference, and this interference also reduces unwanted magnons. The concept can in principle be extended to more arms to sharpen the profile further.

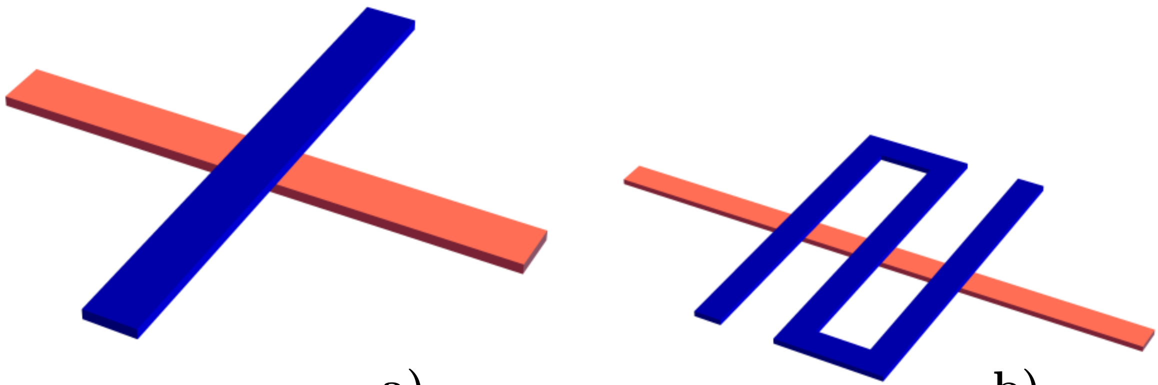

Figure 9.3: Illustration of a excitation antennas. **a)**: Single stripline antenna. **b)**: Meandering stripline antenna to excite a specific wave vector.

9.3 Parametric pumping

Although the magnon picture may be somewhat unrealistic for experimental excitations (*i. e.* large excitations, where occupation numbers can reach into the trillions), the scattering representation resulting from it provides an easily understandable framework for some observed phenomena.

A special case of scattering emerges when a magnon with a wave vector of zero, *i. e.* $a\left[\{k_w\} = 0\right]$, is the source of scattering. This happens for FMR, and at first glance it may seem that the magnon representation is not even applicable there. It surely is not treated as a magnon under normal circumstances. But the magnon formulation is still valid: it is a magnon with no momentum.

Such processes have been investigated by H. Suhl [148]. They are hence called **Suhl processes**. The **1st order Suhl-process** is the three-magnon scattering event originating from an FMR magnon, following the rule

$$k_1 = -k_2 \tag{9.2a}$$
$$\omega_{\mathrm{FMR}} = \omega_1 + \omega_2 \rightarrow \omega_1 = \omega_2 = \frac{\omega_{\mathrm{FMR}}}{2}. \tag{9.2b}$$

It is shown for the combined BVMSW/exchange dispersion relation (using the formulae developed by Kalinikos and Slavin [149]) in figure 9.4 **a)**. The plot has been calculated for a thick slab of permalloy, exhibiting a considerable frequency drop in the backward section. At the FMR frequency, a magnon is excited, and undergoes three-magnon scattering into two magnons of opposite wave vectors, effectively creating a standing wave with half the excited frequency.

The **2nd order Suhl-process** is the four-magnon scattering event originating from two FMR magnons, following the rule

$$k_1 = -k_2 \tag{9.3a}$$
$$2\,\omega_{\mathrm{FMR}} = \omega_1 + \omega_2 \rightarrow \omega_1 = \omega_2 = \omega_{\mathrm{FMR}}. \tag{9.3b}$$

It is shown for the combined BVMSW/exchange dispersion relation in figure 9.4 **b)**. At the FMR frequency, two magnons are excited, and undergo four-magnon scattering into two magnons of opposite wave vectors, effectively creating a standing wave with the excited frequency.

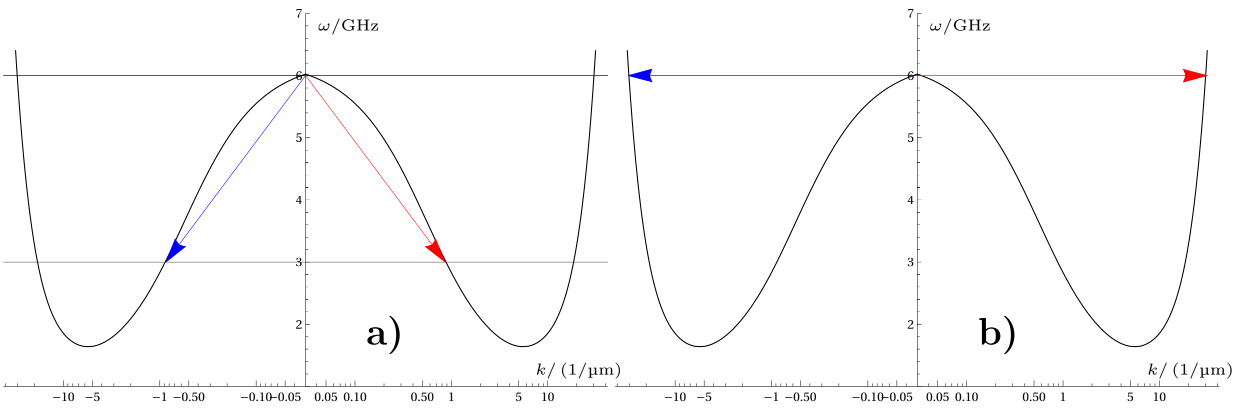

Figure 9.4: Signed log-linear BVMSW/exchange dispersion relation calculated by the Kalinikos-Slavin model. **a)**: 1st order Suhl-process. A standing wave of $\omega_{\mathrm{FMR}}/2$ is formed. **b)**: 2nd order Suhl-process. A standing wave of ω_{FMR} is formed.

The processes are visible in real-world FMR measurements, *c. f.* [150]. For finite size samples, these processes manifest themselves in distinct lines in the FMR spectrum. The plot in figure 9.4 is calculated for an infinite film, where the wave-vector space is dense, and hence the dispersion relation continuous. Since the size severely limits the possible (quantized) wave vectors, only some selected scattering processes are possible, leading to those absorption lines.

The Suhl processes assume conservation of magnonic momentum and energy. There also exist processes that do not converse these quantities. Those are generally known as **two-magnon scattering**, as they are effectively the transformation of one magnon into a different one, with the difference in energy and momentum being provided by several means. They can all be collected under the term **structural error**, *i. e.* a deviation from a single crystal with perfect geometry. An overview and theoretical treatment can be found, *e. g.* in [151, pp. 299–310].

While such behavior can be simulated numerically (*cf.* subsection 10.2.7), this is usually not done. One of the consequences of such effects is the excitation of propagating waves in real systems, even at the FMR frequency.

9.4 Scattering probabilities

It is important to understand that the scattering processes of section 8.3 are completely different from the relaxation mechanism of section 7.2. Whereas relaxation will leave the modes intact while absorbing energy, and hence reduce the occupation numbers, scattering will change the modes while conserving energy, and hence redistribute occupation numbers. The antenna excitation profile shown in figure 9.2 will initially correspond to the excited magnons, but at a distance sufficiently far away from the antenna, the magnon distribution will have changed.

Based on the Hamiltonians examined in chapter 8, a combined Hamiltonian

$$
\begin{aligned}
\mathcal{H} =& \hbar \sum_{\{k_w\}} \omega\left[\{k_w\}\right]\ c^\dagger\left[\{k_w\}\right]\ c\left[\{k_w\}\right] + \\
&\hbar \sum_{\{k_w^i\},\left\{k_w^j\right\},\{k_w^l\}} V_d^\dagger\left[\left\{k_w^i\right\},\left\{k_w^j\right\},\left\{k_w^l\right\}\right] c^\dagger\left[\left\{k_w^i\right\}\right]\ c\left[\left\{k_w^j\right\}\right]\ c\left[\left\{k_w^l\right\}\right] \times \\
&\delta\left[\left\{k_p^i\right\} - \left\{k_p^j\right\} - \left\{k_p^l\right\}\right] + \\
&\hbar \sum_{\{k_w^i\},\left\{k_w^j\right\},\{k_w^l\}} V_d\left[\left\{k_w^i\right\},\left\{k_w^j\right\},\left\{k_w^l\right\}\right] c\left[\left\{k_w^i\right\}\right]\ c^\dagger\left[\left\{k_w^j\right\}\right]\ c^\dagger\left[\left\{k_w^l\right\}\right] \times \\
&\delta\left[\left\{k_p^j\right\} + \left\{k_p^l\right\} - \left\{k_p^i\right\}\right] + \\
&\hbar \sum_{\{k_w^i\},\left\{k_w^j\right\},\{k_w^l\},\{k_w^m\}} V_e\left[\left\{k_w^i\right\},\left\{k_w^j\right\},\left\{k_w^l\right\},\{k_w^m\}\right] c^\dagger\left[\left\{k_w^i\right\}\right] c^\dagger\left[\left\{k_w^j\right\}\right] c\left[\left\{k_w^l\right\}\right] c\left[\{k_w^m\}\right] \times \\
&\delta\left[\left(\left\{k_p^i\right\} + \left\{k_p^j\right\}\right) - \left(\left\{k_p^l\right\} + \left\{k_p^m\right\}\right)\right]
\end{aligned}
\tag{9.4}
$$

can be assembled, which contains three and four-magnon interactions. For the sake of brevity, the terms containing all the exponential functions and other factors have been condensed into the various V-terms. The transformed ladder operators are employed to cater for the demagnetization interaction. Even though the three-magnon process sums over three different modes (i, j, and l), it is possible that some of the indices are identical, *i. e.* the two magnons that are annihilated (or created) are of the same mode. This is indeed a likely process, given that the external excitation will create a large population of magnons with identical wave vectors. In such cases, the sum is only performed over the two remaining indices. This is similar for the four-magnon process.

For small enough excitations, *i. e.* still in the linear regime, the scattering processes can be treated as a perturbation. *Fermi's Golden Rule* [152, p. 142] (see also [140, p. 371]),

$$w_{n \to n'} = \frac{2\,\pi}{\hbar} \left| \langle n'_{\{k_w\}} | \mathcal{H}' | n_{\{k_w\}} \rangle \right|^2 \rho\,[\mathcal{E}]\,, \tag{9.5}$$

can then be employed to calculate the scattering probabilities. n is the ground state, *i. e.* the occupation number of a mode without scattering, n' is the perturbated state, and $\mathcal{H}'$ is the perturbation part of the Hamiltonian, *i. e.* the scattering interactions. The index of the state is used henceforth to denote the ith wave vector, such that n^i is the number of magnons in the system with a wave vector of k_p^i. ρ denotes the density matrix of possible states for a given energy. For all intents and purposes, this translates into a Dirac delta function obeying to energy conservation. The delta functions conserving momentum in equation (9.4) will thus be turned into delta functions conserving energy.

When calculating the matrix element, special care has to be taken to properly take the symmetry of the V-term, regarding index change and the complex conjugate, into account (*cf.* equation (8.25) and (8.27)). The matrix element, as a scalar product, needs to be calculated as a sum over all possible vectors, at least in principle. Since a distinct set of wave vectors (corresponding to indices) that obeys the conservation of momentum has to be selected, that sum gets negated. For the probability, the sum gets reintroduced. Selecting one distinct vector i reduces this by one component, while the conservation of energy reduces this by another component.

At a far enough distance from the antenna, the magnon population can be treated as in steady state such that

$$\frac{\mathrm{d}n^i}{\mathrm{d}t} = w_{n^i \to n^i+1} - w_{n^i \to n^i-1} = 0. \tag{9.6}$$

This equation, when not enforced to be zero, is the differential equation determining the decay of any mode towards steady state. When subtracting the steady state condition resulting from equation (9.6) from its differential form, the differential equation assumes a simple proportional form. Its solution is of course an exponential function: the decay of a mode towards steady state is **exponential**.

Actually solving equation (9.6), to solve for the resulting steady state, is basically impossible. The solution has to be found for all possible modes, as a large system of coupled equations.

But it is not even necessary to compute the solution, as it is known *a priori*: it is the thermal equilibrium (*cf.* section 9.1). This is true, at least for real systems.

For a computed, micromagnetical system, the equilibrium state of a damped system will obviously be the static, unexcited system. If damping is set to zero, after sufficiently long simulation time, the magnon population will have condensated into a state where only the mode with the lowest energy is occupied, as determined by the dispersion relation. Although the FMR configuration is naively expected, this is not necessarily true if a suitable BVMSW configuration is available.

Part IV

Offset-free magnetometer based on a standing spin wave

An abridged version of the research presented here has been published in *Physical Review Applied* [153] in October of 2023.

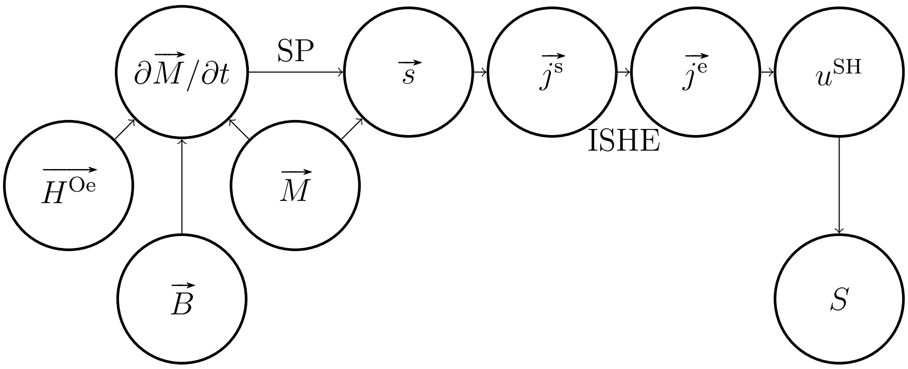

Figure 10.1: Modus of operation for the standing wave magnetometer. This is described in detail in section 10.1. The field to be measured $\vec{B}$ and the Oersted field $\overrightarrow{H^{\mathrm{Oe}}}$ of excitation antennas create a distinct precessional motion $\partial\vec{M}/\partial t$, which is translated into a voltage u by means of spin pumping and ISHE.

The design presented here is based on a **standing spin-wave** in a waveguide, with a fixed frequency and wavelength. This probes a fixed point in dispersion phase space, with the excitation efficiency changing as function of the external field. The **uniaxial shape anisotropy** is exploited to create two different magnetization configurations and therefore two different modes of precession (clockwise and counter clockwise, with respect to a fixed coordinate system). Employing **spin pumping** and the **inverse spin-Hall effect** as detection means, this results in opposite signals of identical magnitude for no measured quantity — such that the output cancels itself out — and an **offset-free transfer curve**. Conceptually, this follows the idea of the spinning current, using successive comparative measurements. The different measurements here always employ the very same parts of the system, and not different current paths and leads as for the spinning current, thereby eliminating possible sources of offset.

This is intended to be a qualitative study. As such, the parameters listed in section 1.2 are not computed, with the exception of the offset, for which a detailed analysis is provided. Since an external field is needed to switch between the two different magnetization configurations, deperming happens continuously, while effects of hysteresis will need to be considered for such a device.

10.1 System Description and Modus of Operation

The structure of the magnetometer is shown in figure 10.2. A waveguide, made out of yttrium iron garnet (YIG, $Y_3Fe_5O_{12}$), with a cross section of (50×50) nm, forms the base. The cross section is square to minimize shape effects (*i.e.* elliptic precession). It is magnetized longitudinally, *i.e.* $m_x = \pm 1$. Atop of it, platinum strip lines with width w and height $h = 15$ nm are placed at an interline distance $d = 2w$. By applying an alternating current (AC) $\overrightarrow{j^{\mathrm{AC}}}$ with a frequency $f = \omega/2\pi$ to the strip lines, where the current's phase is shifted by $+\pi$ between neighboring strip lines, a **standing spin wave** with the wavelength $\lambda = d = 2\pi/k$ is excited in the waveguide due to the Oersted fields generated by the currents. This follows the antenna concept introduced in section 9.2. A value of $\left\|\overrightarrow{j^{\mathrm{AC}}}\right\| = 2 \times 10^{11}\,\mathrm{A/m^2}$ is used here.

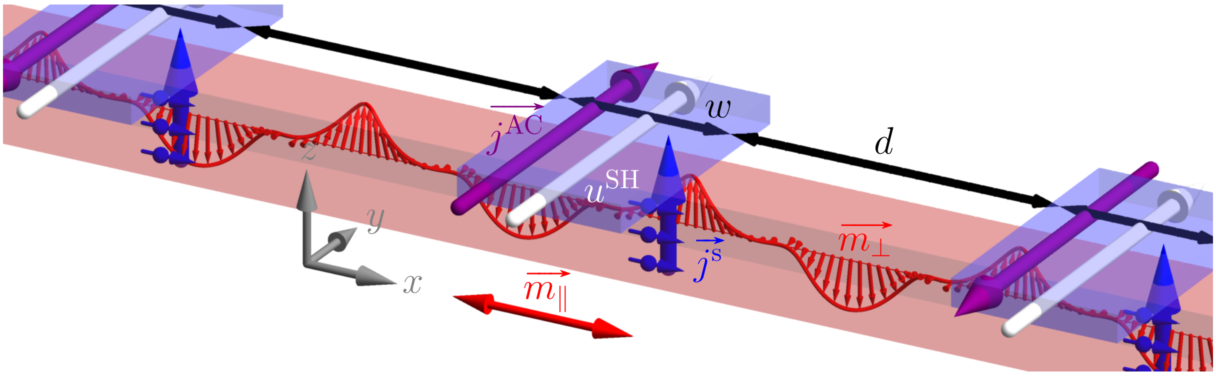

Figure 10.2: Schematic of the magnetometer structure. The YIG waveguide is in light red and the Pt strip lines are in light blue. $\lambda = d = 2\,w = 180\,\mathrm{nm}$. A standing spin wave (red, where the transversal component of the magnetization $\overrightarrow{m_\perp}$ relative to the waveguide center is depicted for an arbitrary time) is excited in the waveguide by the Oersted field of an applied (purple) AC $\overrightarrow{j^{\mathrm{AC}}}$. The precessional motion of the wave generates a (blue) spin DC $\widehat{j^{\mathrm{s}}}$ via spin pumping. The spin-Hall effect in the strip line converts this into a charge DC $\overrightarrow{j^{\mathrm{SH}}}$, resulting in a (white) measurable voltage u^{SH}. The longitudinal component of the magnetization $\overrightarrow{m_\parallel}$ is pointed along the x-axis.

The choice of f^{AC} and λ is described in the next section; for the computations $f = 3.3\,\mathrm{GHz}$ and $\lambda = 180\,\mathrm{nm}$ are used. The magnetometer therefore probes a fixed point in the dispersion phase space (figure 10.3 **a)**).

Application of an external field (figure 10.3 **a)** →**b)**) along the waveguide (*i.e.* B_x) shifts the dispersion relation in the frequency direction, thereby sweeping it along the probing point. The amplitude and rate of precession of the excited standing wave therefore change as a function of external field, acting as measured quantity.

In principle, the wavelength of the standing wave does not change during operation. Realistically, however, the standing wave is not perfectly monochromatic. Hence the probing point should be considered a 2-dimensional distribution in phase space, with the distribution acting as weights for the dispersion relation. The result is a product of both, and the antennas excite wavelengths that are not λ, as intended, but slightly larger (figure 10.3 **c)** and **d)**). Due to the shape of the dispersion-relation susceptibility, this shift becomes larger the further away the magnetometer is from the relation's maximum. The observed wavelength in computation indeed always stays 1–5 nm above $\lambda = d$.

The major advantage of using a standing wave, compared to FMR (*cf.* part V), originates from more precise excitation. For a standing wave, the excitation can be easily achieved via stripline antennas, resulting in a very sharp excitation (*c. f.* section 9.2). For homogeneous precession in a microstrip, the Suhl processes (section 9.3) will always create additional signals, polluting the magnetometer response.

Spin pumping creates a spin accumulation $\vec{s}$ at the YIG/Pt-boundary, resulting in a spin direct current (DC) $\widehat{j^{\mathrm{s}}}$ into the strip lines, with a spin direction that is parallel to the waveguide (*i.e.* j^{s}_{xz}). It also creates a spin AC with orthogonal spin direction (*i.e.* j^{s}_{yz}), but this is not important for the device. This spin DC is then transformed into a charge DC parallel to the applied AC by **ISHE**. The voltage u^{SH} that results from this current is the signal of the sensor.

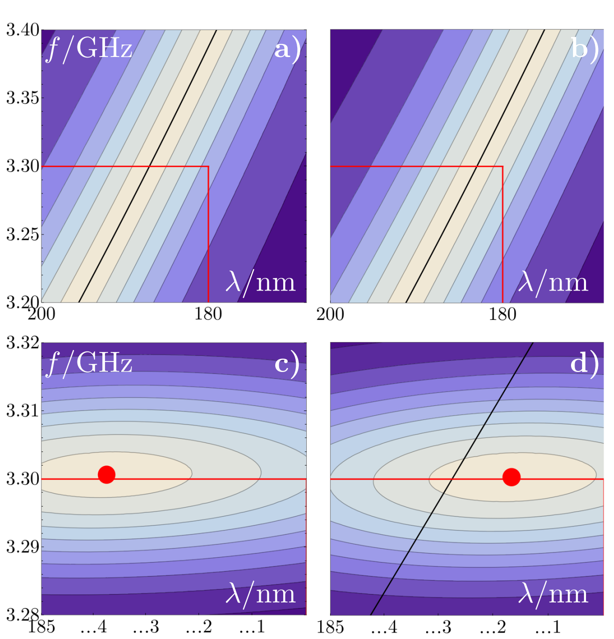

Figure 10.3: Idealized schematic of the working principle and wavelength change of the magnetometer. Shown are intensity contour plots, with light colours for high intensity. The thick black line marks the maximum of the dispersion relation. **a)** and **c)** show applied field along the $+x$-axis, **b)** and **d)** along the $-x$-axis. **a)** and **b)**: Shown is the dispersion relation; the probing point is marked. The dispersion relation gets ("vertically") shifted by field changes and the probing point lies at a different intensity, producing a different signal. **c)** (corresponding to **a)**) and **d)** (corresponding to **b)**): Detailed views of the product of the dispersion-relation susceptibility and the excitation distribution of the antenna array. This product is shifted toward the maximum of the dispersion relation and hence the resulting wave always has higher λ and f in the operational regime.

Even though the phase of $\overrightarrow{j^{\mathrm{AC}}}$ changes between neighboring striplines, the sign of j_y^{SH} does not (as it is strictly dependent upon the direction of precession and hence on the axis of precession/initial direction of magnetization). Therefore, such a setup can not be constructed as a meandering strip line, at least not unless special measures are taken. The setup examined has been selected to keep computational effort down, as spin-pumping computation in a fully conducting waveguide (which may very well be the case for a practical application) is prohibitively costly. It still adequately demonstrates the magnetometer's physics and usability.

For the setup, ten strip lines are used but this number can be increased, therefore amplifying the signal as needed. In principle, every strip line should produce the same voltage, but this is not completely true for a finite-length waveguide due to symmetry reasons.

The magnetometer's signal is then the sum of the individual strip line's u^{SH}, by assuming a serial connection. As this is overlaid by u^{AC}, a suitable low-pass filter has to be applied to isolate it. It will be seen later that this filtering is also necessary for a second reason. To achieve an offset-free transfer curve S, u^{SH} is compared for the magnetization of the waveguide in both directions along its longitudinal axis, *i.e.*

$$S = u^{\mathrm{SH}}\left[m_x = 1\right] + u^{\mathrm{SH}}\left[m_x = -1\right]. \quad (10.1)$$

Per the symmetry of the system, two signals with opposite sign are expected for $B_x = 0$ (due to s_x having the opposite sign), with the signals being identical but shifted by $2\,u^{\mathrm{SH}}\left[B_x = 0\right]$. Consequentially, the response is

$$\frac{\partial S}{\partial B_x} = 2\frac{\partial u^{\mathrm{SH}}}{\partial B_x}. \quad (10.2)$$

Such an additive measurement makes it possible to generate an **offset-free transfer curve** from a single device, with all possible deviations (fabrication and material parameters) being nullified by the symmetry. In practice, the magnetometer's magnetization needs to be periodically (on a millisecond scale) inverted by short application of an external field to enable this differential measurement.

10.1.1 Analytical Magnetometer Response

From figure 10.4 it can be reasonably estimated that the device operates in an exchange-dominated region. The magnetic susceptibility, and hence the shape of the dispersion relation, is then approximately given by equation (7.10), rewritten here as

$$\widehat{\chi} = \frac{B_\mathrm{M}}{\left(B_\mathrm{k} + B_x + B_\mathrm{es} - B_\mathrm{f}\right)^2 + (\alpha\ B_\mathrm{f})^2} \begin{pmatrix} B_\mathrm{k} + B_x + B_\mathrm{es} - B_\mathrm{f} & \alpha\ B_\mathrm{f} \\ -\alpha\ B_\mathrm{f} & B_\mathrm{k} + B_x + B_\mathrm{es} - B_\mathrm{f} \end{pmatrix}. \tag{10.3}$$

with $B_\mathrm{M} = \mu_0 M_\mathrm{S}$, $B_\mathrm{f} = 2\pi f/\gamma_\mathrm{e}$, and $B_\mathrm{k} = 2Ak^2/M_\mathrm{S}$. $\overrightarrow{B^\mathrm{es}}$ is the effective shape anisotropy field of the waveguide and $\vec{B}$ the external field; both are assumed to be exclusively in x-direction.

This introduces the first operational limit on the setup: The linear susceptibility is only valid for small amplitudes and hence the device is restricted to **small Oersted fields**. The observed angle of precession is about 3°, which is still within that limit, at least for a nanoscale waveguide. The second operational limit is immediately visible: the susceptibility is not linearly dependent on B_x and so the magnetometer response is only approximately linear for **small external fields**. In this linear case, the amplitude of the wave follows from equation (6.5), or in this case

$$M_p = \chi_{pq}\ H_q^\mathrm{Oe}, \tag{10.4}$$

where the M_x-component is set at M_S for small excitations and $\overrightarrow{H^\mathrm{Oe}}$ is the harmonic Oersted field in the yz-plane. The rate of precession can be obtained from this term by differentiation of the harmonic field with respect to time such that

$$\frac{\mathrm{d}M_p}{\mathrm{d}t} = \chi_{pq} \frac{\mathrm{d}H_q^\mathrm{Oe}}{\mathrm{d}t}. \tag{10.5}$$

For spin pumping, direct approximations are only possible for homogeneous precession, as cross-diffusion processes (see subsection 10.2.3), which no longer allow analytic solution, have to be considered here. Equation (5.11) can be employed as approximation, with $L = h$. From section 5.5, the effect of the cross diffusion can be estimated as follows: As one strip line covers, in principle, exactly half a wavelength, the distribution of spin accumulation along the waveguide below the strip line should follow the behavior of a standing wave. Since only its x-component is relevant, it can be simply treated as $\propto \sin\left[2\pi x/\lambda\right]$, and hence averaged over half a wavelength. This yields a prefactor $2/\pi$ or a simple proportionality. This is not strictly correct but should hold for the small amplitude approximation used as starting point. This spin accumulation creates a spin direct current (DC) $\widehat{j}^\mathrm{s}$ into the strip lines, with a spin direction that is parallel to the waveguide (*i.e.* j^s_{xz}). It also creates a spin AC with orthogonal spin direction (*i.e.* j^s_{yz}), but this is not important for the device. This spin DC is then transformed into a charge DC parallel to the applied AC by ISHE, equation (3.13), with the spin current equation (3.3) limited to diffusion:

$$j_y^{\mathrm{SH}} = 2\frac{e}{\mu_{\mathrm{B}}} D_0\, \Theta_{\mathrm{SH}}\, \frac{\partial s_x}{\partial z}. \tag{10.6}$$

Averaging over the current for the total height of the strip line removes the coordinate dependence. Assuming a long enough strip line (which is true in practice), boundary effects can be ignored for analytical purposes and a simple Ohmian approximation made for the voltage u^{SH} that is resulting from this current. *N. b.* that the high frequencies involved render this approximation invalid for the oscillatory components but it is valid for the stationary one. Also, the spin drift-diffusion model is formulated using Ohm's law, such that the analytical model and numerics agree.

From the presented equations and arguments, the expected voltage can be approximated, and, more importantly, the **response**

$$\frac{\partial u^{\mathrm{SH}}}{\partial B_x} \propto \frac{B_{\mathrm{f}}(B_{\mathrm{k}} + B_x + B_{\mathrm{es}} - B_{\mathrm{f}})}{((B_{\mathrm{k}} + B_x + B_{\mathrm{es}} - B_{\mathrm{f}})^2 + (\alpha\, B_{\mathrm{f}})^2)^2}, \tag{10.7}$$

where all the amassed material constants and system parameters have been factored out. The signal, as could be expected, is roughly of square Lorentzian shape. Indeed, the fits in the plots shown herein have all been performed with a Lorentzian distribution, as that is still a good approximation of its square variant. The response is then of the same shape as the diagonal susceptibility χ_{d}. It is clearly not linear, as previously stated. This is only the case for small external fields.

10.2 Simulation Results

Spin-pumping effects are computed using the method presented in part II. The effects are only computed after the standing wave has properly formed (after 400 excitation cycles), and then only the generated spin current, but not the feedback effects due to spin torque. Aside from long computation times, a fundamental simulation problem prohibits this, as will be shown.

To facilitate computation of spin pumping in this way, an interaction layer has to be defined where the *s*-*d*-coupling (between the waveguide's *d*-electrons and the strip lines *s*-electrons) is active. The layer is located in the waveguide, directly underneath each stripline, with a thickness of 1 nm. This also includes an overhang to both sides of the strip line of 1 nm. For the purpose of the simulation, this interaction layer has the properties of both the waveguide and the strip line. To account for the fact that computation is not done fully self-consistently, the spin torque, and the change of local damping, is approximated by increasing the Gilbert damping in the interaction layer from 2×10^{-4} to 1×10^{-2}. This is a reasonable approximation; both experimental results (with a bulk increase in YIG/Pt systems by a factor of five [154]) and the results in section 5.5 suggest an increase around the order of 250 for the interaction layer. It has to be noted here that an interaction layer of 1 nm is not realistic; the *s*-*d*-interaction is likely limited to a single atomic Pt layer, hence a value of 0.2 nm is more sensible. Since such a thin layer is numerically challenging to handle, the larger value is used. This means that the voltages presented herein faithfully capture the qualitative behavior of the device but are most likely an order of magnitude higher than what would be measured in experiment. The modified Gilbert damping is reduced by a factor of five to account for the large interaction-layer thickness, to arrive at 1×10^{-2}.

The total waveguide length is 7.32 µm, with the strip line battery of size $14\lambda = 2.52$ µm centrally located. The outermost 2 µm of both ends of the waveguide have increasing Gilbert damping (parabolic trajectory) to suppress the outgoing magnon while reducing reflections. The wave is only standing in the center of the system, and starts to have propagating character further away from it, resulting from asymmetry. A longer waveguide and/or reflecting boundaries are methods to suppress that.

Table 10.1: Material parameters used.

Waveguide			
Gilbert damping	α	0.0002	
Waveguide and interaction layer			
saturation magnetization	M_S	1.4	kA/m
exchange coupling	A	22.5	MeV/m
Interaction layer			
Gilbert damping	α	0.01	
electronic coupling	J	411	meV
Striplines and interaction layer			
electronic diffusion constant	D_0	50	cm²/s
conductivity	C_0	4.5	MS/m
spin-flip time	τ_{sf}	8	fs
spin-Hall angle	Θ_{SH}	0.1	

The material parameters that were used are listed in table 10.1. Spin diffusion, demagnetization, magnetic exchange, and the Oersted field of the strip lines are computed.

To find a suitable probing point, a dispersion relation and a voltage spectrum for the system will be computed.

10.2.1 Demagnetization-field correction

Computation of the demagnetization interaction relies on the boundary of the magnetic system, as shown in subsection 4.2.4. A problem arises since the boundary of the magnetic system, *i. e.* the waveguide, is not the boundary of the simulated system. The FIREDRAKE-package does only support boundary meshes for the complete system, but not for submeshes. This means that the demagnetization interaction is calculated with a wrong boundary, and results in a wrong field.

The remedy this, the following procedure is implemented:

- The mesh of the magnetic system is split off from the mesh of the simulated system.
- The LLG is solved in this subsystem, with the modified Gilbert damping as stand-in for the spin torque.
- The configuration of the subsystem, *i. e.* $\vec{m}$ and $\vec{H}$, is copied to the full system.
- The spin-pumping equation is solved.

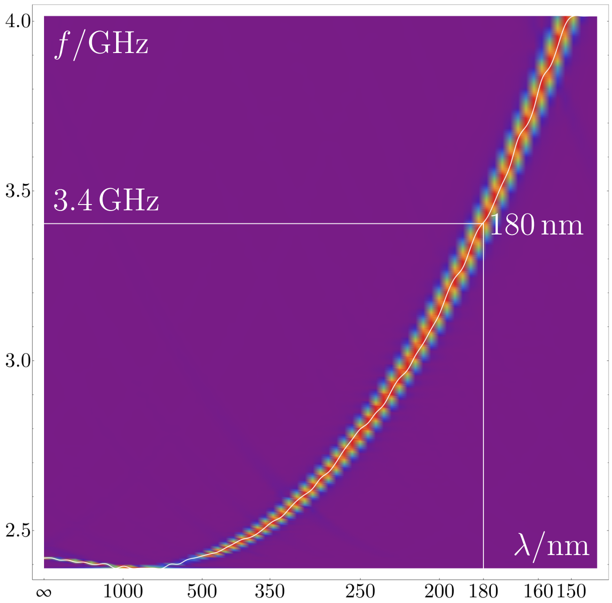

Figure 10.4: Magnon dispersion relation for a longitudinally magnetized YIG waveguide of (50×50) nm cross section. An interpolated approximation (white) has been overlaid on the color map. The magnon exhibits backward-volume magnetostatic behavior. The white cross lines denote the position at $\lambda = 180$ nm and approximately $f = 3.4$ GHz.

This disallows self-consistent computation, but corrects the error of the demagnetization field computation.

10.2.2 Dispersion relation

The dispersion relation is computed as outlined in section 7.4. The result is shown in figure 10.4. The relation does not take antenna geometry into consideration. It exhibits backward-volume magnetostatic behavior for large wavelengths; the magnetometer is already operating in the parabolic exchange regime.

The value of λ selected for a real device is determined by the position of FMR. The wave number (and therefore λ) should be located at a suitable distance from the FMR condition (to enable a standing wave being properly formed) but preferably as close as possible to maximize excitation. $\lambda = d = 2\ w = 180$ nm, and therefore $w = 90$ nm, is selected. This position is marked in figure 10.4 by the white cross lines.

10.2.3 Waveform

Figure 10.5 **a)** shows the signal (no filtering) for $f = 3.4$ GHz. Even though a constant voltage from spin pumping can be naively expected, there is a major oscillating contribution.

This can be understood in the following way. From equation (3.13) it follows that the spin-current component j^{s}_{xz} creates the charge-current component j^{SH}_{y} via ISHE. But by the simple mathematical definition (cross product), j^{s}_{zx} (exchanged indices) also creates j^{SH}_{y}. j^{s}_{zx} is a current along the waveguide, indicating a gradient of the spin accumulation component s_z along the waveguide. This is illustrated in figure 10.6: due to the excitation, the standing wave always has a node at the center of the stripline, corresponding to small precession (in principle, even none) and, hence, little generated spin accumulation. At the edges of the strip line, the precession is markedly stronger but with opposite phase between the two edges. Thus the generated spin accumulation in z-direction is also opposite, forming said spin gradient. This relation inverts itself half a cycle later, creating an oscillating spin current j^{s}_{zx} and, hence, an oscillating contribution to j^{SH}_{y}.

Indeed, for any spin wave (standing or as a magnon), such an oscillating gradient always exists at any point of the waveguide. This effect is not noticed in experiments, however. This results from the large surface area used to generate a measurable signal (see, *e.g.* [112, 49]). In the presented magnetometer setup, where every stripline is centered around a node

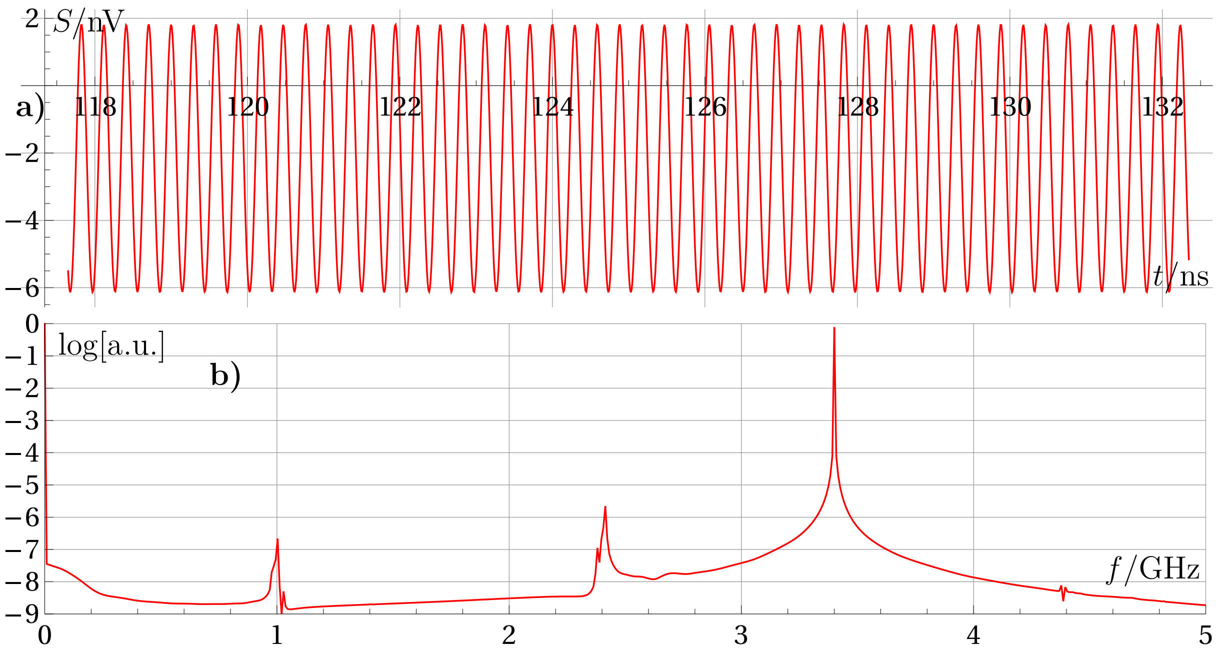

Figure 10.5: a): Inverse spin-Hall signal at 3.4 GHz and $m_x = 1$ without external field. The total signal is dominated by a constant shift and a 3.4 GHz oscillation from excitation. **b)**: Frequency spectrum (Fourier transform) of the signal in **a)**. Other contributions, arising from spectral leakage, are also noticeable.

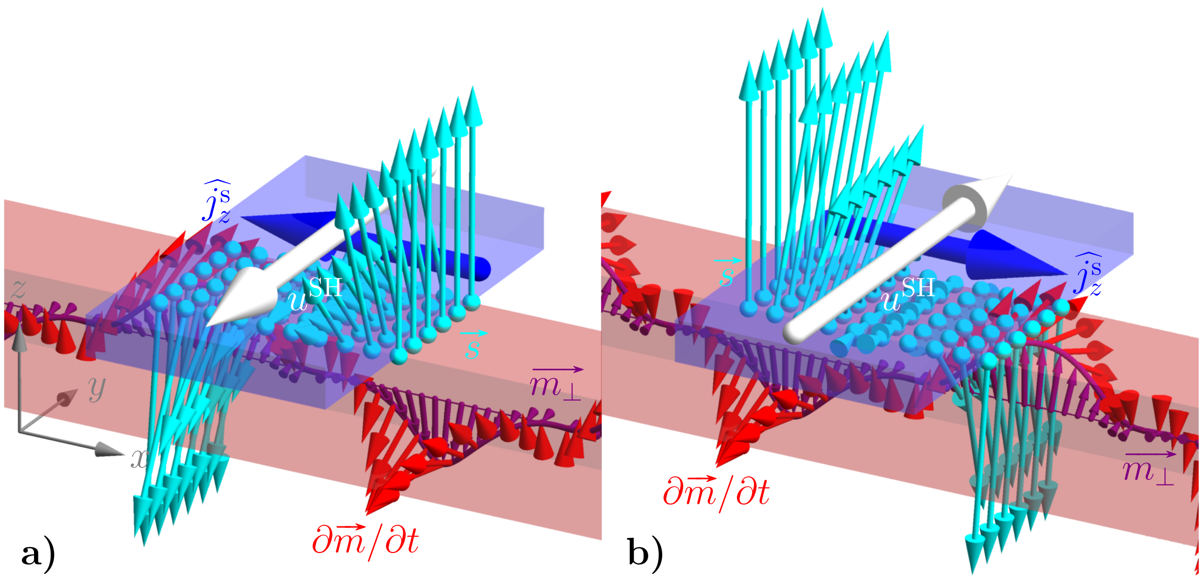

Figure 10.6: The current of z-spins $\vec{j}_z^{\mathrm{s}}$, *i.e.* the z-component of $\hat{j}^{\mathrm{s}}$, pumped by the standing wave. For any time, the standing wave (red) has a distinct phase angle and amplitude at any point along the waveguide, with corresponding precession vector (purple arrows). The spin accumulation generated at the interface boundary (cyan spheres and arrows) then has varying direction and magnitude, creating a resulting spin current (blue) along the waveguide, and a corresponding voltage (white). **a)** and **b)** show states separated by half a cycle.

of the standing wave, with the detectors width $\lambda/2$ (*cf.* figure 10.2), the oscillatory part is maximized. In experiments, the constant part is cumulative over the total surface area (usually many orders of magnitude larger than the spin-pumping area of the detection strips used here), while the oscillatory part is not. It is therefore reduced to almost unnoticeable noise in experiment.

A frequency spectrum of the signal is shown in figure 10.5 **b)**. The dominant contributions, a constant signal originating from j^{s}_{xz}, and an oscillation at 3.4 GHz from j^{s}_{zx}, can be easily seen. Aside from those, other modes are also noticeable, which result from spectral leakage. It is therefore evident that a constant signal, and hence an offset-free response of the magnetometer, can only be achieved after sufficiently long measurement time, to generate a clean signal. With that said, again to keep computation times manageable, signal processing is limited to 50 cycles (≈ 15.2 ns). For further considerations, an 800 MHz low-pass filter is applied to the signal, to extract the constant part. Only the central 10 ns of the result are then averaged, to drop the numerical artifacts introduced at the start and end of the signal due to the filtering operation.

10.2.4 Frequency spectrum

To find the probing frequency, a frequency sweep for the defined $\lambda = d = 2\,w$ is performed. Figure 10.7 **a)** shows the spectrum of the magnetometer for $m_x = 1$. This can be understood as a slice through the dispersion relation, at λ, now also taking the antenna geometry into consideration. The FMR around 2.35 GHz is the dominant feature, whereas the small "line" of the standing wave is located around 3.4 GHz, as expected from the dispersion relation. The error bars near the FMR are considerable. This is expected since FMR means homogeneous precession, while the antenna configuration enforces a standing wave inside the system. This standing wave can not properly form under this circumstances.

Figure 10.7 **b)** shows the vicinity of the standing-wave peak but now the values (and corresponding Lorentz fits) of both magnetization orientations are plotted. The linewidth (full width at half maximum) is 188 nm. It is immediately noticeable that the signals are mirrored at the x-axis, *i.e.* $u^{\mathrm{SH}}\,[m_x = 1] = -u^{\mathrm{SH}}\,[m_x = -1]$. Additive measurement of both configurations should therefore always provide an offset-free signal. The magnetometer's probing frequency is chosen as 3.3 GHz, on the peaks' left slope.

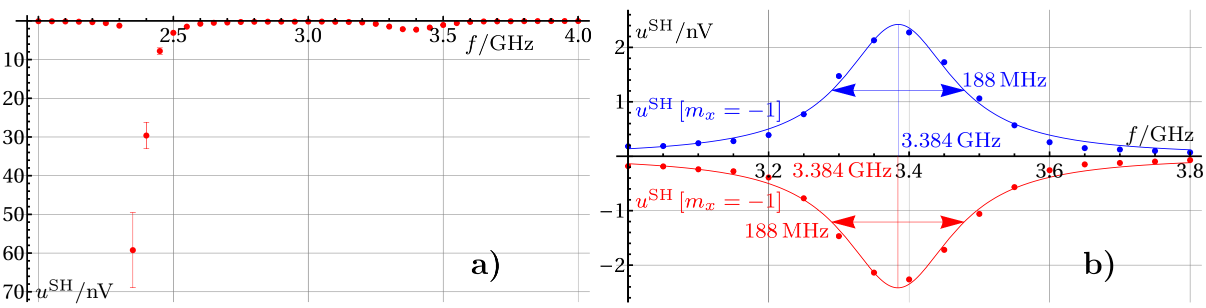

Figure 10.7: a): Signal spectrum of $u^{\mathrm{SH}}\,[m_x = 1]$ (red) of the magnetometer. The values shown here are calculated as a 10 ns-average of the 800 MHz low-pass filtered signal. The error bars denote the standard deviation of this average. **b)**: Detailed view near the standing-wave's peak. $u^{\mathrm{SH}}\,[m_x = -1]$ in blue, red as before. Data points are computed values, plotted lines a fitted Lorentzian, with parameters noted in the plot.

10.2.5 Signal output

Figure 10.8 shows the output of the magnetometer as a function of the external field along the waveguide, *i.e.* B_x, the field to be measured. Figure 10.8 **a)** shows the two signals for $m_x = \pm 1$. Their behavior is identical; the only difference is the sign of the offset of the zero-field case, which corresponds to the sign of m_x. This is expected from figure 10.7 **b)**. In figure 10.8 **b)** the two signals have been combined into the single transfer curve of the magnetometer as per equation (10.1).

From the symmetry argument, the offset for the zero-field case ($B_x = 0$) is expected to be of equal magnitude, but opposite sign, for the two cases. This, of course, cannot be expected for a numerical computation. The computed voltages u^{SH} are $-1.4684\,\mathrm{nV}$ and $1.4729\,\mathrm{nV}$ (ignoring the small standard deviation of those values). This results in an offset of $4.5\,\mathrm{pV}$, or $5\,\mathrm{nT}$. This remaining offset results from several factors:

1. There are errors resulting from numerical computation itself.
2. Due to long computation times and time limits on the VSC, simulation runs had to be divided into smaller segments (three parts for the standing wave to form and two parts for spin-pumping calculation). Restarting of the numerical integrator introduces a noticeable error at the start of each segment.
3. The generated voltage signal was still limited to approximately 15.2 ns, which introduces severe spectral leakage in the Fourier transform and hence makes the filtering operation not very accurate. Figure 10.5 **b)** uses the Fourier transform from a single, locally computed signal eight times as long, to minimize leakage.

The way the transfer curve is generated is by summing the two individual signals from figure 10.8 **a)**. By the same symmetry argument, the difference Δu between the two signals can be expected to be constant. This is plotted in figure 10.9 **a)**.

While the sign does not matter, the fact that it is not constant and shows some structure is important. The observed structure can be attributed to numerical errors, resulting from

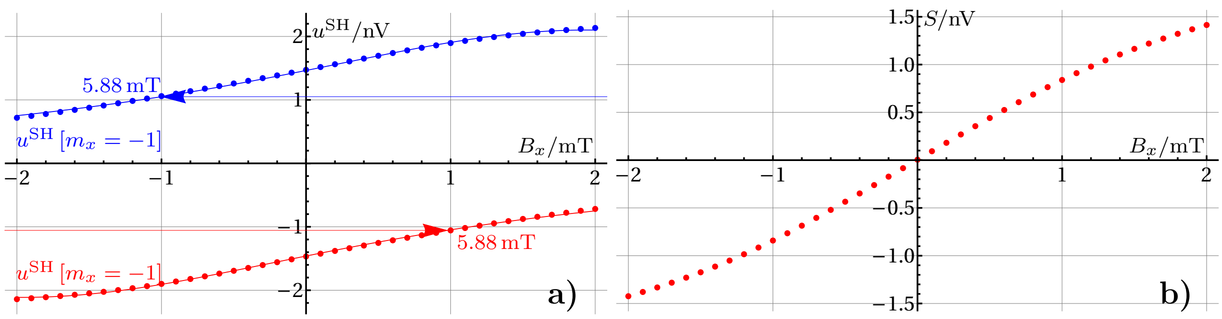

Figure 10.8: a): Magnetometer voltage signal as function of detected field at 3.3 GHz. The values shown here are calculated as a 10 ns-average of the 800 MHz-lowpass-filtered $u^{\mathrm{SH}}\,[m_x = 1]$ (red) and $u^{\mathrm{SH}}\,[m_x = -1]$ (blue). Data points are computed values and plotted lines a fitted Lorentzian, with line widths noted in the plot. **b)**: Magnetometer transfer curve obtained by adding the individual curves from **a)** per equation (10.1).

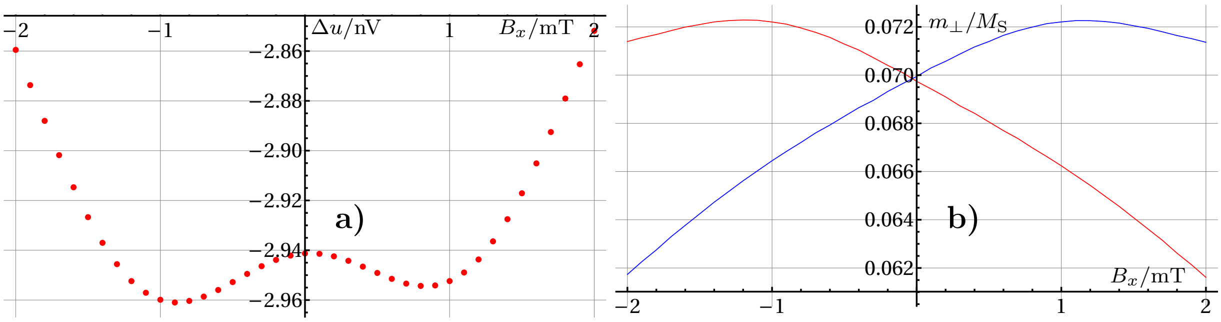

Figure 10.9: a): Magnetometer voltage difference as function of detected field at 3.3 GHz. The values shown here are calculated as a 10 ns-average of the 800 MHz-lowpass-filtered u^{SH}. **b)**: Maximum magnetization transversal component (maximum wave amplitude) in the waveguide as function of detected field at 3.3 GHz. $m_x = 1$ (red) and $m_x = -1$ (blue).

the precessional motion as a function of the magnetic field. Figure 10.9 **b)** shows the maximum transversal magnetization, *i. e.* the magnon amplitude, in the waveguide for the two cases. This shape corresponds to the voltage peak of the standing wave in figure 10.7 **b)**. Since the working point is located at the flank of the peak, this gets replicated here.

A larger amplitude also means faster precession (in that $\mathrm{d}\vec{m}/\mathrm{d}t$ is larger). It can therefore be inferred from figure 10.9 **b)** that the numerical error of the individual voltages should be larger for higher amplitude, simply due to numerical limits for faster processes. In figure 10.9 **a)**, the errors of the two signals get combined, resulting in noticeable peaks at roughly the positions where amplitude, and hence precession speed, reaches a maximum. This then also means that the real Δu is of lower magnitude than the numerical results.

The fact that the peaks in figure 10.9 **a)** are not symmetrical, and also why the offset does not vanish, may simply originate from the built-in asymmetry of the finite-element mesh, introducing asymmetrical numerical errors.

10.2.6 Transversal field effects

Transversal external fields (B_y and B_z) also have an effect on the generated signals. Naively, the axis of precession can be expected to be tilted away from the longitudinal axis of the

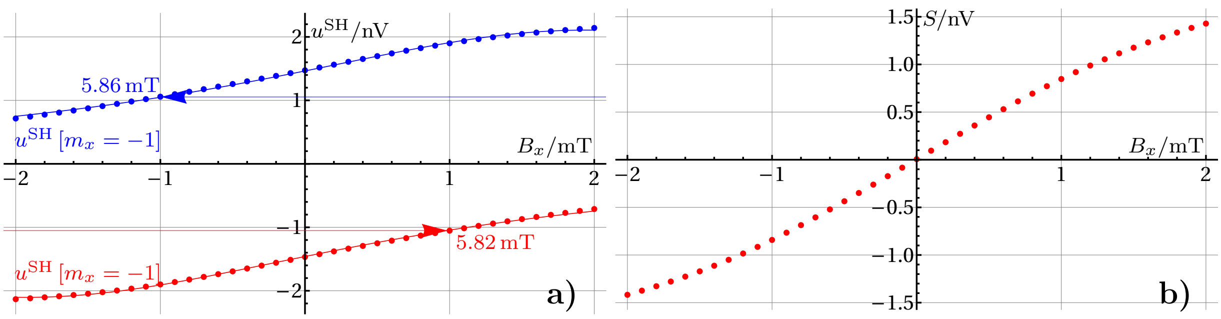

Figure 10.10: a): Magnetometer voltage signal as function of transversal field at 3.3 GHz. The values shown here are calculated as a 10 ns-average of the 800 MHz-lowpass-filtered u^{SH} [$m_x = 1$] (red) and u^{SH} [$m_x = -1$] (blue). Data points are computed values and plotted lines a fitted Lorentzian, with line widths noted in the plot. **b)**: Magnetometer transfer curve obtained by adding the individual curves from **a)** per equation (10.1).

waveguide. Hence the generated voltage should be different. Due to the symmetry, the transfer curve should again be offset free but the slope of the transfer curve should change. To test that assumption, the computation from the prior subsection was repeated for an external field $\vec{B} = (B_x, B_x, B_x)^\intercal$. The results are shown in figure 10.10.

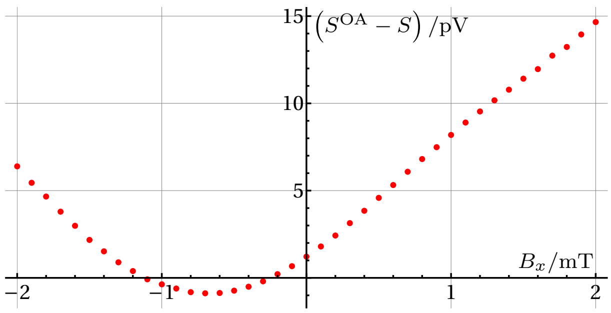

Figure 10.11: Magnetometer signal difference created by transversal components as function of detected field at 3.3 GHz.

The expected slope change was identifiable in simulations. The difference between the signals with and without transversal contributions is depicted in figure 10.11. What is immediately noticeable is that there is even a difference at zero field, although this is clearly wrong from a physics viewpoint. The difference results from different segmentation of the computations (the consequences of it have been mentioned above): 3+2 for the normal signal and 4+4 for the transversal case (due to higher computational complexity). Therefore, the error from restarting the integrator is different in both cases and introduces the difference (this difference can not be expected to be just a constant shift, valid for all fields).

The field-dependent behavior of the difference can be understood with the help of figure 10.9 **a)**. The left peak is more pronounced there and hence it is not unexpected that comparison of two such signals amplifies this peak.

The observed slope change is thus most likely originating from mesh asymmetry, rather than actual physics. In any case, for the small fields for which the magnetometer is be useable, the effect would most likely be very low since a working design would use a relatively long waveguide, with the resulting shape anisotropy providing a large resistance to precession tilt.

10.2.7 Fabrication errors

Numerical (and analytical) setups tend to be perfect. Since fabrication errors are an obstacle to creating an offset-free magnetometer, it seems only reasonable to simulate those errors. To do so, statistical deviations are applied to the simulated system. Also, hysteresis effects from locally incomplete magnetization inversion can be approximated by this approach.

To simulate a system with fabrication errors, an error term was added to the relevant system dimensions (antenna sizes and positions). This was done by drawing from a normal distribution, with μ being the original dimension and $\sigma = 0.1\mu$. The resulting values are listed in table 10.2.

Table 10.2: Modified system dimensions. o is the position offset.

	Width	Height	
Waveguide	50.2829 nm	48.3336 nm	
Antenna	w/nm	h/nm	o/nm
1	101.691	11.8031	+2.42
2	98.5148	14.1532	+7.886
3	77.955	14.6202	+0.706
4	75.7064	14.2496	−12.226
5	102.86	14.3876	+11.743
6	89.9662	16.7913	−5.6602
7	81.6407	17.0589	+5.684
8	89.9388	13.9901	+15.15
9	71.6058	12.9165	−13.251
10	89.7372	14.4093	+12.54

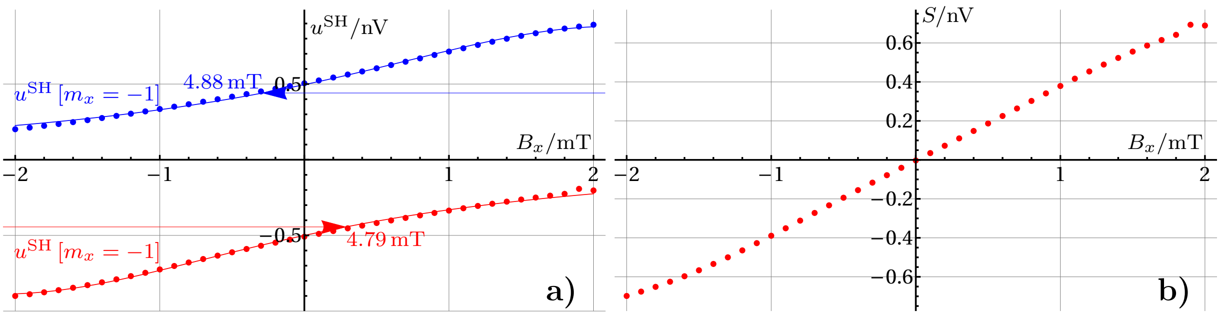

Figure 10.12: a): Magnetometer voltage signal as function of detected field with simulated fabrication errors at 3.3 GHz. The values shown here are calculated as a 10 ns-average of the 800 MHz-lowpass-filtered u^{SH} $[m_x = 1]$ (red) and u^{SH} $[m_x = -1]$ (blue). Data points are computed values and plotted lines a fitted Lorentzian, with line widths noted in the plot. **b)**: Magnetometer transfer curve obtained by adding the individual curves from **a)** per equation (10.1).

In addition, to simulate material defects, a random field was introduced to the waveguide. This was done by drawing from a normal distribution, with $\mu = 0\,\text{mT}$ and $\sigma = 0.1\,\text{mT}$ for each vector component, at each vertex of the finite element mesh. This resulted in a small, random, and fluctuating field within the waveguide.

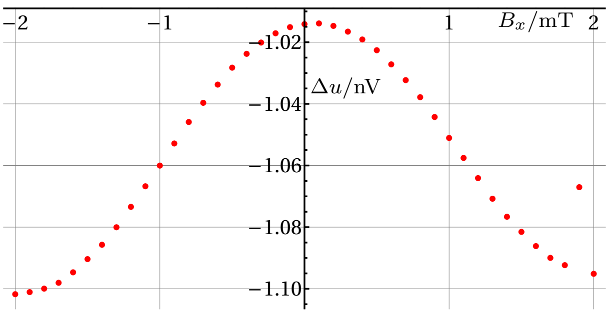

Figure 10.13: Magnetometer voltage difference as function of detected field with simulated fabrication errors. The values shown here are calculated as a 10 ns-average of the 800 MHz-lowpass-filtered u^{SH}.

The deviations introduced are intentionally very large to be able to discern any effects from numerical errors. A very obvious, and easily understandable, consequence of this process is that the amplitude of the generated standing wave is lower than for the optimal case. Deviations in antenna size and position mean that the single excitations no longer add up optimally. Figure 10.12 shows the signal output(s) and the resulting transfer curve for such a case. Although the behavior is as expected, the signal magnitude drops to approximately half its original value. In contrast to the optimal configuration, it is no longer possible to attribute the remaining offset completely to numerical errors. This is not unexpected: as the magnetometer's concept relies on symmetry, the large deviations from that symmetry that have been introduced invalidate the concept.

Again, by the same symmetry argument, the difference Δu between the two signals can be expected to be constant. This is plotted in figure 10.13. The structure observable in figure 10.9 **a)** is now absent; again, the sign does not matter. It can thus no longer be said that only numerical errors contribute to the remaining signal offset. The symmetry of the system is now notably broken and complete cancellation of the offset can no longer be expected.

10.3 Realization

For the application case, two characteristics are of special interest compared to the numerical examination: increasing the signal strength that can be reaped from the device and ensuring efficient usability and fabrication.

The antenna and detector strip lines can be separated. The antenna thickness can then be increased to reduce the current density necessary for excitation, and hence Joule heating and increase lifetime. The detector thickness can be decreased to increase the generated charge-current density. The antenna and detector strip lines do not necessarily need to be colocated any more. The waveguide can have tapered ends to completely suppress wave reflection or optimized length and antenna positions to have suitable reflection at the ends. This further reduces the necessary current but the strong stray field at the ends may change the reflected wave's behavior and introduce significant offset.

For a standing wave that is generated via an array of antennas, the free path of a magnon, and therefore the material's damping, is of limited consequence. This is exacerbated by the additional damping due to spin pumping. Therefore, the employment of a material with ultralow damping does not provide any advantages, especially if it is difficult to fabricate. There then exist two possible variants:

- The waveguides can be fabricated from conducting material. This increases the spin current, and hence the signal, as it is no longer generated by the interaction layer but in the depth of the material on a length scale on the order of λ_{sf}. Having a conducting waveguide means that the detector strip lines short out. To remedy this, instead of the voltage, the charge current can be directly used as the signal and the orthogonal strip lines replaced by ones covering a single waveguide (figure 10.14 **a)**). The waveguides can therefore have reduced cross section, as the relevant dimension is now the length, which needs to be larger. This also extends the linear regime, hence allowing a higher wave amplitude and signal. The waveguide separation needs to be

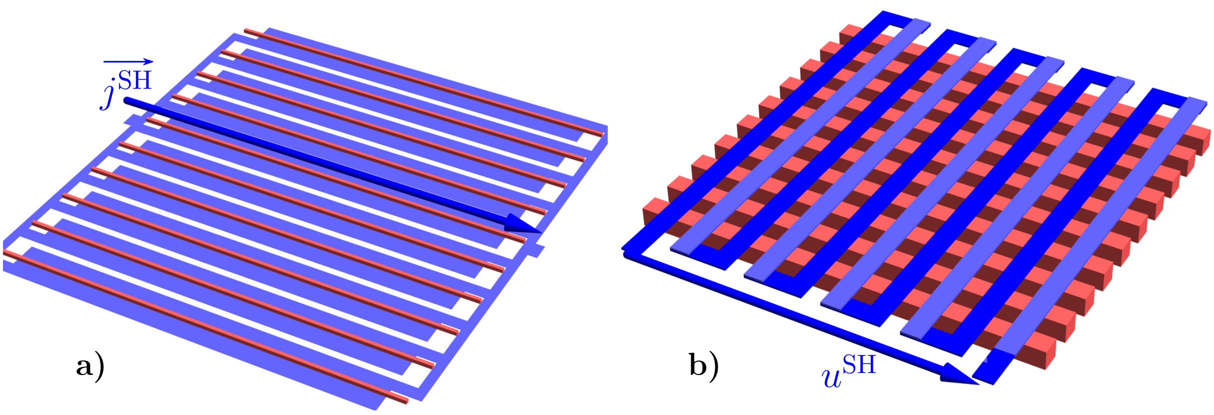

Figure 10.14: Proposed realization variants of the concept. The excitation antennas are not shown for clarity. Waveguides are in light red, current-carrying detectors and vias in shades of blue. **a)**: Variant using the generated current as output signal. **b)**: Variant using the generated voltage as output signal. Every second stripline of the detector (light blue) is raised such that it does not collect a signal to enable correct addition of signal voltages.

higher to account for the detectors. The antenna strip lines have to be separated from the waveguides by a dielectric layer. The pattering of the detector strip lines and vias, and the additional dielectric layer, introduce additional complexity. For this variant, a large number of long waveguides increases the signal.

- The waveguides can be fabricated from non-conducting material, as in the example analyzed herein. As opposed to the first variant, the spin current is lower, there is no short wiring, the voltage can be collected using orthogonal strip lines, and the waveguides can be shorter but need to have a larger cross section. Waveguide separation can be lower, limited by dipolar coupling. No dielectric layer needs to be inserted. The detector strip lines need to be connected in such a way as to correctly add up the voltages. Figure 10.14 **b)** shows the version with simpler structure, where a meandering strip line is employed, with every second strip line raised such that it does not collect a signal. The alternative version, with a more complex but more efficient structure, is not shown here. The strip lines are not connected with each other at the end but by an additional layer of vias above, connecting opposite ends of the strip lines. This yields a more complex spiral-like structure. For this variant, a large number of crossing points between waveguides and detector strip lines increases the signal.

Although the design analyzed in the computations herein follows the insulator-and-voltage approach, this has been mostly for computational reasons. It seems that the conductor-and-current approach offers superior performance in application.

Periodical inversion of the magnetization, to provide the two signals for additive measurement, is a challenge in a realized system. It is, at the core, the dilemma of the ease of switching the magnetization *vs.* the stability against transversal fields. There are some possibilities to achieve proper inversion using on-chip structures. Elaborate switching schemes are most likely necessary in this case. Such methods have been explored by others, as the problem is a common one. It is advantageous that detection and antenna lines exist in this device, because those can be employed as support. The whole device can be sandwiched between large strip-line antennas. Pulsed signals in the excitation antennas can nucleate domains [155], which can then be grown by the large field of the antenna. Another possibility to create local domains is through the use of spin-orbit torque, generated by current through the detection lines [156]. Microwave-assisted switching [157] is also a possibility. In any case, the inversion needs to be as complete as possible to minimize hysteresis effects. Tapered waveguides are advantageous to that effect [158]. In the worst case, an off-chip coil is needed to achieve the desired effect. Such coil-flipping schemes are used successfully for AMR magnetometers for more than two decades [159].

One point that can not be examined numerically is the presence of noise. Ignoring noise that originates from the electric and engineering side of the device, thermal noise from thermal magnons (see section 9.1) can still be a concern on the magnetic side.

Part V

Offset-free magnetometer based on ferromagnetic resonance

The magnetometer that has been presented in part IV employs some novel ideas for an interesting magnetometer design. There are, however, several shortcomings that would most likely prevent it from practical application:

- The voltages generated by the setup are very low, resulting in very low sensitivity.
- The amplitude of the standing wave, and hence the voltage, relies on high fabrication accuracy regarding antenna size and position.
- Most of the waveguide doesn't contribute anything to the resulting voltage, wasting material and space. The same is true for the alternative current-based setup.
- Fabrication of an array of perfectly parallel waveguides is difficult enough, fabrication of another array of parallel antennas adds another difficult step to fabrication.

An important observation is that a standing wave is nothing else than precessional motion, with variable amplitude. Also the phase is variable, but for a detection scheme based on spin pumping this does not matter. The most basic case of precessional motion is with constant amplitude, *i. e.* FMR. FMR would offer some solutions to the listed shortcomings: The achievable **voltage** should be **higher**, necessary fabrication accuracy is much lower, and material waste should be lower.

It might be argued that FMR does not constitute a magnon and therefore violates both the spirit and aim of this thesis. At first glance, this is a valid argument. Mathematically, it is not: In both a quantized (with ladder operators) as well as a continuum (with a harmonic wave function) picture, **FMR is a magnon**, just one with $\left\|\vec{k}\right\| = 0$. It is, after all, the limiting case for the dispersion relation.

The design presented here follows the concept of the previous one regarding spin pumping, anisotropy and signal generation, but switching to FMR.

For this design, sensitivity and linear range are explicitly computed. An analysis of the offset is provided. Since an external field is needed to switch between the two different magnetization configurations, deperming happens permanently; furthermore, hysteresis should be negligible for such a design.

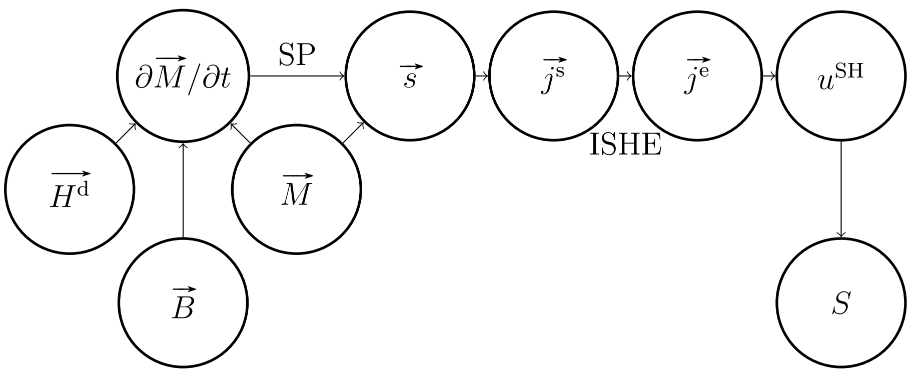

Figure 11.1: Modus of operation for the standing wave magnetometer. This is described in detail in section 11.1. The field to be measured $\vec{B}$ and the Oersted field $\vec{H}^{\mathrm{d}}$ of excitation antennas create a distinct precessional motion $\partial\vec{M}/\partial t$, which is translated into a voltage u by means of spin pumping and ISHE.

11.1 System Description and Modus of Operation

The considered structure is shown in figure 11.2. The setup is based on the work of Pardavi-Horvath *et al.* [160]. A nanoellipse, made out of permalloy (Py, Ni_4Fe) with dimensions of $(520 \times 250 \times 20)$ nm, forms the base. It is magnetized approximately longitudinally, *i.e.* $M_{\parallel}/M_S = m_x \approx \pm 1$. The magnetization is in longitudinal direction close to the centerline of the ellipse, while beginning to follow the curvature of the ellipse the closer it gets to the edges. Below it, a square slab of platinum with dimensions $(540 \times 540 \times 10)$ nm is placed. The driving field $\overrightarrow{H^{\mathrm{d}}}$, an Oersted field in application, is simulated by a homogeneous external field, as this is a sufficient approximation.

The application of an external field along the long axis of the ellipse (*i.e.* B_x) shifts the peak of the susceptibility in the frequency direction. The amplitude and rate of precession therefore change as a function of external field, acting as a measured quantity.

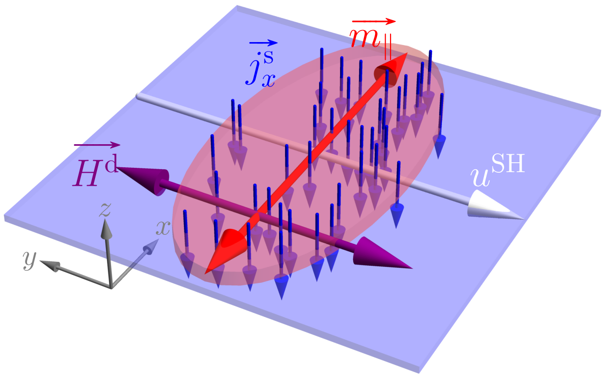

Figure 11.2: Schematic of the sensing structure. The Py nanoellipse of $(520 \times 250 \times 20)$ nm is in light red, the Pt slab of $(540 \times 540 \times 10)$ nm in light blue. The longitudinal (=equilibrium) component $\overrightarrow{m_\parallel}$ of the magnetization is pointed along the long axis. Precessional motion is excited in the ellipse by an oscillating homogeneous driving field $\overrightarrow{H^{\mathrm{d}}}$ along the short axis. The motion generates a (blue) spin DC $\widehat{j}^{\mathrm{s}}$ via spin pumping. The spin-Hall effect in the slab converts this into a charge DC $\overrightarrow{j^{\mathrm{SH}}}$, resulting in a (white) measurable voltage u^{SH}.

The major advantage of the FMR setup is that the device can be operated for large amplitudes, while still operating in the linear regime. For homogeneous precession, unwanted standing-wave contributions always emerge due to Suhl processes (section 9.3), such that care has to be taken when selecting the working frequency of the device.

Spin pumping creates a spin accumulation $\vec{s}$ inside of the nanoellipse that is then diffusing into the Pt slab. This spin accumulation creates a spin DC $\widehat{j}^{\mathrm{s}}$ into the slab, with a spin direction that is parallel to the long axis of the ellipse (*i.e.* j^{s}_{xz}). (It also creates a spin AC with an orthogonal spin direction (*i.e.* j^{s}_{yz}), but this is not important for the device.) This spin DC is then transformed into a charge DC parallel to the applied AC by **ISHE**. The voltage u^{SH} that results from this current is the signal of the sensor.

For the setup, a single ellipse is used. For a practical implementation, this number needs to be increased by three orders of magnitude, in order to amplify the signal. The magnetometer signal is then the sum of the individual ellipses' u^{SH}, by assuming a serial connection. Since precession inside the ellipses is highly elliptical, a suitable low-pass filter has to be applied to subdue those high-frequency oscillations. To achieve an offset-free transfer curve S, u^{SH} is compared for the magnetization of the waveguide in both directions along its longitudinal axis, *i.e.*

$$S = u^{\mathrm{SH}}\left[m_x = 1\right] + u^{\mathrm{SH}}\left[m_x = -1\right]. \tag{11.1}$$

Per the symmetry of the system, two signals with opposite sign are expected for $B_x = 0$ (due to s_x having the opposite sign), with the signals being identical but shifted by $2\, u^{\mathrm{SH}}\,[B_x = 0]$. Consequentially, the response is

$$\frac{\partial S}{\partial B_x} = 2\frac{\partial u^{\mathrm{SH}}}{\partial B_x}. \tag{11.2}$$

Such an additive measurement makes it possible to generate an **offset-free transfer curve** from a single device, with all possible deviations (fabrication and material parameters) being nullified by the symmetry. In practice, the nanoellipse's magnetization needs to be periodically (on a millisecond scale) inverted by short application of an external field to enable this differential measurement.

11.1.1 Analytical Magnetometer Response

The nonlinear derivation of subsection 6.3.2 can not be expressed analytically, hence numerical and experimental evaluation will be performed for the linear case, which is sufficient. Assuming homogeneous magnetization as an approximation, the magnetic susceptibility, and hence the shape of the FMR peak, is then given by equation (6.15), rewritten here as

$$\widehat{\chi} = \frac{B_{\mathrm{M}}}{\left(B_x + B_{\mathrm{M}}\left(N_{22} - N_{11}\right) - B_{\mathrm{f}}\right)\left(B_x + B_{\mathrm{M}}\left(N_{33} - N_{11}\right) - B_{\mathrm{f}}\right) + \left(\alpha\, B_{\mathrm{f}}\right)^2} \begin{pmatrix} B_x + B_{\mathrm{M}}\left(N_{33} - N_{11}\right) - B_{\mathrm{f}} & \alpha\, B_{\mathrm{f}} \\ -\alpha\, B_{\mathrm{f}} & B_x + B_{\mathrm{M}}\left(N_{22} - N_{11}\right) - B_{\mathrm{f}} \end{pmatrix}. \tag{11.3}$$

with $B_{\mathrm{M}} = \mu_0 M_{\mathrm{S}}$ and $B_{\mathrm{f}} = 2\pi f/\gamma_{\mathrm{e}}$. M_{S} and α are listed in table 11.1; B_x is the external field, assumed to be exclusively in x-direction. The shape of the off-diagonal components of the susceptibility is that of a Lorentz distribution.

An operational limit is immediately visible: the susceptibility is again not linearly depending on B_x, and so the magnetometer response is only approximately linear for **small external fields**.

The flat ellipse of the simulation can be approximated as a flat ellipsoid, essentially a **Stoner-Wohlfarth particle**. For such a case, the demagnetization factors can be computed analytically, as has been mentioned. In principle, all nine demagnetization factors can be computed numerically for the flat ellipse. This would needlessly make equation (11.3) more complicated, without changing the qualitative behavior.

Again,

$$M_p = \chi_{pq}\, H_q^{\mathrm{d}} \tag{11.4}$$

and

$$\frac{\mathrm{d}M_p}{\mathrm{d}t} = \chi_{pq} \frac{\mathrm{d}H_q^{\mathrm{d}}}{\mathrm{d}t}. \tag{11.5}$$

It is not possible to analytically solve the diffusion equation when including the coupling effects inside the ellipse. An approximation is possible when the ellipse is treated as an electric insulator and hence simply as a boundary condition for the diffusion equation in the slab, as has been shown in subsection 5.4.2. To enable this, the coupling effects have to be substituted by modified values for $\gamma_{\mathrm{e}} \to \gamma_{\mathrm{SP}}$ (this also applies to the definition of B_{f} above) and $\alpha \to \alpha_{\mathrm{SP}}$. Indeed, most of the simulations are conducted by using modified values instead of the full coupling, again due to the wrong demagnetization field (*e. f.* subsection 10.2.1). Assuming homogeneous precession, equation (5.11) can again be employed as an approximation, with $L = 10\,\mathrm{nm}$.

This spin accumulation creates a spin DC $\hat{j}^{\mathrm{s}}$ into the slab, with a spin direction that is parallel to the long axis of the ellipse (*i.e.* j^{s}_{xz}). (It also creates a spin AC with an orthogonal spin direction (*i.e.* j^{s}_{yz}), but this is not important for the device.) This spin DC is then transformed into a charge DC parallel to the applied AC by ISHE, equation (3.13), with the spin current equation (3.3) limited to diffusion:

$$j_y^{\mathrm{SH}} = 2\frac{e}{\mu_{\mathrm{B}}} D_0\, \Theta_{\mathrm{SH}}\, \frac{\partial s_x}{\partial z}. \tag{11.6}$$

Averaging over the current for the total height of the slab removes the coordinate dependence. Assuming a long enough slab (true in practice as it is a stripline), boundary effects can be ignored for analytical purposes and a simple Ohmian approximation made for the voltage u^{SH} that results from this current.

From the presented equations and arguments, the expected voltage can be approximated and, more importantly, the **response**

$$\frac{\partial u^{\mathrm{SH}}}{\partial B_x} \propto \frac{B_{\mathrm{f}}\left(2\left(B_x - B_{\mathrm{f}}\right) + B_{\mathrm{M}}\left(N_{22} + N_{33} - 2\,N_{11}\right)\right)}{\left(\left(B_{\mathrm{f}} - B_x + B_{\mathrm{M}}\left(N_{11} - N_{22}\right)\right)\left(B_{\mathrm{f}} - B_x + B_{\mathrm{M}}\left(N_{11} - N_{33}\right)\right) + \left(\alpha_{\mathrm{SP}}\,B_{\mathrm{f}}\right)^2\right)^2}, \tag{11.7}$$

where all the amassed material constants and system parameters have been factored out. The signal, as could be expected, again is roughly of square Lorentzian shape, hence the fits in the plots shown herein have all been performed with a Lorentzian distribution. The response is clearly not linear, as previously stated. This is only the case for small external fields.

11.2 Simulation Results

Table 11.1: Material parameters used.

Py ellipse			
saturation magnetization	M_S	860	kA/m
exchange coupling	A	81.1	MeV/m
electronic coupling	J	995	meV
electronic diffusion constant	D_0	10	cm²/s
conductivity	C_0	1	MS/m
spin-flip time	τ_{sf}	8	fs
Gilbert damping	α	0.01	
Pt slab			
electronic diffusion constant	D_0	50	cm²/s
conductivity	C_0	4.5	MS/m
spin-flip time	τ_{sf}	19.6	fs
spin-Hall angle	Θ_{SH}	0.04	

The material parameters that were used are listed in table 11.1. The spin diffusion, demagnetization, magnetic exchange, and the external driving field are computed. Again, the procedure from subsection 10.2.1 is applied here.

To find a suitable probing point, frequency and voltage spectra are computed for the system.

11.2.1 Energy spectra

To find the working frequency and assess the general behavior of the

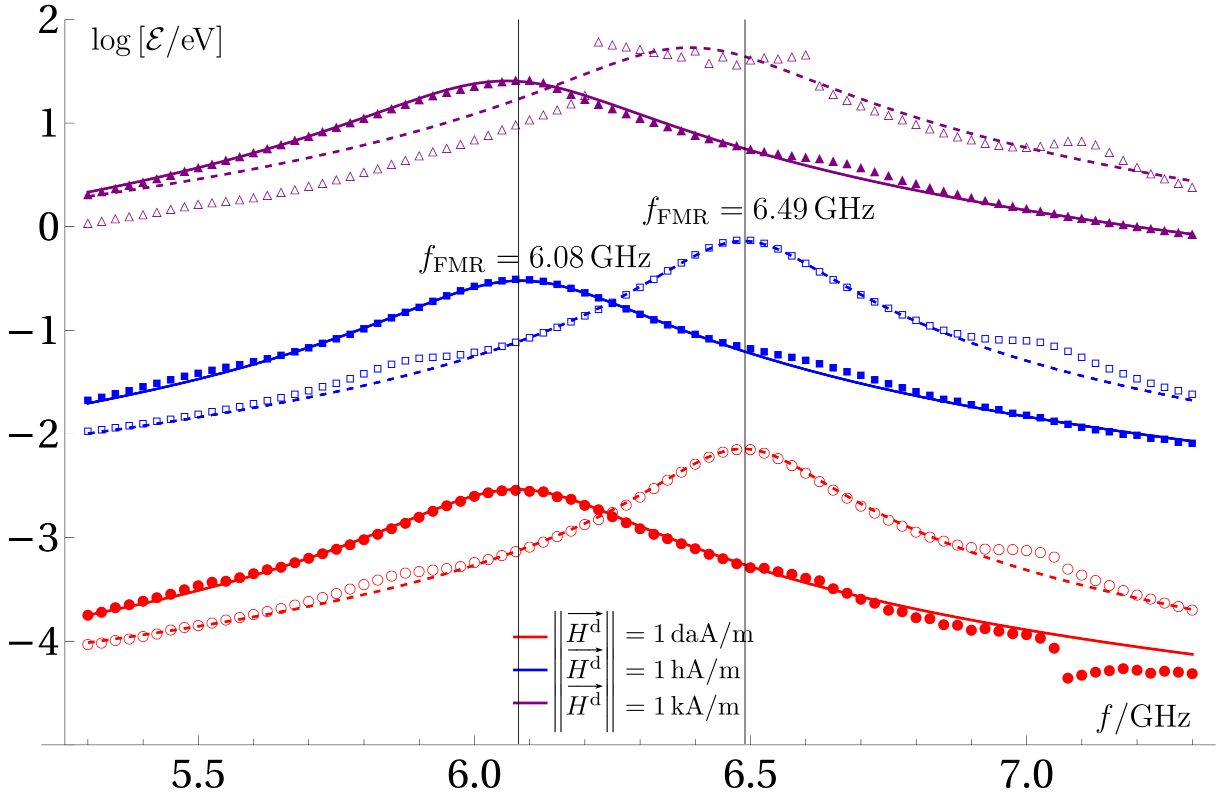

Figure 11.3: Energy spectra from the simulation system for three different driving field $\|\vec{H}^d\|$ strengths (colors), and for with spin torque (solid curves — fit and filled markers — computed values) and without spin torque (dashed curves and unfilled markers). Plotted is the sum of the exchange and demagnetization energy in the system. The values shown here are an average over 10 cycles. The frequency shift and amplitude loss is a consequence of spin pumping. For high driving field and without spin torque the peak already experiences domainization.

simulation system, a frequency sweep near the expected FMR frequency is performed. This is done in two different ways: With and without the spin-torque effects from the self-consistent spin pumping solver (note that the spin torque has been approximated by the method outlined in subsection 11.2.3). The results are shown in figure 11.3. Here, $\mathcal{E}$ is the sum of the exchange and demagnetization energy in the system. $\mathcal{E} \propto \left\|\overrightarrow{H_\mathrm{d}}\right\|^2$, as can be expected for linear behavior. To subdue the oscillation from elliptic precession, an average over the last 10 cycles is plotted. The FMR is located at 6.48 GHz without spin torque, and at 6.02 GHz with spin torque. The change in frequency originates purely from the effects of spin pumping. The peak amplitude without spin torque is markedly higher than with it. This is again a consequence of spin pumping. For the high driving field, the peaks notably deviate from their ideal form: Without spin torque, the damping and effective anisotropy in the system are too low to fully prohibit the formation of domains, whereas with spin torque the increased damping can subdue domainization and the non-linear change of the demagnetization field can subtly shift the peak to lower frequencies.

11.2.2 Nonlinear resonance

Revisiting section 6.3, an interesting thought arises. Mathematically, the hysteresis shown in figure 6.5 incorporates sections where the function is not continuous and exhibits infinite slope. This can of course not be observed in real systems. What is observed is a very high slope (although for very high excitations this is very difficult ro resolve [161]).

Since this very high slope should translate into a very high response, the question arises if it can be exploited. Can the hysteresis be traced to this section and stabilized; and what would happen if the field, *i. e.* $\overrightarrow{B_x}$, is then changed?

Unfortunately, as already evident from figure 11.3, this can not be reached for the tested setup. The domainization that is setting in for higher fields renders the analytical theory invalid. Since the bias field in the setup originates from the rather weak and spatially inhomogeneous uniaxial shape anisotropy, the analytical formula does not hold anymore. For high driving fields, the magnetization inside the nanoellipse becomes very inhomogeneous itself, up to the point where the system drops into the state of lowest energy, with two antiparallel domains in the ellipse.

11.2.3 Modified micromagnetical parameters

To enable the demagnetization-field correction, the modified parameters can be extracted from a self-consistent simulation and employed in a non-self-consistent computation to mimic the effects of the spin torque. Extraction is permitted since the modified parameters are in principle only a function of system structure and material (*c. f.* subsection 5.4.2). In actual simulation they are “almost” independent from additional parameters. This can be seen in figure 11.4. Even though the values are not strictly equal and constant, they are roughly so (this is also true for different driving field strength, not shown here). The values of $\gamma_\mathrm{SP} = 0.938\gamma_\mathrm{e}$ and $\alpha_\mathrm{SP} = 1.55\alpha$) will be used in further simulations.

It can be argued that the parameters are not constant in the nanoellipse but rather a field, dependent on the z-coordinate. This is indeed so. The point of this method is to

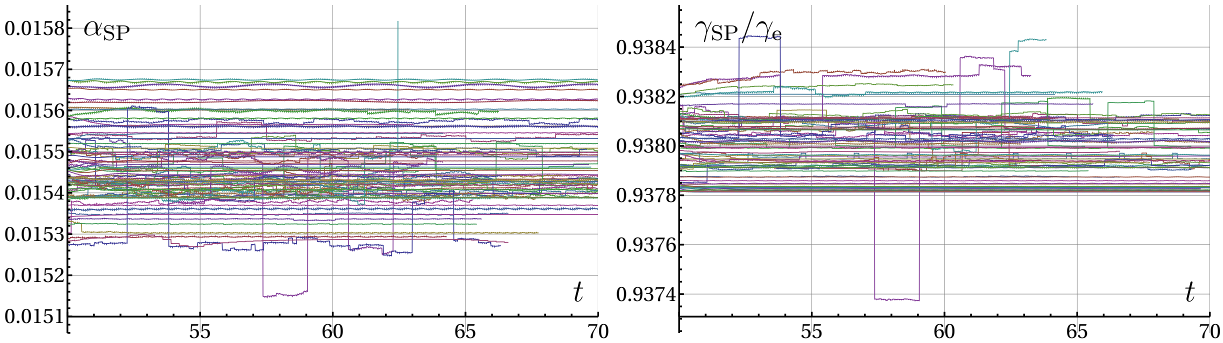

Figure 11.4: Modified micromagnetical parameters for a driving field of $\left\|\overrightarrow{H_d}\right\| = 1\,\mathrm{kA/m}$ over time. Each colored curve is another frequency from figure 11.3. The values are an average over the nanoellipse. All the values are contained in an interval. Some deviations from numerical inaccuracies are noticeable. Some of the curves end prematurely due to computation time limit.

ensure the correct average magnetodynamics (in regards to position of FMR), and not the correct pumped spin current. The voltage signal resulting from the computations will most likely be very different than a measured one anyway, since the material parameters are approximations.

11.2.4 Signal Output

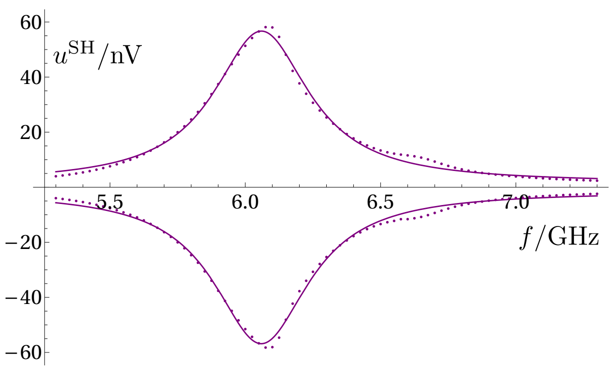

Figure 11.5: Voltage spectrum from the simulation system for $\left\|\overrightarrow{H^d}\right\| = 1\,\mathrm{kA/m}$, for both magnetization directions. The shown values are 4 ns-averages of the 250 MHz low-pass-filtered voltages. The symmetry is clearly visible.

The frequency spectrum for $\left\|\overrightarrow{H^d}\right\| = 1\,\mathrm{kA/m}$ is again shown in figure 11.5, but now with the spin-Hall voltage for both magnetization directions $m_x = \pm 1$. A low-pass filter of 250 MHz has been employed to subdue the oscillatory components (due to elliptical precession). As expected, the curves are each other's mirror image.

The largest response of the right flank is located at 6.2 GHz, which is selected as working frequency. Sweeping the external field B_x at this frequency, and combining the signals for both directions as per equation (10.1) yields the signal shown, among others, in figure 11.6. There, the computed signals for three different driving fields are shown. The response of the signal increases with driving field strength, but the linear range ΔB (calculated as per [29]) decreases doing so. Note that the linear range of the device is smaller than the strength of the driving field.

The case of $\left\|\overrightarrow{H^d}\right\| = 1\,\mathrm{kA/m}$ has the working frequency already close to domainization. A different frequency at the left flank of the peak could have been chosen for even higher response, but the onsetting domainization is enacting an upper limit on the response of a couple hundred nV/T.

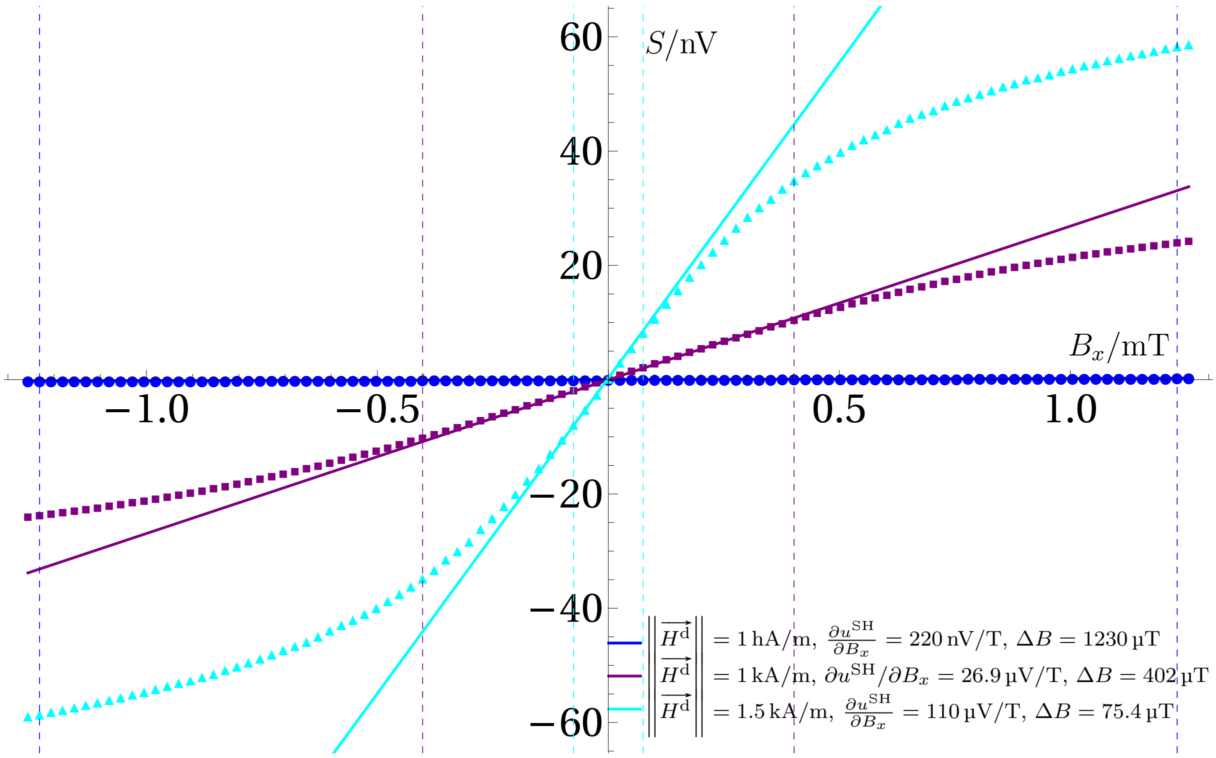

Figure 11.6: Signals from the simulation system for three different driving field $\left\|\overrightarrow{H^{\mathrm{d}}}\right\|$ strengths (colors). The shown values are 4 ns-averages of the 250 MHz low-pass-filtered voltages. The response is shown by the corresponding lines. Response and linear range are also noted in the legend.

11.2.5 Transversal field effects

To examine the effects of transversal fields, the same sweep as in subsection 11.2.4 is performed, but now with $B_i = \Delta B$, with i either being y or z, and the transversal component equal to the linear range of the sensor. The resulting key parameters are shown in table 11.2, in comparison to the values without the transversal components.

Table 11.2: Key parameters of the simulation system, comparing no transversal with transversal fields.

H_{d}	1 hA/m	1 kA/m	1.5 kA/m
	$\vec{B} = (B_x, 0, 0)^{\intercal}$		
$\frac{\partial u^{\mathrm{SH}}}{\partial B_x}/(\mathrm{\mu V/T})$	0.220	26.9	110
$O/\mathrm{\mu T}$	−27.1	−1.11	2.59
$\Delta B/\mathrm{\mu T}$	1230	402	75.4
	$\vec{B} = (B_x, \Delta H_{\mathrm{l}}, 0)^{\intercal}$		
$\frac{\partial u^{\mathrm{SH}}}{\partial B_x}/(\mathrm{\mu V/T})$	0.225	26.2	111
$O/\mathrm{\mu T}$	−24.5	−0.423	2.55
$\Delta B/\mathrm{\mu T}$	1010	503	75.4
	$\vec{B} = (B_x, 0, \Delta H_{\mathrm{l}})^{\intercal}$		
$\frac{\partial u^{\mathrm{SH}}}{\partial B_x}/(\mathrm{\mu V/T})$	0.222	26.9	110
$O/\mathrm{\mu T}$	−25.9	−1.05	2.47
$\Delta B/\mathrm{\mu T}$	1130	402	75.4

There is a noticeable difference between the two possible transversal directions, with the effects for the z-direction more subdued. There are two reasons for this: Firstly, the z-direction tilts the precession axis out of the plane of the flat ellipsoid, to which the demagnetization effects provide considerable resistance. And secondly, even though the precession axis is tilted, the component of $\vec{s}$ that is responsible for the resulting constant voltage (which is parallel to that axis) is still orthogonal to the direction where the voltage is measured (y). Both things are not true for the y-direction. In any case, a reduction of the response can be expected, but this is not reflected in the simulations.

Even though the offset should in principle be unchanged, the different symmetry of the mesh (see also the succeeding section) for the new precession axis means that there is a change.

If comparing the signal curves for fields with and without transversal components (*i. e.* $S^{\mathrm{t}} - S$), no functional behavior can be observed. Relative differences, however, are generally getting lower with the external field increasing towards the end of the linear range and are higher for transversal field in the y-direction. This is obviously what one would expect.

11.2.6 Numerical errors

Compared to part IV, the offset is rather high; especially when considering the much longer simulation time and complicated simulation setup with multiple re-starts of the integrator there.

The elimination of the offset relies on the symmetry of the system, specifically rotation symmetry. Geometrically, the system is obviously symmetrical. But after discretizing the system, this is in general no longer true. Unless it is specifically built so, the used meshing algorithm (any meshing algorithm, in fact) does not build a symmetrical mesh.

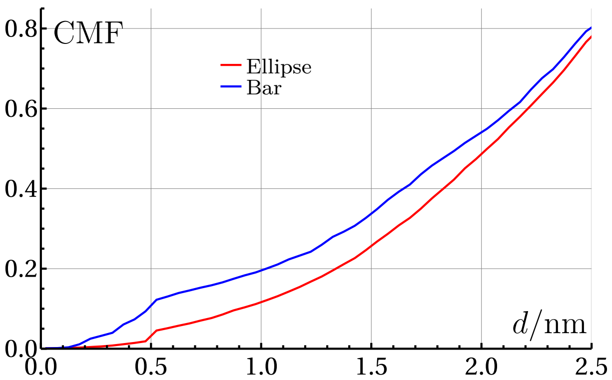

Figure 11.7: Comparison of the CMF of the meshed simulation system and a system where the ellipse has been replaced with a bar of equal area and aspect ratio. d is the distance from a vertex in the unrotated mesh to the nearest vertex in the rotated mesh.

To get a measure of the meshes asymmetry, for every vertex in the unrotated mesh, the closest vertex in the rotated mesh is found. The determined distances are then collected into a histogram, and plotted as a cumulative mass function (CMF), *i. e.* the cumulative normalized histogram. Additionally, the same procedure was performed for a mesh where the ellipse is replaced by a bar with the same area and aspect ratio. The comparison is shown in figure 11.7. As the meshes have been created with a tetrahedron size of $\approx 5\,\mathrm{nm}$, the majority of distances are within half of it. It can be seen that both structures have similar behavior, but the bar system generally has lower distances. This suggests that a cuboid system, as in part IV, provides lower offset due to higher symmetry.

In the case of transversal fields, this symmetry analysis is no longer applicable as the ground state of the system is not rotationally symmetric.

11.3 Realization

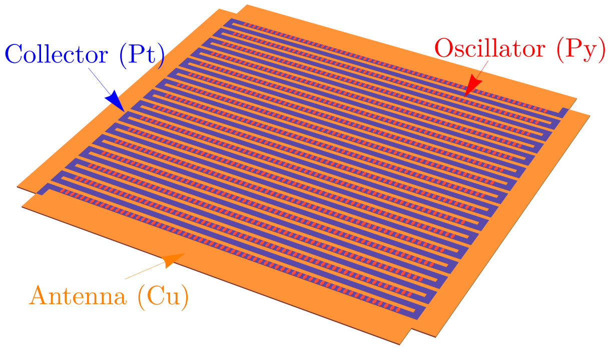

Figure 11.8: Proposed realization of the concept. 1008 nanoellipses are arranged in a (450×1800) nm lattice and connected by a 540 nm-wide stripline that provides the voltage. The whole setup is positioned atop a Cu cross structure that provides both the driving field and the field for magnetization reversal.

For the application case, it is necessary to scale the simulation system up, or rather employ a large amount of the simulated nanoellipses in serial fashion. The simple serial version is shown in figure 11.8. This device consists of 1008 nanoellipses in a 63×16 configuration with (450×1800) nm separation; the ellipses cover a roughly square area of (28.15×27.52) µm. The ellipses are fully connected by a Pt stripline of 540 nm width. Due to polarity, every other stripline is vacant. Naively, one can expect a signal 1008-times as large as for a single nanoellipse, with the response also increasing the same. The whole setup is placed atop a cross structure made out of copper, that acts both as a provider of driving field as well as means for magnetization reversal. Applying AC orthogonally to the striplines creates the driving field, applying DC parallel to them reverses the magnetization. By combining a DC in both directions the **Stoner-Wohlfarth astroid** [128] can be exploited to reduce the necessary switching current.

Assessment and Conclusion

The aim of this work was to design and evaluate a magnetometer on the basis of spin waves, especially a variant that provides offset-free behavior, ideally from a single device.

Within that scope, the project was a success. Two devices have been presented and numerically examined. Within the limits of numerical accuracy, both of them were free from offset.

But as has been stated, Hall-effect magnetometers are in principle already offset-free by their physical concept but still retain a finite offset after cancellation measures are taken. It is thus evident that the offset is originating from fabrication; something which can not be properly modeled in numerics, especially in micromagnetics. The utility of the presented devices hence relies on their fabrication as well, and will suffer from the same problems.

This turns one of the advantages of the presented designs into a disadvantage. The spinning-current setup of Hall-effect magnetometers contains four independent measurements that are used for offset cancellations. The presented designs can only have two independent measurements; it can be expected that the remaining offset will be much larger than for Hall-effect devices, especially since the two measurements have considerable offsets by themselves.

The same can not be said for magnetoresistive magnetometers, however. As already stated before, they possess considerable offset even after the cancellation setup. The presented devices should be competitive with them.

The low sensitivity provided by spin pumping is much lower than anything available commercially. This can be a critical disadvantage for the presented devices. On the other hand, relying on spin pumping means that no current is applied to the structure, which should improve device lifetime and heat generation, compared to magnetoresistive devices. This includes spin-torque oscillator devices which are similar to the presented FMR-based magnetometer, but rely on GMR for readout.

All things considered, the presented devices and concepts are not able to challenge Hall-effect devices but should be able to compete with magnetoresistive ones for certain niche applications. It will take further work, *i. e.* fabrication of a prototype and testing, to obtain real-world data.

Bibliography

[1] Miguel Alcubierre. "The warp drive: hyper-fast travel within general relativity". In: *Classical and Quantum Gravity* 11.5 (May 1994), pp. L73–L77. ISSN: 1361-6382. DOI: 10.1088/0264-9381/11/5/001.

[2] Chris Van Den Broeck. "A 'warp drive' with more reasonable total energy requirements". In: *Classical and Quantum Gravity* 16.12 (Nov. 1999), pp. 3973–3979. ISSN: 1361-6382. DOI: 10.1088/0264-9381/16/12/314.

[3] Charles H. Bennett et al. "Teleporting an unknown quantum state via dual classical and Einstein-Podolsky-Rosen channels". In: *Physical Review Letters* 70.13 (Mar. 1993), pp. 1895–1899. ISSN: 0031-9007. DOI: 10.1103/physrevlett.70.1895.

[4] Dik Bouwmeester et al. "Experimental quantum teleportation". In: *Nature* 390.6660 (Dec. 1997), pp. 575–579. ISSN: 1476-4687. DOI: 10.1038/37539.

[5] Francesca Casoli and Gaspare Varvaro, eds. *Ultrahigh-density magnetic recording. Storage materials and media designs*. Includes bibliographical references. [Singapore]: Pan Stanford Publishing, 2016. 1 p. ISBN: 9789814669597.

[6] Alois Tipek and Pavel Ripka, eds. *Modern sensors handbook*. Instrumentation and measurement series. Includes bibliographical references and index. Newport Beach, CA: ISTE USA, 2007. 1518 pp. ISBN: 9781280847813.

[7] Pavel Ripka. *Magnetic Sensors and Magnetometers*. Second. Norwood: Artech House, 2021. ISBN: 9781630817428.

[8] I. R. McFadyen, E. E. Fullerton, and M. J. Carey. "State-of-the-Art Magnetic Hard Disk Drives". In: *MRS Bulletin* 31.5 (May 2006), pp. 379–383. DOI: 10.1557/mrs2006.97.

[9] John David Jackson. *Classical Electrodynamics*. Third Edition. John Wiley & Sons Inc, July 27, 1998. 832 pp. ISBN: 047130932X.

[10] R. C. Jaklevic et al. "Quantum Interference Effects in Josephson Tunneling". In: *Physical Review Letters* 12.7 (Feb. 1964), pp. 159–160. DOI: 10.1103/physrevlett.12.159.

[11] B. D. Josephson. "Possible new effects in superconductive tunnelling". In: *Physics Letters* 1.7 (July 1962), pp. 251–253. ISSN: 0031-9163. DOI: 10.1016/0031-9163(62)91369-0.

[12] Michael Faraday. "On the magnetization of light and the illumination of magnetic lines of force". In: *Philosophical Transactions of the Royal Society of London* 136 (Dec. 1846), pp. 1–20. ISSN: 2053-9223. DOI: 10.1098/rstl.1846.0001.

[13] John Kerr. "XLIII. On rotation of the plane of polarization by reflection from the pole of a magnet". In: *The London, Edinburgh, and Dublin Philosophical Magazine and Journal of Science* 3.19 (May 1877), pp. 321–343. ISSN: 1941-5990. DOI: 10.1080/14786447708639245.

[14] R. S. Popovic. *Hall Effect Devices*. Boca Raton: CRC Press, Dec. 2003. DOI: 10.1201/noe0750308557.

[15] E. H. Hall. "On a New Action of the Magnet on Electric Currents". In: *American Journal of Mathematics* 2.3 (Sept. 1879), p. 287. DOI: 10.2307/2369245.

[16] William Thomson. "XIX. On the electro-dynamic qualities of metals:—Effects of magnetization on the electric conductivity of nickel and of iron". In: *Proceedings of the Royal Society of London* 8 (Dec. 1857), pp. 546–550. DOI: 10.1098/rspl.1856.0144.

[17] R. Hunt. "A magnetoresistive readout transducer". In: *IEEE Transactions on Magnetics* 7.1 (Mar. 1971), pp. 150–154. DOI: 10.1109/tmag.1971.1067019.

[18] M. N. Baibich et al. "Giant Magnetoresistance of (001)Fe/(001)Cr Magnetic Superlattices". In: *Physical Review Letters* 61.21 (Nov. 1988), pp. 2472–2475. DOI: 10.1103/physrevlett.61.2472.

[19] G. Binasch et al. "Enhanced magnetoresistance in layered magnetic structures with antiferromagnetic interlayer exchange". In: *Physical Review B* 39.7 (Mar. 1989), pp. 4828–4830. DOI: 10.1103/physrevb.39.4828.

[20] M. Julliere. "Tunneling between ferromagnetic films". In: *Physics Letters A* 54.3 (Sept. 1975), pp. 225–226. DOI: 10.1016/0375-9601(75)90174-7.

[21] John Slonczewski. "Magnetic Bubble Tunnel Detector". In: *IBM Technical Disclosure Bulletin* 19.6 (Nov. 1976), pp. 2328–2330.

[22] Rolf Slatter. "Low power miniaturized tunnel magnetoresistive (TMR) sensors for Industry 4.0 applications". In: *Micro-Nano-Integration; 7th GMM-Workshop*. Dortmund: VDE, 2018, pp. 1–6. URL: https://ieeexplore-ieee-org/abstract/document/8580243.

[23] P. M. Braganca et al. "Nanoscale magnetic field detection using a spin torque oscillator". In: *Nanotechnology* 21.23 (May 2010), p. 235202. DOI: 10.1088/0957-4484/21/23/235202.

[24] Gopalakrishnan Balasubramanian et al. "Ultralong spin coherence time in isotopically engineered diamond". In: *Nature Materials* 8.5 (Apr. 2009), pp. 383–387. DOI: 10.1038/nmat2420.

[25] Mitsuteru Inoue et al. "Investigating the use of magnonic crystals as extremely sensitive magnetic field sensors at room temperature". In: *Applied Physics Letters* 98.13 (Mar. 2011), p. 132511. DOI: 10.1063/1.3567940.

[26] O. Haas, B. Dufay, and S. Saez. "Development of a Magnonic-Based Magnetic Sensor: Comparison of Two Different Implementations With YIG Material". In: *IEEE Transactions on Magnetics* 59.2 (Feb. 2023), pp. 1–6. DOI: 10.1109/tmag.2022.3215274.

[27] Y. Martin and H. K. Wickramasinghe. "Magnetic imaging by '"force microscopy"' with 1000 Å resolution". In: *Applied Physics Letters* 50.20 (May 1987), pp. 1455–1457. ISSN: 1077-3118. DOI: 10.1063/1.97800.

[28] P. Ripka. "Magnetic Sensors: Principles and Applications". In: *Encyclopedia of Materials: Science and Technology*. Elsevier, 2007, pp. 1–11. DOI: 10.1016/b978-008043152-9.02158-8.

[29] Dieter Suess et al. "Topologically protected vortex structures for low-noise magnetic sensors with high linear range". In: *Nature Electronics* 1.6 (June 2018), pp. 362–370. DOI: 10.1038/s41928-018-0084-2.

[30] Kannan M. Krishnan. *Fundamentals and Applications of Magnetic Materials*. Oxford University Press, Aug. 18, 2016. 816 pp. ISBN: 0199570442.

[31] Vyacheslav Tuzlukov. *Signal Processing Noise*. Taylor & Francis Group, 2002. ISBN: 9781420041118.

[32] Eric W. Weisstein, ed. *MathWorld*. Wolfram Research. May 2, 2023. URL: https://mathworld.wolfram.com/.

[33] Herbert Weitensfelder et al. "Comparison of Sensitivity and Low-Frequency Noise Contributions in Giant-Magnetoresistive and Tunneling-Magnetoresistive Spin-Valve Sensors with a Vortex-State Free Layer". In: *Physical Review Applied* 10.5 (Nov. 2018), p. 054056. DOI: 10.1103/physrevapplied.10.054056.

[34] María Dolores Cubells-Beltran et al. "Full Wheatstone Bridge Spin-Valve Based Sensors for IC Currents Monitoring". In: *IEEE Sensors Journal* 9.12 (Dec. 2009), pp. 1756–1762. DOI: 10.1109/jsen.2009.2030880.

[35] Ricardo Ferreira et al. "2-Axis Magnetometers Based on Full Wheatstone Bridges Incorporating Magnetic Tunnel Junctions Connected in Series". In: *IEEE Transactions on Magnetics* 48.11 (Nov. 2012), pp. 4107–4110. DOI: 10.1109/tmag.2012.2202381.

[36] P. J. A. Munter. "A low-offset spinning-current hall plate". In: *Sensors and Actuators A: Physical* 22.1-3 (June 1990), pp. 743–746. DOI: 10.1016/0924-4247(89)80069-x.

[37] Maria-Alexandra Paun, Jean-Michel Sallese, and Maher Kayal. "Offset and drift analysis of the Hall effect sensors". In: *Digest Journal of Nanomaterials and Biostructures* 7.3 (2012), pp. 883–891. ISSN: 1842-3582.

[38] *CT100 Datasheet. 1D Linear Sensor*. Version 2.0. Crocus Technology. Aug. 2021. 15 pp. URL: https://crocus-technology.com/wp-content/uploads/2021/09/CT100-Data-Sheet-Rev2.0.pdf.

[39] *CT130 Datasheet. XtremeSense Z-Axis TMR Analog Sensor*. Version 0.41. Crocus Technology. 2023. 9 pp. URL: https://crocus-technology.com/datasheets/CT130%20Data%20Sheet.pdf.

[40] F. Bloch. "Zur Theorie des Ferromagnetismus". In: *Zeitschrift für Physik* 61.3–4 (Mar. 1930), pp. 206–219. ISSN: 1434-601X. DOI: 10.1007/bf01339661.

[41] T. Holstein and H. Primakoff. "Field Dependence of the Intrinsic Domain Magnetization of a Ferromagnet". In: *Physical Review* 58.12 (Dec. 1940), pp. 1098–1113. DOI: 10.1103/physrev.58.1098.

[42] C. Kittel. "Interaction of Spin Waves and Ultrasonic Waves in Ferromagnetic Crystals". In: *Physical Review* 110.4 (May 1958), pp. 836–841. ISSN: 0031-899X. DOI: 10.1103/physrev.110.836.

[43] Andrii V. Chumak, Alexander A. Serga, and Burkard Hillebrands. "Magnon transistor for all-magnon data processing". In: *Nature Communications* 5.1 (Aug. 2014). ISSN: 2041-1723. DOI: 10.1038/ncomms5700.

[44] Anjan Barman et al. "The 2021 Magnonics Roadmap". In: *Journal of Physics: Condensed Matter* 33.41 (Aug. 2021), p. 413001. DOI: 10.1088/1361-648x/abec1a.

[45] A. V. Chumak et al. "Advances in Magnetics Roadmap on Spin-Wave Computing". In: *IEEE Transactions on Magnetics* 58.6 (June 2022), pp. 1–72. DOI: 10.1109/tmag.2022.3149664.

[46] Ph. Talbot, A. Fessant, and J. Gieraltowski. "Electromagnetic Sensors Based on Magnonic Crystals for Applications in the Fields of Biomedical and NDT". In: *Procedia Engineering* 120 (2015), pp. 1241–1244. DOI: 10.1016/j.proeng.2015.08.839.

[47] P. J. Metaxas et al. "Sensing magnetic nanoparticles using nano-confined ferromagnetic resonances in a magnonic crystal". In: *Applied Physics Letters* 106.23 (June 2015), p. 232406. DOI: 10.1063/1.4922392.

[48] Y. Kajiwara et al. "Transmission of electrical signals by spin-wave interconversion in a magnetic insulator". In: *Nature* 464.7286 (Mar. 2010), pp. 262–266. DOI: 10.1038/nature08876.

[49] C. W. Sandweg et al. "Spin Pumping by Parametrically Excited Exchange Magnons". In: *Physical Review Letters* 106.21 (May 2011), p. 216601. DOI: 10.1103/physrevlett.106.216601.

[50] A. V. Chumak et al. "Direct detection of magnon spin transport by the inverse spin Hall effect". In: *Applied Physics Letters* 100.8 (Feb. 2012), p. 082405. DOI: 10.1063/1.3689787.

[51] Claas Abert et al. "magnum.fe: A micromagnetic finite-element simulation code based on FEniCS". In: *Journal of Magnetism and Magnetic Materials* 345 (Nov. 2013), pp. 29–35. DOI: 10.1016/j.jmmm.2013.05.051.

[52] D. A. Ham et al. *Firedrake user manual*. Tech. rep. 2023. DOI: 10.25561/104839.

[53] Satish Balay et al. *PETSc Web page*. https://petsc.org/. 2023. URL: https://petsc.org/.

[54] Lisandro D. Dalcin et al. "Parallel distributed computing using Python". In: *Advances in Water Resources* 34.9 (Sept. 2011), pp. 1124–1139. ISSN: 0309-1708. DOI: 10.1016/j.advwatres.2011.04.013.

[55] Alan C. Hindmarsh et al. "SUNDIALS". In: *ACM Transactions on Mathematical Software (TOMS)* 31.3 (Sept. 2005), pp. 363–396. DOI: 10.1145/1089014.1089020.

[56] Christophe Geuzaine and Jean-François Remacle. "Gmsh: A 3-D finite element mesh generator with built-in pre- and post-processing facilities". In: *International Journal for Numerical Methods in Engineering* 79.11 (May 2009), pp. 1309–1331. ISSN: 1097-0207. DOI: 10.1002/nme.2579.

[57] Andrii Chumak and Vincent Vlaminck. "MagFunc. Non-Reciprocal 3D Architectures for Magnonic Functionalities". Grant Proposal.

[58] A. Einstein. "Die Grundlage der allgemeinen Relativitätstheorie". In: *Annalen der Physik* 354.7 (1916), pp. 769–822. DOI: 10.1002/andp.19163540702.

[59] P. A. M. Dirac. “A new notation for quantum mechanics”. In: *Mathematical Proceedings of the Cambridge Philosophical Society* 35.3 (July 1939), pp. 416–418. DOI: 10.1017/s0305004100021162.

[60] Markus Gattringer. “Field-free SOT switching via repolarization of spin accumulation”. MA thesis. Universität Wien, Aug. 4, 2020. 79 pp.

[61] W. F. Brown jr. *Micromagnetics*. Interscience Tracts on Physics and Astronomy 18. John Wiley & Sons, 1963.

[62] Nigel Goldenfeld. *Lectures On Phase Transitions And The Renormalization Group*. Taylor & Francis Inc, June 30, 1972. 420 pp. ISBN: 0201554097.

[63] A. Landé. “Über den anomalen Zeemaneffekt (Teil I)”. In: *Zeitschrift für Physik* 5.4 (July 1921), pp. 231–241. DOI: 10.1007/bf01335014.

[64] A. Landé. “Über den anomalen Zeemaneflekt (II. Teil)”. In: *Zeitschrift für Physik* 7.1 (Dec. 1921), pp. 398–405. DOI: 10.1007/bf01332807.

[65] M. C. Hickey and J. S. Moodera. “Origin of Intrinsic Gilbert Damping”. In: *Physical Review Letters* 102.13 (Mar. 2009), p. 137601. DOI: 10.1103/physrevlett.102.137601.

[66] V.M. Edelstein. “Spin polarization of conduction electrons induced by electric current in two-dimensional asymmetric electron systems”. In: *Solid State Communications* 73.3 (Jan. 1990), pp. 233–235. DOI: 10.1016/0038-1098(90)90963-c.

[67] G. Dresselhaus. “Spin-Orbit Coupling Effects in Zinc Blende Structures”. In: *Physical Review* 100.2 (Oct. 1955), pp. 580–586. DOI: 10.1103/physrev.100.580.

[68] L. D. Landau and E. V. Lifshits. “On the Theory of the Dispersion of Magnetic Permeability in Ferromagnetic Bodies”. In: *Physikalische Zeitschrift der Sowjetunion* 8 (1935), pp. 153–169.

[69] T. L. Gilbert. “Classics in Magnetics A Phenomenological Theory of Damping in Ferromagnetic Materials”. In: *IEEE Transactions on Magnetics* 40.6 (Nov. 2004), pp. 3443–3449. DOI: 10.1109/tmag.2004.836740.

[70] P. Zeeman. “The Effect of Magnetisation on the Nature of Light Emitted by a Substance”. In: *Nature* 55.1424 (Feb. 1897), pp. 347–347. DOI: 10.1038/055347a0.

[71] Hans Christian Ørsted. “Experiments on the Effect of a Current of Electricity on the Magnetic Needle”. In: *Annals of Philosophy* 16 (1820). Ed. by Thomas Thomson, pp. 273–276.

[72] W. Heisenberg. “Zur Theorie des Ferromagnetismus”. In: *Zeitschrift für Physik* 49.9-10 (Sept. 1928), pp. 619–636. DOI: 10.1007/bf01328601.

[73] Pierre Weiss. “L’hypothèse du champ moléculaire et la propriété ferromagnétique”. In: *Journal de Physique Théorique et Appliquée* 6.1 (1907), pp. 661–690. DOI: 10.1051/jphystap:019070060066100.

[74] W. Pauli. “Über den Zusammenhang des Abschlusses der Elektronengruppen im Atom mit der Komplexstruktur der Spektren”. In: *Zeitschrift für Physik* 31.1 (Feb. 1925), pp. 765–783. DOI: 10.1007/bf02980631.

[75] J. H. Van Vleck. *The Theory of Electric and Magnetic Susceptibilities*. Oxford: Clarendon Press, 1932. ISBN: 978-0198512431. ark: 13960/t6qz23d7c. URL: https://archive.org/details/theoryofelectric031070mbp/page/n333/mode/2up.

[76] J. C. Slater. “Cohesion in Monovalent Metals”. In: *Physical Review* 35.5 (Mar. 1930), pp. 509–529. DOI: 10.1103/physrev.35.509.

[77] Sergio M. Rezende. *Fundamentals of Magnonics*. Lecture Notes in Physics 969. Springer, 2020. 375 pp. ISBN: 9783030413163.

[78] N. F. Mott. “The electrical conductivity of transition metals”. In: *Proceedings of the Royal Society of London. Series A - Mathematical and Physical Sciences* 153.880 (Feb. 1936), pp. 699–717. DOI: 10.1098/rspa.1936.0031.

[79] E. Y. Tsymbal and D. G. Pettifor. “Perspectives of giant magnetoresistance”. In: *Solid State Physics*. Elsevier, 2001, pp. 113–237. DOI: 10.1016/s0081-1947(01)80019-9.

[80] P. C. van Son, H. van Kempen, and P. Wyder. “Boundary Resistance of the Ferromagnetic-Nonferromagnetic Metal Interface”. In: *Physical Review Letters* 58.21 (May 1987), pp. 2271–2273. DOI: 10.1103/physrevlett.58.2271.

[81] Ludwig Boltzmann. “Weitere Studien über das Wärmegleichgewicht unter Gasmolekülen”. In: *Kinetische Theorie II*. Vieweg+Teubner Verlag, 1970, pp. 115–225. DOI: 10.1007/978-3-322-84986-1_3.

[82] S. Zhang, P. M. Levy, and A. Fert. “Mechanisms of Spin-Polarized Current-Driven Magnetization Switching”. In: *Physical Review Letters* 88.23 (May 2002). DOI: 10.1103/physrevlett.88.236601.

[83] A. Einstein. “Über die von der molekularkinetischen Theorie der Wärme geforderte Bewegung von in ruhenden Flüssigkeiten suspendierten Teilchen”. In: *Annalen der Physik* 322.8 (1905), pp. 549–560. DOI: 10.1002/andp.19053220806.

[84] Claas Abert et al. “A self-consistent spin-diffusion model for micromagnetics”. In: *Scientific Reports* 6.1 (Dec. 2016). DOI: 10.1038/s41598-016-0019-y.

[85] Michele Ruggeri. “Coupling and numerical integration of the Landau-Lifshitz-Gilbert equation”. PhD thesis. Technische Universität Wien, Oct. 25, 2016. 138 pp. URL: https://publik.tuwien.ac.at/files/publik_252806.pdf.

[86] Robert Karplus and J. M. Luttinger. “Hall Effect in Ferromagnetics”. In: *Physical Review* 95.5 (Sept. 1954), pp. 1154–1160. DOI: 10.1103/physrev.95.1154.

[87] Y. K. Kato. “Observation of the Spin Hall Effect in Semiconductors”. In: *Science* 306.5703 (Dec. 2004), pp. 1910–1913. DOI: 10.1126/science.1105514.

[88] M. I. Dyakonov. “Magnetoresistance due to Edge Spin Accumulation”. In: *Physical Review Letters* 99.12 (Sept. 2007). DOI: 10.1103/physrevlett.99.126601.

[89] Lars Onsager. “Reciprocal Relations in Irreversible Processes. I.” In: *Physical Review* 37.4 (Feb. 1931), pp. 405–426. DOI: 10.1103/physrev.37.405.

[90] E. Saitoh et al. “Conversion of spin current into charge current at room temperature: Inverse spin-Hall effect”. In: *Applied Physics Letters* 88.18 (May 2006), p. 182509. DOI: 10.1063/1.2199473.

[91] Georges Voronoi. “Nouvelles applications des paramètres continus à la théorie des formes quadratiques. Premier mémoire. Sur quelques propriétés des formes quadratiques positives parfaites.” In: *Journal für die reine und angewandte Mathematik (Crelles Journal)* 1908.133 (Jan. 1908), pp. 97–102. DOI: 10.1515/crll.1908.133.97.

[92] D. Suess et al. “Accurate finite-difference micromagnetics of magnets including RKKY interaction: Analytical solution and comparison to standard micromagnetic codes”. In: *Physical Review B* 107.10 (Mar. 2023), p. 104424. DOI: 10.1103/physrevb.107.104424.

[93] Claes Johnson. *Numerical Solution of Partial Differential Equations by the Finite Element Method*. DOVER PUBN INC, Jan. 1, 2009. 278 pp. ISBN: 048646900X.

[94] Joachim Schöberl. “NETGEN An advancing front 2D/3D-mesh generator based on abstract rules”. In: *Computing and Visualization in Science* 1.1 (July 1997), pp. 41–52. DOI: 10.1007/s007910050004.

[95] Walter Ritz. “Über eine neue Methode zur Lösung gewisser Variationsprobleme der mathematischen Physik.” In: *Journal für die reine und angewandte Mathematik (Crelles Journal)* 1909.135 (Jan. 1909), pp. 1–61. DOI: 10.1515/crll.1909.135.1.

[96] Carlos J. Garcia-Cervera and Xiao-Ping Wang. “Spin-polarized transport: Existence of weak solutions”. In: *Discrete & Continuous Dynamical Systems - B* 7.1 (2007), pp. 87–100. DOI: 10.3934/dcdsb.2007.7.87.

[97] William H. Press et al. *Numerical Recipes*. Cambridge University Pr., Sept. 6, 2007. 1248 pp. ISBN: 0521880688.

[98] D.R. Fredkin and T.R. Koehler. “Hybrid method for computing demagnetizing fields”. In: *IEEE Transactions on Magnetics* 26.2 (Mar. 1990), pp. 415–417. DOI: 10.1109/20.106342.

[99] Ivar Stakgold. *Boundary Value Problems of Mathematical Physics*. Vol. 2. 2 vols. MacMillan Series in Advanced Mathematics and Theoretical Physics. New York: The MacMillan Company, 1968. 408 pp.

[100] W. Hackbusch, B. Khoromskij, and S. A. Sauter. “On H 2-Matrices”. In: *Lectures on Applied Mathematics*. Springer Berlin Heidelberg, 2000, pp. 9–29. ISBN: 9783642597091. DOI: 10.1007/978-3-642-59709-1_2.

[101] Ivan Cimrák. “A Survey on the numerics and computations for the Landau-Lifshitz equation of micromagnetism”. In: *Archives of Computational Methods in Engineering* 15.3 (Sept. 2007), pp. 1–37. DOI: 10.1007/bf03024947.

[102] Claas Abert. “Micromagnetics and spintronics: models and numerical methods”. In: *The European Physical Journal B* 92.6 (June 2019). DOI: 10.1140/epjb/e2019-90599-6.

[103] E. Fehlberg. “Klassische Runge-Kutta-Formeln fünfter und siebenter Ordnung mit Schrittweiten-Kontrolle”. In: *Computing* 4.2 (June 1969), pp. 93–106. DOI: 10.1007/bf02234758.

[104] C. F. Curtiss and J. O. Hirschfelder. “Integration of Stiff Equations”. In: *Proceedings of the National Academy of Sciences of the United States of America* 38.3 (1952), pp. 235–243. ISSN: 00278424. URL: http://www.jstor.org/stable/88864.

[105] D. Suess et al. “Time resolved micromagnetics using a preconditioned time integration method”. In: *Journal of Magnetism and Magnetic Materials* 248.2 (July 2002), pp. 298–311. DOI: 10.1016/s0304-8853(02)00341-4.

[106] Thomas Simpson. “A new Method for the Solution of Equations in Numbers”. In: *Essays on several Curious and Useful Subjects In Speculative and Mix’d Mathematicks. Illustrated by a Variety of Examples*. London: J. Nourse, 1740, pp. 81–86.

[107] A. Krylov. “Über die numerische Auflösung einer Gleichung, durch die in technischen Fragen die Frequenz kleiner Schwingungen bestimmt ist.” In: *Bulletin de l’Académie des Sciences de l’URSS. VII. Série* 1931.4 (1931), pp. 491–539. URL: `http://www.mathnet.ru/links/f85608aecde5fea66526cf5b1da10a12/im5215.pdf`.

[108] M. R. Hestenes and E. Stiefel. “Methods of conjugate gradients for solving linear systems”. In: *Journal of Research of the National Bureau of Standards* 49.6 (Dec. 1952), p. 409. DOI: `10.6028/jres.049.044`.

[109] Markus Gattringer et al. “Micromagnetically integrated numerical model of spin pumping based on spin diffusion”. In: *Physical Review B* 106.2 (July 2022), p. 024417. DOI: `10.1103/physrevb.106.024417`.

[110] A. Brataas et al. *Spin pumping and spin transfer*. Oxford University Press, Dec. 2017. DOI: `10.1093/oso/9780198787075.003.0008`.

[111] Yaroslav Tserkovnyak, Arne Brataas, and Gerrit E. W. Bauer. “Enhanced Gilbert Damping in Thin Ferromagnetic Films”. In: *Physical Review Letters* 88.11 (Feb. 2002), p. 117601. DOI: `10.1103/physrevlett.88.117601`.

[112] K. Ando et al. “Inverse spin-Hall effect induced by spin pumping in metallic system”. In: *Journal of Applied Physics* 109.10 (May 2011), p. 103913. DOI: `10.1063/1.3587173`.

[113] S. Zhang and Z. Li. “Roles of Nonequilibrium Conduction Electrons on the Magnetization Dynamics of Ferromagnets”. In: *Physical Review Letters* 93.12 (Sept. 2004), p. 127204. DOI: `10.1103/physrevlett.93.127204`.

[114] J. C. Slonczewski. “Currents and torques in metallic magnetic multilayers”. In: *Journal of Magnetism and Magnetic Materials* 247.3 (June 2002), pp. 324–338. DOI: `10.1016/s0304-8853(02)00291-3`.

[115] M. Buettiker, H. Thomas, and A. Prêtre. “Current partition in multiprobe conductors in the presence of slowly oscillating external potentials”. In: *Zeitschrift fuer Physik B Condensed Matter* 94.1-2 (Mar. 1994), pp. 133–137. DOI: `10.1007/bf01307664`.

[116] Pavlo Omelchenko, Erol Girt, and Bret Heinrich. “Test of spin pumping into proximity-polarized Pt by in-phase and out-of-phase pumping in Py/Pt/Py”. In: *Physical Review B* 100.14 (Oct. 2019), p. 144418. DOI: `10.1103/physrevb.100.144418`.

[117] M. Sturma et al. “Simultaneous resolution of the micromagnetic and spin transport equations applied to current-induced domain wall dynamics”. In: *Physical Review B* 94.10 (Sept. 2016), p. 104405. DOI: `10.1103/physrevb.94.104405`.

[118] Serban Lepadatu. “Boris computational spintronics—High performance multi-mesh magnetic and spin transport modeling software”. In: *Journal of Applied Physics* 128.24 (Dec. 2020), p. 243902. DOI: `10.1063/5.0024382`.

[119] Saburo Takahashi. “Physical Principles of Spin Pumping”. In: *Handbook of Spintronics*. Dordrecht: Springer Netherlands, 2016, pp. 1445–1480. DOI: 10.1007/978-94-007-6892-5_51.

[120] A. Sommerfeld. “Zur Elektronentheorie der Metalle auf Grund der Fermischen Statistik”. In: *Zeitschrift für Physik* 47.1-2 (Jan. 1928), pp. 1–32. DOI: 10.1007/bf01391052.

[121] Youcef Saad and Martin H. Schultz. “GMRES: A Generalized Minimal Residual Algorithm for Solving Nonsymmetric Linear Systems”. In: *SIAM Journal on Scientific and Statistical Computing* 7.3 (July 1986), pp. 856–869. DOI: 10.1137/0907058.

[122] J. W. Ruge and K. Stüben. “4. Algebraic Multigrid”. In: *Multigrid Methods*. Society for Industrial and Applied Mathematics, Jan. 1987, pp. 73–130. DOI: 10.1137/1.9781611971057.ch4.

[123] Jocelyne Erhel, Kevin Burrage, and Bert Pohl. “Restarted GMRES preconditioned by deflation”. In: *Journal of Computational and Applied Mathematics* 69.2 (May 1996), pp. 303–318. DOI: 10.1016/0377-0427(95)00047-x.

[124] Satish Balay et al. *PETSc/TAO Users Manual*. Tech. rep. ANL-21/39 - Revision 3.19. Argonne National Laboratory, 2023. DOI: 10.2172/1968587.

[125] Issai Schur. “Neue Begründung der Theorie der Gruppencharaktere”. In: *Sitzungsberichte der Königlich Preussischen Akademie der Wissenschaften*. Vol. 1. 1905. Berlin: Verlag der Königlichen Akademie der Wissenschaften, 1905, pp. 406–432.

[126] Richard Phillips Feynman, Robert B. Leighton, and Matthew Sands. *The Feynman Lectures on Physics. New Millenium Edition*. New Millenium Edition. 3 vols. Basic Books, Jan. 4, 2011. ISBN: 9780465024148.

[127] D. Polder. “On the theory of ferromagnetic resonance”. In: *Physica* 15.1-2 (Apr. 1949), pp. 253–255. DOI: 10.1016/0031-8914(49)90051-8.

[128] E. C. Stoner and E. P. Wohlfarth. “A mechanism of magnetic hysteresis in heterogeneous alloys”. In: *Philosophical Transactions of the Royal Society of London. Series A, Mathematical and Physical Sciences* 240.826 (May 1948), pp. 599–642. DOI: 10.1098/rsta.1948.0007.

[129] Charles Kittel. “On the Theory of Ferromagnetic Resonance Absorption”. In: *Physical Review* 73.2 (Jan. 1948), pp. 155–161. DOI: 10.1103/physrev.73.155.

[130] Herbert Goldstein, Charles P. Poole, and John L. Safko. *Classical Mechanics (3rd Edition)*. Addison Wesley, 2002, p. 680. ISBN: 9780201657029.

[131] J. A. Osborn. “Demagnetizing Factors of the General Ellipsoid”. In: *Physical Review* 67.11–12 (June 1945), pp. 351–357. ISSN: 0031-899X. DOI: 10.1103/physrev.67.351.

[132] G. V. Skrotskii and Yu. I. Alimov. “Ferromagnetic Resonance in a circularly polarized Electromagnetic Field of arbitrary Amplitude”. In: *Zhur. Eksptl’. i Teoret. Fiz.* 35.6 (1959), pp. 1481–1484. URL: https://www.osti.gov/biblio/4258191.

[133] G. V. Skrotskii and Yu. I. Alimov. “Effect of Specimen Shape on Ferromagnetic Resonance in a strong Radio-Frequency Field”. In: *Zhur. Eksptl’. i Teoret. Fiz.* 36.4 (1959), pp. 1267–1271. URL: https://www.osti.gov/biblio/4245031.

[134] R. W. Damon and J. R. Eshbach. “Magnetostatic modes of a ferromagnet slab”. In: *Journal of Physics and Chemistry of Solids* 19.3-4 (May 1961), pp. 308–320. DOI: 10.1016/0022-3697(61)90041-5.

[135] L. R. Walker. “Resonant Modes of Ferromagnetic Spheroids”. In: *Journal of Applied Physics* 29.3 (Mar. 1958), pp. 318–323. DOI: 10.1063/1.1723117.

[136] J. R. Eshbach and R. W. Damon. “Surface Magnetostatic Modes and Surface Spin Waves”. In: *Physical Review* 118.5 (June 1960), pp. 1208–1210. DOI: 10.1103/physrev.118.1208.

[137] Massimiliano d’Aquino et al. “A novel formulation for the numerical computation of magnetization modes in complex micromagnetic systems”. In: *Journal of Computational Physics* 228.17 (Sept. 2009), pp. 6130–6149. DOI: 10.1016/j.jcp.2009.05.026.

[138] Florian Bruckner et al. “Large scale finite-element simulation of micromagnetic thermal noise”. In: *Journal of Magnetism and Magnetic Materials* 475 (Apr. 2019), pp. 408–414. DOI: 10.1016/j.jmmm.2018.11.106.

[139] C. Lanczos. “An iteration method for the solution of the eigenvalue problem of linear differential and integral operators”. In: *Journal of Research of the National Bureau of Standards* 45.4 (Oct. 1950), p. 255. DOI: 10.6028/jres.045.026.

[140] J. J. Sakurai and Jim J. Napolitano. *Modern Quantum Mechanics*. Pearson, 2011, p. 520. ISBN: 9781292024103.

[141] L. Brillouin. “Les électrons libres dans les métaux et le role des réflexions de Bragg”. In: *Journal de Physique et le Radium* 1.11 (1930), pp. 377–400. DOI: 10.1051/jphysrad:01930001011037700.

[142] N. N. Bogoljubov. “On a new method in the theory of superconductivity”. In: *Il Nuovo Cimento* 7.6 (Mar. 1958), pp. 794–805. DOI: 10.1007/bf02745585.

[143] Paul Adrien Maurice Dirac. “The physical interpretation of the quantum dynamics”. In: *Proceedings of the Royal Society of London. Series A, Containing Papers of a Mathematical and Physical Character* 113.765 (Jan. 1927), pp. 621–641. ISSN: 2053-9150. DOI: 10.1098/rspa.1927.0012.

[144] Satyendranath Bose. “Plancks Gesetz und Lichtquantenhypothese”. In: *Zeitschrift für Physik* 26.1 (Dec. 1924), pp. 178–181. ISSN: 1434-601X. DOI: 10.1007/bf01327326.

[145] A. Einstein. *Quantentheorie des einatomigen idealen Gases*. 1924. DOI: 10.1002/3527608958.ch27.

[146] A. Einstein. *Quantentheorie des einatomigen idealen Gases. Zweite Abhandlung*. 1925. DOI: 10.1002/3527608958.ch28.

[147] S. O. Demokritov et al. “Bose–Einstein condensation of quasi-equilibrium magnons at room temperature under pumping”. In: *Nature* 443.7110 (Sept. 2006), pp. 430–433. ISSN: 1476-4687. DOI: 10.1038/nature05117.

[148] H. Suhl. “The theory of ferromagnetic resonance at high signal powers”. In: *Journal of Physics and Chemistry of Solids* 1.4 (Jan. 1957), pp. 209–227. DOI: 10.1016/0022-3697(57)90010-0.

[149] B. A. Kalinikos and A. N. Slavin. “Theory of dipole-exchange spin wave spectrum for ferromagnetic films with mixed exchange boundary conditions”. In: *Journal of Physics C: Solid State Physics* 19.35 (Dec. 1986), pp. 7013–7033. ISSN: 0022-3719. DOI: 10.1088/0022-3719/19/35/014.

[150] E. V. Skorohodov et al. “Ferromagnetic resonance in submicron permalloy stripes”. In: *Journal of Magnetism and Magnetic Materials* 424 (Feb. 2017), pp. 118–121. DOI: 10.1016/j.jmmm.2016.10.024.

[151] A. G. Gurevich and G. A. Melkov. *Magnetization Oscillations and Waves*. Boca Raton, Florida: CRC Press, 1996. ISBN: 0849394600.

[152] Enrico Fermi. *Nuclear physics*. Rev. ed., reprint. Chicago [u.a.]: Univ. of Chicago Press, 1974. 248 pp. ISBN: 0226243656.

[153] Markus Gattringer et al. “Offset-Free Magnetic Field Sensor Based on a Standing Spin Wave”. In: *Physical Review Applied* 20.4 (Oct. 2023), p. 044083. DOI: 10.1103/physrevapplied.20.044083.

[154] Yiyan Sun et al. “Damping in Yttrium Iron Garnet Nanoscale Films Capped by Platinum”. In: *Physical Review Letters* 111.10 (Sept. 2013), p. 106601. DOI: 10.1103/physrevlett.111.106601.

[155] Oscar Alejos et al. “Efficient and controlled domain wall nucleation for magnetic shift registers”. In: *Scientific Reports* 7.1 (Sept. 2017). DOI: 10.1038/s41598-017-12230-9.

[156] Zhiwei Ren et al. “Reconfigurable nanoscale spin-wave directional coupler using spin-orbit torque”. In: *Scientific Reports* 9.1 (May 2019). DOI: 10.1038/s41598-019-43597-6.

[157] Xiaolong Fan et al. “Electrical detection of microwave assisted magnetization switching in a Permalloy microstrip”. In: *Applied Physics Letters* 95.6 (Aug. 2009). DOI: 10.1063/1.3200239.

[158] Dominika Kuźma et al. “Effects of shape on magnetization switching in systems of magnetic elongated nanoparticles”. In: *Journal of Magnetism and Magnetic Materials* 545 (Mar. 2022), p. 168685. DOI: 10.1016/j.jmmm.2021.168685.

[159] P. Ripka et al. “AC-driven AMR and GMR magnetoresistors”. In: *Sensors and Actuators A: Physical* 76.1-3 (Aug. 1999), pp. 225–230. DOI: 10.1016/s0924-4247(99)00034-5.

[160] M. Pardavi-Horvath et al. “Angular dependence of ferromagnetic resonance and magnetization configuration of thin film Permalloy nanoellipse arrays”. In: *Journal of Applied Physics* 110.5 (Sept. 2011), p. 053921. DOI: 10.1063/1.3633214.

[161] Y. Li et al. “Nutation Spectroscopy of a Nanomagnet Driven into Deeply Nonlinear Ferromagnetic Resonance”. In: *Physical Review X* 9.4 (Nov. 2019), p. 041036. ISSN: 2160-3308. DOI: 10.1103/physrevx.9.041036.